Saroj Kumar Jha

Ph.D Thesis

Ph.D Thesis

PHD

Jawaharlal Nehru University

Document Details

Submission ID

trn:oid:::1:3438961235

Submission Date

Dec 9, 2025, 9:43 AM GMT+5:30

Download Date

Dec 9, 2025, 9:59 AM GMT+5:30

File Name

Thesis__09122025__without_Ref.pdf

File Size

5.9 MB

172 Pages

46,941 Words

248,740 Characters

5% Overall Similarity

The combined total of all matches, including overlapping sources, for each database.

Filtered from the Report

- Bibliography
- Quoted Text
- Small Matches (less than 14 words)

Exclusions

- 3 Excluded Sources
- 63 Excluded Matches

Match Groups

85 Not Cited or Quoted 5%
Matches with neither in-text citation nor quotation marks

1 Missing Quotations 0%
Matches that are still very similar to source material

0 Missing Citation 0%
Matches that have quotation marks, but no in-text citation

0 Cited and Quoted 0%
Matches with in-text citation present, but no quotation marks

Top Sources

2% Internet sources
3% Publications
1% Submitted works (Student Papers)

Integrity Flags

1 Integrity Flag for Review

Replaced Characters
64 suspect characters on 34 pages
Letters are swapped with similar characters from another alphabet.

Our system's algorithms look deeply at a document for any inconsistencies that would set it apart from a normal submission. If we notice something strange, we flag it for you to review.

A Flag is not necessarily an indicator of a problem. However, we'd recommend you focus your attention there for further review.

Match Groups

- **85** Not Cited or Quoted 5%
  Matches with neither in-text citation nor quotation marks
- **1** Missing Quotations 0%
  Matches that are still very similar to source material
- **0** Missing Citation 0%
  Matches that have quotation marks, but no in-text citation
- **0** Cited and Quoted 0%
  Matches with in-text citation present, but no quotation marks

Top Sources

2% Internet sources
3% Publications
1% Submitted works (Student Papers)

Top Sources

The sources with the highest number of matches within the submission. Overlapping sources will not be displayed.

1	Internet	
discovery.researcher.life		<1%
2	Student papers	
University of Sheffield		<1%
3	Publication	
Jyoti Saini, Monika Sharma, Sheetal Yadav, Bijoy Kumar Kuanr. "Effect of Bi and C...		<1%
4	Internet	
hdl.handle.net		<1%
5	Internet	
confcats-siteplex.s3.us-east-1.amazonaws.com		<1%
6	Publication	
Chunhui Du, Hailong Wang, Fengyuan Yang, P. Chris Hammel. " Enhancement of ...		<1%
7	Publication	
Shilpa Samdani, Yaqi Rong, Birte Coester, Amit Kumar Shukla, Wen Siang Lew, Yu...		<1%
8	Internet	
etheses.whiterose.ac.uk		<1%
9	Publication	
Ganesh Gurjar, Vinay Sharma, Avirup De, Sunil Nair, S Patnaik, Bijoy K Kuanr. " Cr...		<1%
10	Publication	
Zhiyong Qiu, Dazhi Hou, Joseph Barker, Kei Yamamoto, Olena Gomonay, Eiji Saito...		<1%

11	Publication	Zbigniew Celinski, I.R. Harward, N.R. Anderson, Robert E. Camley. "Planar Magnet... <1%
12	Publication	H. L. Wang, C. H. Du, Y. Pu, R. Adur, P. C. Hammel, F. Y. Yang. " Scaling of Spin Hall ... <1%
13	Publication	Prashant Kumar, Ravi Kumar, Vipul Sharma, Manoj Kumar Khanna, Bijoy Kumar K... <1%
14	Publication	P. Merodio, A. Ghosh, C. Lemonias, E. Gautier, U. Ebels, M. Chshiev, H. Béa, V. Balt... <1%
15	Publication	Ganesh Gurjar, Vinay Sharma, S Patnaik, Bijoy K Kuanr. "Control of magnetization... <1%
16	Publication	Pawel Gruszecki, Chandrima Banerjee, Michal Mruczkiewicz, Olav Hellwig, Anjan ... <1%
17	Internet	worldwidescience.org <1%
18	Publication	Acuna Gonzalez, Wilder. "Development of ErAs-Embedded III-V Semiconductor Str... <1%
19	Student papers	Cranfield University <1%
20	Internet	www.politesi.polimi.it <1%
21	Publication	Nepal, Rajeev. "Heterostructures of Van Der Waal Semimetals and Soft Ferromag... <1%
22	Publication	Franson, Andrew J.. "Patterning and Characterization of Ferrimagnets for Cohere... <1%
23	Publication	Zeinab Harajli, Samih Isber, Mohammad Haidar. "Optimizing spin pumping in Yttr... <1%
24	Internet	dspace.uohyd.ac.in <1%

25	Publication	Hailong Wang, Chunhui Du, P. Chris Hammel, Fengyuan Yang. " Antiferromagnon... <1%
26	Publication	Prashant Kumar, Ravi Kumar, Vipul Sharma, Manoj Kumar Khanna, Bijoy Kumar K... <1%
27	Internet	tel.archives-ouvertes.fr <1%
28	Publication	B. Bayard, B. Sauviac, D. Vincent. "Ferrite Isolators", Wiley, 2005 <1%
29	Publication	Harder, Michael, Yongsheng Gui, and Can-Ming Hu. "Electrical detection of magn... <1%
30	Publication	Sergio M. Rezende. "Fundamentals of Magnonics", Springer Science and Business ... <1%
31	Internet	academic-accelerator.com <1%
32	Internet	pure.rug.nl <1%
33	Internet	www.science.gov <1%
34	Publication	Bromley, Daniel. "Spin Transport in Superconducting and Ferromagnetic Heteros... <1%
35	Publication	Wang, Hailong. "Understanding of pure spin transport in a broad range of y</sub... <1%
36	Publication	Bijoy K. Kuanr, V. Veerakumar, Ryan Marson, Sanjay R. Mishra, R. E. Camley, Z. Cel... <1%
37	Publication	Gaur, Samanvaya Singh. "Ferromagnetic Cobalt-Iron Thin Films for Light Induced ... <1%
38	Publication	Handbook of Spintronics, 2016. <1%

39 Student papers

Jawaharlal Nehru University (JNU) <1%

40 Publication

Sunayana Bhardwaj, Prashant Kumar, Ram Krishna Ghosh, Bijoy K. Kuanr. "Role o... <1%

41 Publication

Yongjian Zhou, Tingwen Guo, Leilei Qiao, Qian Wang et al. "Piezoelectric Strain-C... <1%

42 Internet

digitalcommons.wayne.edu <1%

43 Publication

Holmes, Alexander M.. "Nonreciprocal Surface Waves on Gyrotropic Interfaces", T... <1%

44 Publication

Sarah Heidtfeld, Roman Adam, Takahide Kubota, Koki Takanashi et al. " Generati... <1%

45 Internet

physlab.org <1%

Chapter 1

Introduction and Scientific Motivation

This chapter primarily focuses on introduction of the research challenge and motivation for the current investigation. It begins with a brief background and overview of the study, followed by a summary of the key motivation behind this dissertation work. The magnetic systems studied in this thesis are then described along with the fundamental theoretical concepts of Ferromagnetic Resonance (FMR), a widely used technique for demonstrating device testing, and magnetization dynamics investigations. The chapter also discusses essential topics such as spin wave and magnons, energy redistribution within magnetic systems and energy transfer from the magnetic to nonmagnetic interfaces. Furthermore, spin hall and inverse spin hall effect are discussed due to their significance for spin pumping and spin transport phenomena. The chapter concludes with an outline of the broad thesis structure.

1.1 Background and overview

A number of significant and profound changes in the fields of technology and communication were sparked by the invention of transistor [1] in 1947. The rapid expansion and advancement of integrated circuits and high-performance electronic devices have changed the basis of the global economy and is having an increasing influence on every aspect of existence, from daily life to the most cutting-edge science, technology, and business. The development of semiconductor-based technology has always been aided by the incredibly high integration density, faster speed, and ever-increasing data processing capacity. These benefits, when coupled with developments in optical communication, have made it simple and inexpensive to store, process, and send vast amounts of data. However, the International Technology Roadmap for

Semiconductors said in 2011, that since single-element size and operational speed will both reach their ultimate limits in the coming years, semiconductor-based technology will face significant challenges impeding downscaling and power reduction in the near future. Generation of waste heat during switching is also a fundamental drawback in electronics. In the meantime, research in the field of nano magnetism and magnetization dynamics, a well-liked subfield of spintronics [2], owing to its potential uses in nanoscale signal processing and information transfer devices [3-5]. By innovation and advancements in radiofrequency (RF) and microwave communication technologies, circuits have grown increasingly complex and compact, utilizing a variety of materials, including magnetic ones. The manipulation and control of electrons spin degree of freedom is the source of the promise of spintronics, a relatively new field of nanoelectronics study. As the ultimate quantum mechanical limit of Moore's law approaches [6,7], this new technology is being investigated. The concept of spin is often combined with the charge of an electron in these electrical devices [2, 8]. Electric signal transmission through magnetic insulator [9] and spin Seeback effect in magnetic insulator [10,11] are the two main areas of current spintronics research. Around fifty years ago, both of these research topics are experimentally evaluated through magnetic material, Charles Kittel referred to it as the "fruit fly of magnetism [12]. Yttrium iron garnet ($Y_3Fe_5O_{12}$, YIG) [13], most suitable and well-known ferromagnetic insulator, which has received notable attention in recent periods for the spintronics applications. The development of effective converters that can convert pure spin currents into charge currents and vice versa is essential for the implementation of insulator-based devices. The exchange interaction between insulator electrons and conduction electron spins at the interface allows for the realization of spin current transfer in ferromagnetic insulator/metal bilayers. The generation and transfer of spin-polarized current from the ferromagnetic layer to the adjoining normal metal layer is referred to as the spin pumping effect [14,15]. The full cycle of conversion, or going from a charge current in the normal metal to a pure spin current and back to a charge current, was first shown by Kajiwara et al. in 2010 in the magnetic insulator/normal metal (YIG/Pt)

bilayer structure. In 2010, Slonczewski, proposed the concept of using thermal transport of magnons to produce spin transfer torque [16]. Since then, there has been a sharp rise in interest in using spin pumping and spin transfer torque to investigate different aspects of magnetization dynamics in magnetic/metal bilayer systems. YIG is one of the most researched magnetic materials. YIG is one of the most researched magnetic materials, Because of its numerous uses in magneto-optical devices including optical insulators, screens, and deflectors as well as microwave devices like microwave filters, delay lines etc. There is a need for nanometer-thick YIG films with excellent crystalline quality that maintain exceptionally low Gilbert damping due to the recent advancements in magnonics and oxide spintronics. In the first instance, the spin Hall effect causes an electrical signal to stimulate a spin wave in a YIG film strip [17]. The inverse spin Hall effect [18] transforms the spin wave into an electrical signal as it moves to the opposite end of the YIG strip. Because spin-up and spin-down electrons have different chemical potentials, a temperature gradient across a YIG film strip causes a voltage to be produced in the spin Seebeck scenario. The typical metal layer on a film strip may experience spin currents as a result of these variations in potential, also known as spin voltage. The variety of chemical and physical methods can be used to create high-quality YIG thin films [19-21]. Lichuan et al. investigated the effect of annealing temperature on material composition and magnetic characteristics and reported Gilbert damping constant of 5.74×10^{-4} for YIG thin films annealed at 800 °C [22]. Bhoi et al. noticed that saturation magnetization increases and the FMR linewidth decreases with the increase of film thickness [23]. Additionally, Bhoi et al. documented how oxygen pressure affected the FMR linewidth and saturation magnetization of YIG films produced on quartz substrates. [24]. Ferromagnetic Resonance (FMR) spectroscopy is a comprehensive method for identifying and evaluating the range of magnetic parameters [25-29]. Another crucial characteristic that results from the spin-orbital interaction that is vital in a crystalline material system is the magneto crystalline anisotropy (MCA) [30-32]. Additionally, the FMR tool can easily examine spin-controlled devices at microwave and terahertz frequencies [33,34]. In today's time

ferromagnetic has a broad range of device applications starting from the most popular radar and communication devices like filters, phase shifters, and isolators to the most advanced next generation Spin Transfer Torque (STT) Magnetic Random Access Memory (MRAM) and Magnetic Tunnel Junction (MTJ) based devices [35-37]. The thin film is crucial for creating a device structure among the several ferromagnetic nanostructure types, including nanoparticles, thin films, and nanotubes. Because of the strain and roughness of the interface, the material characteristics drastically shift from a bulk material form to a material film of a nanometers in thickness. One key distinction between bulk and thin-film materials is that surface or interface effects are often control the characteristics of thin films [38,39]. To obtain the desired device feature, it is simple to adjust and control the magnetic characteristics in thin-film. Several obstacles must be overcome in the field of spintronics before industrial-level product releases may occur. Spin injection, spin transport, and spin detection are the three main functions of a spintronics device, and they are related to these difficulties According to the current research and understanding magnetic garnets are most suitable candidate for the creation and transfer of spin currents [40,41]. In this research work, we have discussed the synthesis and characterization of heterostructures based on pure yttrium iron garnet (YIG) thin film for spintronics device applications. For this thesis work, yttrium iron garnet (YIG) is selected as a ferrimagnetic insulator because of its lowest known spin dissipation value, exceptionally low Gilbert damping constant, and high uniaxial and cubic anisotropy. All these are the prerequisites and recommendation for the transfer of spin waves over a longer range.

1.2 Motivation

This thesis describes the development of high-quality crystalline ferromagnetic nanometer (nm) thick films, and heterostructures of ferromagnetic/normal metal multilayer. Pulsed laser deposition and DC/RF sputtering technique utilized to create different kinds of nanostructures. The produced thin-film structures were examined for microwave devices

and spintronics applications throughout a wide frequency range, and comprehensive structural and magnetic experiments were carried out. The research for this thesis was primarily motivated by three main concerns. First, it has to do with the exponential growth of electron-based electronics' speed and storage capacity as well as their enormous increase in power consumption [42-45].

Furthermore, the decreasing size of devices restricts their use in new cutting-edge technologies and communication. Therefore, tunable miniature devices that can function across a broad frequency range without altering their construction are desperately needed. Magnetic thin films and their heterostructures represent one of the most actively studied classes of materials in spintronics. Thin films, as compared to bulk materials, have lower dimensionality, changed magnetic anisotropy, and an increased role of surface or interfacial contributions, all of which significantly affect their spin and charge transport properties [46].

Control of nanoscale magnetization dynamics is of utmost significance, both to improve fundamental knowledge and to facilitate the development of energy-saving devices that utilize spin currents instead of charge currents. Within thin films, this damping mechanism dictates how well spin angular momentum can be preserved during precession. Small damping values are critical to the observation of long-distance magnon transport, high-frequency spin oscillators, and spin-wave logic devices [47]. Damping is, however, not a material constant; it is highly sensitive to defects, surface roughness, but most particularly to the interface quality with neighboring layers. Therefore, research into the damping mechanisms in thin films gives invaluable information both on fundamental physics and material optimization. In contemporary spintronic structures, ferromagnets are usually paired with normal metals (e.g., Pt, W, Cu) or other functional layers to create heterostructures. Magnetization dynamics at these interfaces can initiate spin currents through the phenomenon of spin pumping [15]. The effectiveness of such interfacial transfer is measured by the spin mixing conductance ($g\uparrow\downarrow$), which describes how well the

angular momentum can be transferred through the interface [48]. Large values of spin mixing conductance are preferred since they indicate the strong interfacial coupling and efficient spin transfer. In contrast, badly designed interfaces can introduce extra scattering channels that increase two-magnon scattering and thus broaden linewidths in ferromagnetic resonance (FMR) measurements [49].

It is this that emphasizes the importance of the accurate control and characterization of interfaces in thin films to the advances in spintronic technologies. A further compelling motivation comes from the role of interfacial spin–orbit coupling in controlling spin–charge conversion phenomena. In spin-injected heavy metals like Pt and W, spin currents are transformed into measurable charge currents using the inverse spin Hall effect [19,50]. Not only is this transformation a probe of the spin dynamics that underlies it, but it is also the operating principle of most spintronic devices, such as spin Hall magnetoresistance sensors and spin–orbit torque memories [51].

An understanding of the mechanisms by which spin currents travel through intermediate spacers (e.g., Cu) and by which interface quality influences ISHE voltages is thus an urgent research requirement. Magnetic thin films like epitaxial yttrium iron garnet (YIG) on GGG substrates provide model systems with ultra-low damping [8,52] and thus are excellent platforms to explore these spin–orbit mediated interfacial effects. The incentive for this technology is also very application-focused. Spintronics and magnonics are designed to minimize power consumption by the removal of Joule heating, which is inherent in charge-based electronics [10]. Engineered interfacial dynamics in magnetic thin films are set to facilitate a broad array of next-generation technologies having so many applications few of them is mentioned below,

Magnonics: Low-damping thin films enable the propagation of spin waves over long distances, providing the foundation for wave-based computing in magnonic circuits [47].

Memory and Logic Devices: Spin pumping and ISHE offer a method of ultrafast, low-power information transfer in magnetic random-access memory (MRAM) and logic devices [53]

Insulator-Based Spintronics: Magnetic insulators such as YIG are capable of producing pure spin currents without electron transport, greatly reducing dissipation and allowing hybrid device architectures [8].

Aside from applications, there is also a compelling fundamental motivation. Thin film magnetism is a rich arena for the exploration of many-body interactions, magnon–phonon coupling, interfacial exchange, and spin–orbit physics. Strain sensitivity, stoichiometry sensitivity, and dimensional confinement in sensitivity of magnetic properties provide the opportunity to discover new quantum phenomena. In addition, by controlling deposition parameters, layer thicknesses, and interface structures with deliberate systematic variation, scientists can chart the interplay between material growth conditions, structural quality, and dynamical spin properties [54]. These insights are crucial to closing the gap between prediction and realistic device performance.

In summary, the research on magnetic properties and interfacial spin dynamics in magnetic thin films is driven by a twofold motivation, the quest for basic understanding of spin interaction in low dimensions and the pressing technological imperative for low-power, scalable substitutes to charge-based electronics. By probing the way interfaces change damping, spin pumping, and spin–charge conversion, can reveal the rules of spin transport at the nanoscale. Such understanding will speed up the invention of next-generation magnonic and spintronic devices, leading to high-speed, energy-savings, and multifunctional information technologies. We have carried out a thorough investigation into the development of magnetic thin film nanostructures and how they might be used in high-frequency spintronic devices.

In order to investigate the current technological obstacles, we have chosen yttrium iron garnet (YIG) for ferrimagnetic nanostructures thin film. YIG was selected because it is a soft magnetic material with very low coercivity and magnetization. Additionally, it has the lowest FMR line width and Gilbert damping [33,54–56], which aided in the design of effective high frequency filters and isolators across a wide frequency range. The impact of changes in oxygen gas growth pressure during film growth, as well as the angle dependent FMR measurements of epitaxial YIG thin films deposition on GGG (111) substrates is novel research which is first examined and reported by us.

Second motivation, due to significant effect of the magnetic medium on the radiated power of the microstrip and the current distribution, magnetostatic modes can be induced in YIG thin films utilizing microstrip lines [57-59]. This can result in devices like spin-wave filters and isolators, which have a lot of potential for use in new, small, inexpensive reconfigurable microwave devices. The impact of varying oxygen gas pressure during the thin film formation has been studied on the wave propagation. Designing both reciprocal and non-reciprocal devices requires a strong theoretical foundation that closely aligns with experimental efforts. We have used Ansys HFSS (High Frequency Simulation Software) packages to numerically simulate the isolator structures utilizing full-wave simulations. The capacity to model entire waves serves as a crucial link between theoretical research and experimental findings.

Investigating a material that can be utilized in spintronics and flexible electronics devices is the third motivation for this study. Researchers are currently very interested in spin transport and magneto-dynamics in antiferromagnetic (AF) insulators [60–62]. The efficacy of spin pumping is predicted by both experimental and theoretical research to be dependent on a number of factors, including interface quality, the presence of magnetic anisotropy in the FM Layer, and spin orbit coupling in the NM Layer. For instance, the proximity-induced ferromagnetism in YIG/Pt systems has recently been suppressed by Cu interlayers [63–66]. In order to investigate spin pumping for spintronics device

applications, we have deposited the heterostructure of multilayer using FM, AFM and normal metal. The next section includes a quick overview of the compound/metal used in this research work.

1.2.1 YIG

YIG holds a unique position among high frequency and spintronic materials and is a significant soft magnetic material. YIG's two key characteristics are low magnetization damping and small value of line width [67,68]. Experiments may be conducted at room temperature due to the high Curie temperature of 560 K. These factors have made YIG an essential component for microwaves and magnonics. YIG is ferrimagnetic insulator with a garnet crystal structure. The structure of the YIG crystal is made up of metal and oxygen polyhedrons. The space group of YIG is Ia3 d, and the body-centered cubic (BCC) unit cells contain the Fe atoms.

The anti-parallel alignment of the magnetic moments created by Fe^{+3} ions at the "16a (Octahedral) site and 24d (tetrahedral) site [69,70]. Additionally, the moments of the Y^{+3} ions at the "24c (dodecahedral)" sites are anti-parallel to the vector sum of the moments at the 16a and 24d sites. In contrast to metal ferromagnets, YIG's ultralow Gilbert damping ($\alpha \sim 10^{-5}$) allows spin waves (magnons) to propagate on millimeter-length scales, making it a perfect model system for research on spin dynamics and magnon transport [52].

1.2.2 Ni

One of the most studied ferromagnets in magnetism and spintronics is nickel (Ni), a 3D ferromagnetic transition metal with strong electrical conductivity and a Curie temperature of about 627 K [71]. Ni's metallic ferromagnetism has led to its frequent use in fundamental studies of spin-polarized transport, giant magnetoresistance (GMR), and magnetization dynamics [72]. However, Ni can readily create Nickel Oxide (NiO), an antiferromagnetic insulator with a Néel temperature of about 523 K, when exposed to

oxidation. Ni is often converted to NiO by controlled reactive sputtering or heating in air. NiO is a wide-bandgap (~4 eV) insulating antiferromagnet, unlike metallic Ni, and can achieve a unique interfacial spin-exchange coupling with ferromagnets thanks to its compensating spin structure [73,74]. In spintronics, NiO is a key component that mediates interfacial spin dynamics. NiO efficiently mediates the transmission of spin current by antiferromagnetic magnons between YIG and a heavy metal such as Pt, which usually improves spin pumping and the inverse spin Hall effect [75,76].

1.2.3 Normal metal (Pt, W, Cu)

Normal metal like platinum (Pt), tungsten (W) and copper (Cu) play an important role in spintronics due to their special characteristics and interaction with magnetic materials [18,77]. Pt and W are heavy metals with robust spin orbit coupling that can efficiently convert charge current in to the spin current through the spin Hall effect. Due to their strong spin orbit coupling, these metals have a large spin hall effect, which makes it easier to detect and produce spin currents [51,65,78]. Pt and W are frequently used in spin Hall effect-based devices for spintronics applications, such as charge current -to- spin current conversion, spin logic operation and spin orbit torque switching [18,79]. While copper (Cu), a light metal with a weak intrinsic spin orbit coupling, is useful due to its large spin diffusion length and recent development with orbital torques. It is a typical metal with a very long spin diffusion length, making it appropriate for spin transport in multilayer geometries and lateral spin valves [48,80,81]. This makes it both cost-effective and environmentally friendly for use in future spintronic devices. Cu is a key component of magnetic heterostructures and lateral spin valves, serving as a platform to investigate orbital torque generation and the orbital Hall effect as well as a spacer for the conveyance of pure spin current [82].

1.3 Magnetic properties and crystal structure of YIG

Bertaut and Forrat discovered yttrium iron garnet YIG ($Y3Fe5O12$) in 1956 [14, 83]. Kittel called it the fruit fly of magnetism around half a century ago [13]. This material receives a lot of interest due to its superior dynamical properties [84]. Yttrium iron garnet has a distinct composition and a complicated crystal structure with almost cubic symmetry. YIG has a density of 5.17 g/cm^3 [85]. Its magnetization damping is a minuscule 3×10^{-5} [84]. It has a high Curie temperature of roughly 560 K and a wide band gap of 2.85 eV [85].

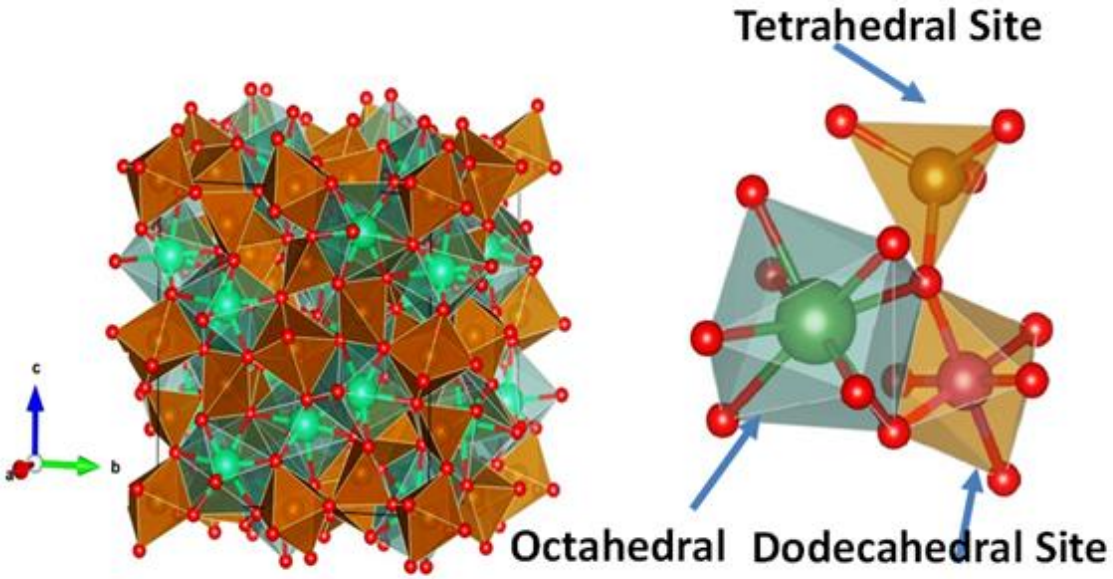

Fig:1.1 Yttrium iron garnet ($Y_3Fe_5O_{12}$) Crystal Structure

According to reports, the YIG unit cell's lattice constant is 12.376 ± 0.004 Å [13]. Space group is $Ia\bar{3}d$ used for YIG crystallization [12]. The cubic structure of the YIG unit cell is composed of eight units of the chemical formula $Y_3Fe_5O_{12}$. The unit cell contains 160 ions in total shown in fig. 1.1. Three c sites (dodecahedral), two *a* sites (octahedral), and three d sites (tetrahedral) make up each YIG formula unit. There are 96 oxygen ions, 40 iron

ions, and 24 yttrium ions in each of the eight YIG formula units. Eight oxygen ions encircle the Y^{3+} ions found in the dodecahedral c sites, creating an eight-cornered, twelve-sided polyhedron. Four O^{2-}ions surround each of the 24 Fe^{3+} ions that occupy the d sites, resulting in tetrahedral symmetry. The six O^{2-}ions encircling the sixteen Fe^{3+} ions provide octahedral symmetry. The O^{2-} ions occupy h sites, which are created when two polyhedra, an octahedron, and a tetrahedron interact. Each O^{2-}ion is thus surrounded by two c site Y^{3+} ions, one *a* site Fe^{3+}, and one d site Fe^{3+}. Y^{3+} ions have no magnetic moment. Super-exchange interactions between non-equivalent Fe^{3+} ions at the d and *a* sites are what cause the ferrimagnetism of YIG. Three types of super-exchange interaction: Fe^{3+} ions at the d-site with nearest d-site neighbor, Fe^{3+} ions at the *a* -site with nearest a-site neighbor, and Fe^{3+} ions at the d-site with nearest a-site neighbors define the total magnetic moment in YIG. Theoretically, the angle and distance of the Fe-O-Fe bonds determine how strong the super-exchange interactions are [26]. At bond angles of 180^0 and 90^0, respectively, the strongest and weakest interactions take place. Maximum bond angle in YIG is 126.6^0 between "a site Fe^{3+}"-"O^{2-}"-"d site Fe^{3+}" [13,86]. Consequently, Fe^{3+} ions exhibit the strongest super-exchange interactions at the d and *a* sites. The magnetic moments of three Fe^{3+} in d sites and two Fe^{3+} in *a* sites are arranged antiparallel as a result of this interaction. With magnetization parallel to the magnetic moments in the direction of the d site, this results in a net magnetic moment of $5\mu_B$ per formula unit. The experimentally determined magnetic moments in earlier reports ranged from $4.72\mu_B$ to $5.01\mu_B$ [87]. The average recorded room-temperature saturation magnetization ($4\pi M_s$) value is 1750 G [13], with reported values ranging from 1730 G to 1780 G.

The ferric ions, which have a spherical charge distribution and are in a L = 0 state, are the only magnetic ions in YIG. Thus, they have little interaction with phonons and lattice deformation. In ferromagnetic resonance (FMR) investigations, YIG is characterized by extremely narrow linewidths as a result. At 10 GHz, the FMR linewidth resulting from intrinsic damping in YIG crystals is roughly 0.2 Oe [84]. Compared to ferromagnetic

metals, this linewidth translates to an intrinsic damping constant α of roughly 3×10^{-5}, which is roughly two orders of magnitude smaller [88].

Since the 1960s, rare-earth iron garnet materials have been the subject of extensive research due to their unique spin dynamics and magneto-optical characteristics, including the capacity to change magnetization states. Because of its unusually low damping ($\approx10^{-5}$), low infrared absorption, and large Verdet constant—all of which are essential for Faraday rotators, isolators, and sensors—yttrium iron garnet ($Y_3Fe_5O_{12}$, YIG) has drawn the most attention of all the garnets. The potential application of YIG thin films in spintronics has sparked recent interest in them [40]. It is a desirable pure spin current source for the Seebeck effect and spin pumping at room temperature due to its low damping and high Curie temperature (≈560 ^{0}C). When compared to other magnetic insulators like $CoFe_2O_4$ [89], EuS, and EuO [90, 91], YIG has superior promise in several aspects. In contrast to permalloy, which has a magnon lifetime of the order of nanoseconds, it has the narrowest known FMR linewidth, resulting in a larger magnon lifetime of a few hundred nanoseconds. Spin currents can propagate over centimeter lengths in YIG because of its low damping [92]. Because of this, YIG is the preferred material for research on spin waves and magnetic insulator-based spintronics. Various substrates like Si, SiO_2, Quartz, GGG etc. are typically used to deposit yttrium iron garnet thin films, gadolinium gallium garnet (GGG) substrates (111) are typically preferred for the deposition of YIG thin film. With eight formula units per unit cell and a lattice constant of 12.383 Å, GGG has a cubic crystalline structure. Additionally, they have relatively similar thermal expansion coefficients ($1.04\times10^{-5}{}^0$/C). This enables nm-thick YIG films to grow epitaxially on a GGG substrate.

1.4 Magnetization dynamics

The time-varying reaction of the magnetization vector in magnetic materials to external fields, torques, or temperature changes is known as magnetization dynamics. The way magnetic moments precess, relax, and switch in response to applied excitations is

determined by this fundamental idea in magnetism and spintronics [93]. The Landau–Lifshitz–Gilbert (LLG) equation, which describes the precessional motion around effective magnetic fields and damping effects producing energy dissipation, provides the precise mathematical framework [94-96]. Designing spin-torque oscillators, magnetic sensors, high-speed magnetic memory systems, and next-generation technologies like magnonics requires an understanding of magnetization dynamics. The dynamic response of magnetic systems depends on both internal (such as anisotropy, exchange interactions, and damping) and external (such as applied fields, spin currents, or temperature gradients) factors [97].

1.4.1 Landau-Lifshitz-Gilbert (LLG) equation

The fundamental idea in spin dynamics is the precessional motion of magnetic moments. In 1935, Lev Landau and Evgeny Lifshitz created the Landau-Lifshitz (LL) equation, which is essentially a torque equation, for this precessional motion [95]. A dissipation term was added to the equation to take into consideration the damping in the system. Later on, Gilbert modified the equation to include a magnetic dampening element [94]. It is well known that an electron's spin can result in a magnetic moment that is connected to an angular momentum. The magnetic moment $\vec{\mu}$ and total angular momentum $\vec{J}$ connected with an expression

$$\vec{\mu} = \gamma \vec{J} \tag{1.1}$$

In above equation, γ denotes the gyromagnetic ration ($\gamma = \frac{g\mu_B}{h}$), where g denotes electron's Lande g-factor (g=2.0), μ_B and $\hbar = \frac{h}{2\pi}$ are the Bohr magnetron and reduced Plank's constant respectively. A magnetic moment in an effective magnetic field ($\vec{B}_{eff}$) is affected by a torque ($\vec{\tau}$).

$$\vec{\tau} = \vec{\mu} \text{ x } \vec{B}_{eff} \tag{1.2}$$

Due to the relationship between angular momentum ($\vec{J}$) and torque, the following equation can be used to characterize the equation of motion for angular momentum:

$$\frac{d\vec{J}}{dt} = \vec{\mu} \text{ x } \vec{B}_{eff} \quad (1.3)$$

In this equation $\vec{B}_{eff}$=μ_0 x H_{eff}, where, μ_0 is magnetic permeability in free space. The effectiveness of the magnetic field $\vec{H}_{eff}$ is defined as the sum of all internal and external magnetic field i.e written as $\vec{H}_{eff} = \vec{H}_a + \vec{H}_d + \vec{H}_m + \vec{H}_o + \vec{H}_{ex}$ where $\vec{H}_a$, $\vec{H}_d, \vec{H}_m, \vec{H}_o$ *and* $\vec{H}_{ex}$ are the anisotropy field, demagnetizing filed, external magnetic field, static field and exchange field respectively. In the continuum limit, the atomic magnetic moment may be replaced by the macroscopic magnetization M. There is a torque because of $\vec{H}_{eff}$. The magnetization experiences precession around the magnetic field as a result of torque. The Landau-Lifshitz (LL) equation describes such a precessional motion of magnetization:

$$\frac{d\vec{m}}{dt} = \gamma\mu_0 \text{ (M x } \vec{H}_{eff}) \quad (1.4)$$

According to the equation above, a non-dissipative system will never achieve equilibrium with $\vec{M}$ parallel to $\vec{H}$, which is in conflict with the system's actuality. Thus, the damping component was added to the equation of motion by Landau and Lifshitz in 1935 [95].

$$\frac{d\vec{m}}{dt} = -\gamma\mu_0 \text{ (M x } \vec{H}_{eff}) - \frac{\lambda}{M_S} [\vec{M} \text{ x } (\vec{M} \text{ x } \mu_0 \vec{H}_{eff})] \quad (1.5)$$

In this case, the damping constant with relaxation time ζ is λ=1/ ζ.

When damping is significant, this method may result in a high rate of precession. The viscous damping factor was phenomenologically introduced by Gilbert in 1955 as a solution to the problem. The ensuing Landau-Lifschitz-Gilbert (LLG) equation can be shown as follows [94],

$$\frac{d\vec{m}}{dt} = -\gamma\mu_0 \text{ (M x } \vec{H}_{eff}) + \frac{\alpha}{M_S} (\vec{M} \text{ x} \frac{d\vec{m}}{dt}) \quad (1.6)$$

A dimensionless Gilbert damping parameter called α is applied here. The first term is known as the precessional term, which describes how magnetization moves around the effective magnetic field in a steady condition with a Larmor frequency $\omega = \gamma\mu_0 \vec{H}_{eff}$ due to the torque ($\vec{M}$ x $\vec{H}_{eff}$).

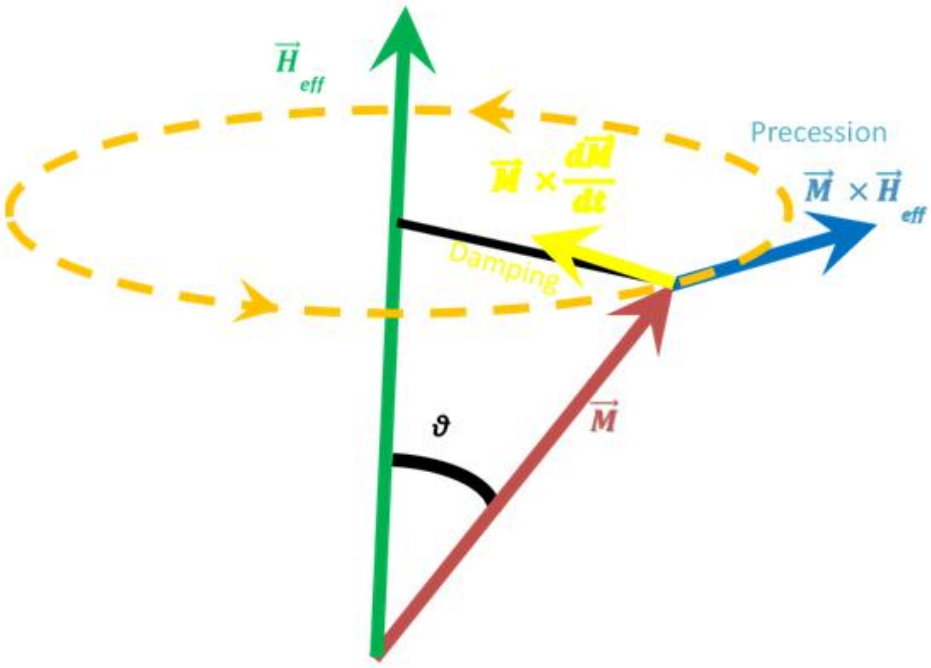

Fig:1.2 The precession of magnetization vector $\vec{M}$ around a magnetic field vector $\vec{H}_{eff}$ in the presence of precessional torque and damping torque.

The second term describes the relaxation of magnetization along the direction of the effective field and is known as the viscous damping term. In the fig. 1.2 shows that in the presence of damping torque and precessional torque, the magnetization vector $\overrightarrow{M}$ precesses around a magnetic field vector $\vec{H}_{eff}$. This damping term minimizes the energy by enabling the spin to travel in a helical trajectory toward the effective magnetic field. Stated differently, the precessional and damped motions are in a state of relaxation with the least amount of energy. The term "spin relaxation of magnetization" describes this. The spin-orbit interaction is frequently used to explain how energy and spin angular momentum are transferred from a magnon system to the phonons in a lattice because the damping torque is responsible for the dissipative processes in this process [98]. There are two types of relaxation mechanisms: intrinsic and extrinsic. Magnon-phonon coupling in the lattice is caused by extrinsic dampening processes including electron scattering and

magnon-magnon scattering. However, damping is naturally influenced by the spin-orbit interaction between phonons and magnons in the lattice. A key important requirement for spintronics is minimal Gilbert damping, which facilitates excitation and switching between various magnetic states and is essential for fast and energy-efficient spintronic memory devices.

1.4.2 Kittel equation

A fundamental relationship that provides the resonance condition in ferromagnetic materials when a magnetic field is applied is the Kittel equation. In 1948, Charles Kittel developed it, and it is frequently used in ferromagnetic resonance (FMR) studies to ascertain the magnetic properties of materials such as bulk samples, thin films, and multilayers [99]. The resonance frequency of magnetization precession is related to the applied magnetic field and the intrinsic magnetic properties of the material, such as anisotropy fields and saturation magnetization, according to the formula. By determining how the magnetic moments respond dynamically to external perturbations, the Kittel equation provides insight into the material's internal interactions, damping, and magnetic anisotropy [100]. By linearizing the LLG equation and determining the frequency ($\omega \; or \; f$) at which maximal absorption takes place, the precise FMR condition is obtained. The most well-known outcome is the Kittel equation, which in its general form for an ellipsoid (which can assume different forms by changing dimensions), is

$$\omega^2 = \gamma^2\left[H_{res} + \left(N_y - N_z\right)M_s\right]\left[H_{res} + (N_x - N_z)M_s\right] \tag{1.7}$$

In the above equation, $\omega = 2\pi f$, is the angular frequency.

H_{res} is the applied resonance magnetic field,

N_x, N_y and N_z are the demagnetization factor along the primary axes which, depend completely on the dimensions and shape of the samples.

The equation is frequently expressed as follows for thin films where the magnetic field is applied in-plane [101],

$$\omega_0 = \gamma\sqrt{[H(H + 4\pi M)]} \tag{1.8}$$

The resonance condition arises when the frequency of the applied alternating magnetic field matches the natural precession frequency of the magnetic moments around the effective magnetic field direction. The anisotropy field H accounts for magneto crystalline and shape anisotropies, while M influences the internal demagnetizing field. This relation enables the extraction of critical parameters such as saturation magnetization Ms, Anisotropy constants, Damping behavior via linewidth analysis. The Kittel equation is widely used in experimental FMR measurements to fit resonance data and derive material properties. Kittel equation is described broadly with FMR in next section.

1.4.3 Ferromagnetic resonance (FMR)

Griffiths was the first to observe microwave absorption by ferromagnetic films at a resonance frequency distinct from the electron spin's Larmor frequency in 1946 [101]. Theoretically, Kittel later explained these phenomena as ferromagnetic resonance in magnetic material [108, 109]. An analogy of this FMR phenomena is electron paramagnetic resonance (EPR) [103]. The foundation of EPR is the Zeeman effect, which happens when an atom with a free electron is exposed to a magnetic field and the energy levels of the electrons are separated using the energy splitting formula, $\Delta E = g\mu_B H$. Fig. 1.3 shows the resonance spectrum that is produced when a material absorbs energy ($E = h\nu$) from an applied rf-magnetic field, causing resonance ($h\nu = g\mu_B H$). In both ferromagnetic resonance (FMR) and electron paramagnetic resonance (EPR), when exposed to an rf magnetic field (h_{rf}), the elementary magnetic moments precess around an external magnetic field (H). With the same frequency and phase, the magnetic moments precess coherently. The dynamics of magnetization in uniform precession are described

by the LLG equation. The g-factor, Gilbert damping parameter, magnetic anisotropies, and other characteristics of magnetic materials can all be estimated using FMR data. The key parameters utilized in the investigation of FMR data are the location of the resonant field (Hr) and the line-width (ΔH) of the acquired absorption spectra. In order to determine the resonance frequency in terms of ΔH and Hr, the LLG equation is interpreted for lesser magnetic field in the next paragraph. The primary emphasis of FMR data analysis is the magnetic response of a ferrimagnet to time-varying magnetic fields. FMR involves applying two magnetic fields to a sample while it is being measured. In a FMR experiment, a high-frequency magnetic field (h_{rf}) is used to induce the magnetization precession after a dc magnetic field (H) saturates the magnetization (M_s) in the direction of H. Fig. 1.4 shows a microwave field originating from a waveguide stimulates a sample.

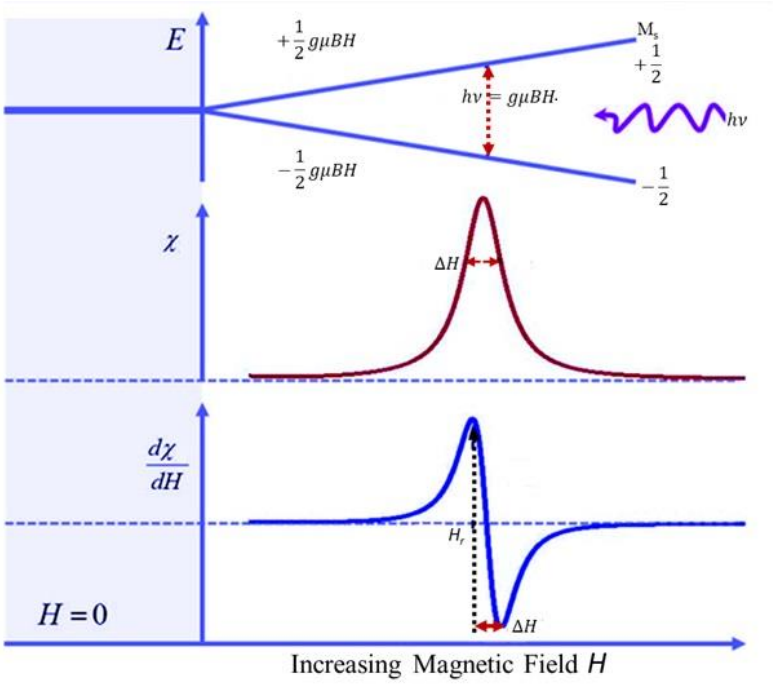

Fig. 1.3 The energy levels and resonances of free electrons are illustrated at zero and increasing applied magnetic field (H). In this figure, the spacing between energy levels increases as the magnitude of the magnetic field increases (χ is magnetic susceptibility) [104].

The magnetic moment's response to this stimulus is determined by the magnetic susceptibility, which may be calculated by applying the LLG-equation in this case. A saturation of magnetic moments (M_s) in the y direction is caused by an applied dc field. The microwave field h causes precessional motion, which results in smaller time harmonic components m_z and m_x in the z and x direction, respectively. The expression for the magnetization vector can be written as [101],

$$\vec{M} = M_x\hat{x} + M_s\hat{y} + M_z\hat{z} \tag{1.9}$$

Whereas the effective magnetic field may be written as [101],

$$\vec{H}_{eff} = \vec{H} + \vec{H}(t) + \vec{H}_k + \vec{H}_d \tag{1.10}$$

In this case, external contributions are represented by the first two terms, specifically the rf field $\left(\vec{h}(t) = h_x\hat{x} + h_z\hat{z}\right)$ and applied dc field $\left(\vec{H} = H\hat{y}\right)$. The final term represents the demagnetizing field ($\vec{h}_d = -M_z\hat{z}$) that reduces the dipole magnetic moment in the film, whereas the other two terms are thought of as internal contributions, or an out of plane contribution, as a result of magnetic anisotropy $\left(\vec{h}_k = \frac{H_k}{M_s} - M_z\hat{z}\right)$. It is commonly known that the LLG-equation solution can be obtained by applying the linear approximation while ignoring second order components, and by entering the values of M and H_{eff} into the LLG-equation (1.6). The solution to the LLG equation is expressed as [101],

$$\begin{pmatrix} h_x \\ h_z \end{pmatrix} = \frac{1}{\gamma\mu_0 M_S}\begin{pmatrix} \gamma\mu_0 H - i\omega\alpha & i\omega \\ i\omega & \gamma\mu_0(H+M_S-H_K)-i\omega\alpha \end{pmatrix}\begin{pmatrix} m_x \\ m_z \end{pmatrix} \tag{1.11}$$

The above-mentioned equation (1.10) may be converted in to the Polder susceptibility tensor $\left(\bar{\bar{\chi}}\right)$ form and it may be written as $m = \bar{\bar{\chi}}h$ in this equation h is applied rf field. Fig. 1.4 indicates that h is in the direction of x, hence, only the one component χ_{xx} is suitable, which is written as [101],

$$\chi_{xx} = \frac{M_S\left(H+M_{eff}-\frac{i\omega\alpha}{\gamma\mu_0}\right)}{H(H+M_{eff})-\frac{\omega^2}{\gamma^2{\mu_0}^2}-\frac{i\Delta H}{2}(2H+M_{eff})} \quad (1.12)$$

In this case, $\Delta H = \frac{2\omega\alpha}{\gamma\mu_0}$ here, $\omega = 2\pi f$ and α is known as gilbert damping constant. Effective magnetization is M_{eff}, equals to $(M_S + H_K)$. To assess the thin film sample's effective magnetization and damping, we must first determine a relationship between the absorption peak's linewidth, resonance field, and susceptibility.

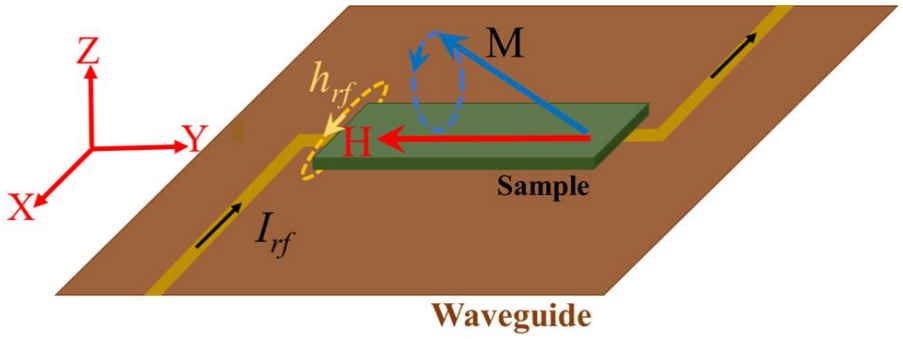

Fig. 1.4 Microwave current passing through the waveguide induces a microwave field in the sample, which drives Larmor precession

When the absorption peak reaches at its maximum, which happens when the denominator of the imaginary component of χ_{xx} becomes close to zero, the system is in resonance [101].

$$\left[H\left(\mathrm{H}+M_{eff}\right)-\left(\frac{\omega}{\gamma\mu_0}\right)^2\right]^2+\left[\Delta H\left(H+\frac{1}{2}M_{eff}^2\right)\right]^2=0 \quad (1.13)$$

This can be recast in the below form, based on the assumption that $\Delta H^2 \ll H_r^2$ [101],

$$f_r = \frac{\gamma}{2\pi}\mu_0\sqrt{(H_r)(H_r+M_{eff})} \quad (1.14)$$

It is known as the Kittel equation. Consequently, it may be used to determine a sample's effective magnetization (M_{eff}) by fitting the frequency to a resonance field (H_r) after

doing a broadband measurement of the resonance peak for various applied frequencies (f). Above equation is very much useful in the field of spintronics study to determine the various parameters of the thin film samples.

Damping parameters of the thin film samples can be calculated from the absorption data of FMR. From the absorption data we can calculate the line width and resonance field. By using the value of line width in the following equation to determine the damping parameters [105].

$$\Delta H_f = \Delta H_0 + \frac{4\pi\alpha}{\gamma\mu_0} f \tag{1.15}$$

The offset ΔH_0 accounts for the several resonances that surround the peak's center due to the sample's inhomogeneities. Equation (1.14) demonstrates that when the applied frequency rises, the line width increases linearly, with the damping controlling the slope. By taking measurements across a wide frequency range and fitting the linewidth to the resonance frequency, one can ascertain the damping of a material. Ferromagnetic resonance (FMR) in conjunction with a force microscope or a vector network analyzer (VNA) allows for a thorough examination of the dynamic magnetic response of thin films [106]. By measuring the material's reaction to microwave fields across a variety of frequencies, a VNA-FMR system can provide details on characteristics like effective saturation magnetization and damping. By detecting the forces generated by the magnetic sample inside a non-uniform magnetic field gradient, Magnetic Resonance Force Microscopy (MRFM) offers high-resolution, local observations [107].

34

1.4.4 Spin pumping

Spin pumping is a process where the dynamic magnetization of a ferromagnetic material creates a pure spin current into a neighbouring nonmagnetic layer without any accompanying charge current. When the ferromagnet is excited into precession, for

example, via ferromagnetic resonance (FMR), the angular momentum transfer at the interface results in the emission of a spin current into the surrounding material [14].

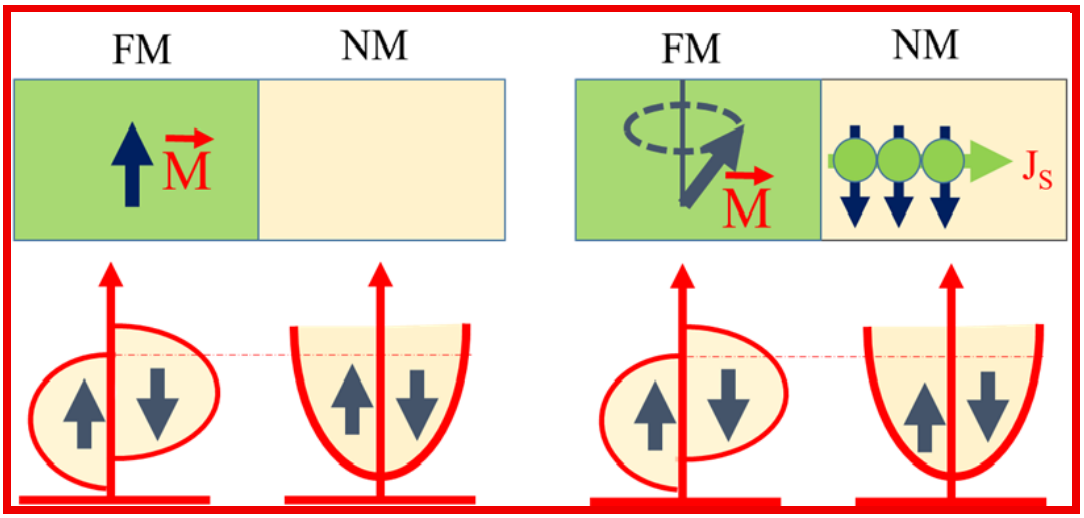

Fig. 1.5 Spin pumping in a ferromagnetic (FM)/normal metal (NM) bilayer structure [108].

This procedure relies on the effectiveness of interfacial coupling, measured by the spin mixing conductance, and leads to an extra damping of the magnetization dynamics of the ferromagnet. Spin current pumped into heavy metals such as Pt is transduced to a detectable charge current through the inverse spin Hall effect (ISHE) and thus spin pumping has become a key means of studying spin–charge interconversion phenomena and spintronic devices including spin-based logic and memory devices [14,18]. Spin pumping is especially significant in systems such as YIG/metal heterostructures, where low intrinsic damping permits efficient detection and generation of spin currents at interfaces. To demonstrate the spin pumping phenomenon in the bilayer structure of ferromagnetic (FM) and normal metal (NM) a schematic is shown in fig. 1.5. The orientation of the magnetization in the FM layer is indicated by the magnetization vector $\vec{M}$, which is shown by an arrow. In fig. 1.5 bottom diagram shows the band image, vertical

arrows show the directions of the electronic magnetic moments. The electrons in both layers are at the same Fermi level as long as the FM layer's magnetization remains static. The FM layer uses the magnetization vector's precession to transfer angular momentum to the NM layer. The spin current produced in the NM layer causes a difference in the chemical potential between electrons spinning up ($\mu_\uparrow$) and down ($\mu_\downarrow$). This phenomenon known as spin pumping [14,109]. Assume that the tiny spheres in the NM layer represent the electrons, and that the arrow across each sphere indicates the direction of the electron magnetic moment. Spin voltage, also known as spin accumulation which is the term used to describe the chemical potential differential $\mu = (\mu_\uparrow - \mu_\downarrow)$. The equation given below defines a spin current density vector.

$$\vec{J}_S = \frac{\hbar}{4\pi}\Re(g_{\uparrow\downarrow})\vec{M} \times \frac{\partial \vec{M}}{\partial t} \tag{1.16}$$

In equation (1.15), real component of spin mixing conductance is denoted by $\Re(g_{\uparrow\downarrow})$, which is the effectiveness of the transfer of spin current across the FM-NM layer interface. The spin current density is the net angular momentum that moves from the magnetization $\vec{M}$ in the FM layer to the electrons in the NM layer over a unit area in a unit amount of time. The momentum transfer can be described as resulting in an increase in the damping constant of the FM layer.

$$\alpha_{SP} = \frac{g\mu_B}{4\pi M_S}\frac{\Re(g_{\uparrow\downarrow})}{d} \tag{1.17}$$

In the above equation g and d stands for Bohr magnetron and FM layer thickness respectively, whereas g and M_S represents Landé factor and saturation magnetization respectively. Since the additional damping caused by spin pumping is more important in thinner films, the actual Gilbert damping value is inversely related to the thickness of the magnetic layer [14].

1.4.5 Spin transfer torque

In 1996, Slonczewski suggested a novel method for ferromagnet magnetic state [110]. One of the fundamental techniques of spintronics, spin transfer torque (STT) uses spin-polarized electrical currents to control magnetization in ferromagnetic materials. Conduction electrons become spin-polarized when an electric current flows through a ferromagnetic layer because their spins align with the layer's magnetization. The angular momentum of these spin-polarized electrons is transferred to the local magnetic moments if they move into another ferromagnetic layer with a different magnetization direction. This torque reorients or switches the magnetization of the material [110,111]. Below equation derived by Slonczewski from the LLG equation in 1996 [94].

$$\frac{dM}{dt} = -\gamma M \times H + \frac{\alpha}{M_S} M \times \frac{dM}{dt} - \frac{\gamma \hbar \mu_0}{2VM_S} M \times (M \times I_S) \tag{1.18}$$

In the above equation final term is added in 1996 by Slonczewski and it characterize how the magnetization reacts to current I_S flows in to the magnet (keep in mind that I_S not in the direction of the current flow rather in the direction of spin polarization). Because of the torque-like nature of this term, the influence of Is on M is referred to as spin-transfer torque (STT). Consequently, a ferromagnet's magnetization can be reoriented using a spin current.

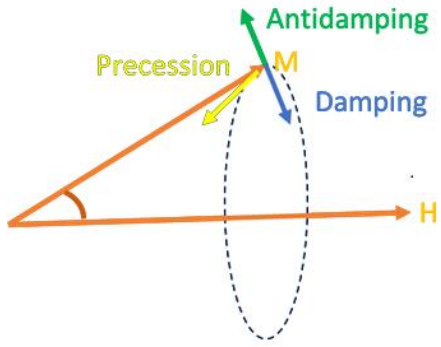

Fig.1.6 Demonstration of the term M and H [117].

In the above fig. 1.6 in the direction of the yellow arrow, the magnetization M precesses around the effective magnetic field H (shown by the dotted line trajectory). M is pushed toward its equilibrium orientation, which is parallel to H, by Gilbert damping. Depending on whether spin-transfer torque acts anti-parallel (green) or parallel (blue) to the damping term, the precessional cone angle will either increase or decrease.

The polarization of the spin current determines the torque's direction. The angle between M and H, also known as the cone angle or precessional angle, can either be reduced or increased depending on whether it operates parallel to or anti-parallel to the damping term. The effects of the various variables in the LLG equation on the magnetization are schematically depicted in fig. 1.6. The STT acting anti-parallel to the damping can be used to completely compensate for the Gilbert damping, which causes the magnetization to oscillate [112], or it can even cause a complete reversal of the magnetization [113,114]. These effects can also happen in magnetic insulators like YIG since STT just requires a spin current to flow into a magnet. There have been recent reports of spin torque magnetization switching of an insulating thulium iron garnet layer and auto-oscillations of microdisk caused by spin transfer torque [115]. In both situations, the effect produced by the SHE in the Pt layer on top of the magnet is driven by spin current. Spin-Transfer Torque Magnetic Random-Access Memory (STT-MRAM), which encodes data inside the magnetic direction of a nanostructured device, is the most widely studied application. High-speed and low-power memory operation is made possible by STT's ability to toggle the state of the free layer magnetization by passing a spin-polarized current [116].

1.4.6 Spin orbit torque

One of the keys spintronics phenomena that regulates the magnetization of ferromagnetic materials through spin-orbit coupling phenomena is spin-orbit torque (SOT). SOT results from the coupling between an applied charge current and the internal spin–orbit coupling within heavy metals or topological materials adjacent to the ferromagnet, as opposed to

spin transfer torque, which is mediated by spin-polarized currents from a ferromagnet [118,119]. Through processes like the spin Hall effect (SHE) or the Rashba–Edelstein effect, intense spin–orbit coupling produces a transverse spin current when an electric current passes through a heavy metal (such as tantalum, tungsten, or platinum). Magnetization switching, domain wall movement, or oscillations without external magnetic fields can result from this interface spin accumulation's torque on the magnetization of the nearby ferromagnetic layer [119,120]. Often the torque generated by SOT can be divided in to two parts, Damping-like torque opposes or orients the magnetization's precession in a direction perpendicular to the direction of magnetization, field-like torque acts similarly to an effective magnetic field. Given equation derived from the LLG equation [94, 121],

$$\frac{dM}{dt} = -\gamma M \times H + \alpha M \times \frac{dM}{dt} + \frac{J_{ex}}{\hbar} M \times m \qquad (1.19)$$

In this equation, γ is gyromagnetic ratio, H is effective field and α is gilbert damping, last term of above equation is known as current induce spin torque. SOT has enabled advances in spintronic devices, especially in high-speed, energy-efficient memory and logic devices such as. The Spin-Orbit Torque Magnetic Random-Access Memory, or SOT-MRAM, offers low switching currents and fast, nonvolatile memory. Devices based on domain walls: SOT regulates the movement of magnetic domain walls for memory or logic bits and Signal processing can be done with oscillators and neuromorphic computing components, which employ the magnetization dynamics brought on by SOT.

1.4.7 Spin current and spin diffusion

A spin current is the flow of spin. This performs similarly to how charge moves in an electrical current. The movement of spin angular momentum, often by conduction electrons with polarized spins in a particular direction, is known as a spin current. Unlike charge current, which must accompany net charge flow, spin current can be generated through a variety of methods, such as spin injection, spin pumping, or the spin Hall effect [8]. When spin-polarized electrons traverse a material, they lose their spin orientation with

distance as a result of scattering due to impurities, phonons, or other scattering mechanisms. The process is identified as spin diffusion that accounts for how spins relax and become spread out in space as they flow through the material [50]. There is internal angular momentum in an electron. The electron's spin is what causes this angular momentum. Here, we discuss about the charge current, the charge conservation law is used to define a charge current. A charge current density (J_c) is defined by the continuity equation of charge, which is a representation of the charge conservation law [122].

$$\dot{\rho} = -\nabla \cdot J_c \tag{1.20}$$

But because of spin relaxation, spin is not entirely conserved and follows the continuity equation [123].

$$\frac{dM}{dt} = -\nabla \cdot J_s + T \tag{1.21}$$

In this equation, $J_s$is the spin current density and M is the magnetization. The relaxation and creation of spin angular momentum result in nonconservation of spin angular momentum, which is represented by the T. The spin relaxation's fundamental phenomenological model is described as [123].

$$T = \frac{-(M-M_0)}{\tau} \tag{1.22}$$

In above equation $(M - M_0)$ is the nonequilibrium magnetization as determined from the equilibrium value M_0 and τ is a decay time constant. In case of heterostructure, it is possible to inject a spin current from a ferromagnet (FM) into a normal metal (NM) in the bilayer structure arrangement. A spin current at an FM/NM junction with a charge current flowing through the interface is depicted in fig. 1.7 An electrochemical potential gradient between spin up ($\mu_\uparrow$) and spin down ($\mu_\downarrow$) is the driving factor for a diffusion or drift spin current. This allows us to express the charge current density J_c and spin current density J_s as [123].

$$J_c = J_\uparrow + J_\downarrow = \frac{1}{e}\nabla(\sigma_\uparrow \mu_\uparrow + \sigma_\downarrow \mu_\downarrow) \quad (1.23)$$

$$J_s = J_\uparrow - J_\downarrow = \frac{1}{e}\nabla(\sigma_\uparrow \mu_\uparrow - \sigma_\downarrow \mu_\downarrow) \quad (1.24)$$

In this case, the spin down and spin up conductivity are represented by $\sigma_\downarrow$ and $\sigma_\uparrow$, respectively.

In the steady state, the continuity equations for spin and charge are given below,

$$\nabla \cdot (J_\uparrow + J_\downarrow) = 0 \quad (1.25)$$

$$\nabla \cdot (J_\uparrow - J_\downarrow) = -e\frac{\delta n_\uparrow}{\tau_{\uparrow\downarrow}} += e\frac{\delta n_\downarrow}{\tau_{\uparrow\downarrow}} \quad (1.26)$$

where $\delta n_{\uparrow(\downarrow)}$represents the spin up (spin down) divergence from equilibrium carrier density and $\tau_{\uparrow\downarrow}$ represents the electron's scattering time from spin state ↑ to ↓ or vice versa. Because there is no net spin scattering in equilibrium, the continuity equations and the balance principle $\frac{N_\uparrow}{\tau_{\uparrow\downarrow}} = \frac{N_{\uparrow\downarrow}}{\tau_{\uparrow\downarrow}}$ allow us to derive the fundamental equations describing the charge and spin transport as [123].

$$\nabla^2(\sigma_\uparrow \mu_\uparrow + \sigma_\downarrow \mu_\downarrow) = 0 \quad (1.27)$$

$$\nabla^2(\mu_\uparrow - \mu_\downarrow) = \frac{1}{\lambda_{sd}^2}(\mu_\uparrow - \mu_\downarrow) \quad (1.28)$$

Above equation (1.27) recognized as the spin diffusion equation. In this case, λ_{sd} may be written as $\sqrt{D}\tau_{sf}$, which is known as spin diffusion length, in this expression τ_{sf} is the spin relaxation time and D is the spin-averaged diffusion constant.

When a spin-polarized current enters a normal metal at an FM/NM junction, the chemical potentials for the spin up and spin down diverge over a short period, causing spin accumulation in the NM. In nonmagnetic metals, the charge current has lack of spin polarization and the electrical conductivity is spin-independent. Consequently, the spin

diffusion length defines the spatial axis over which the non-conservation of spin current occurs.

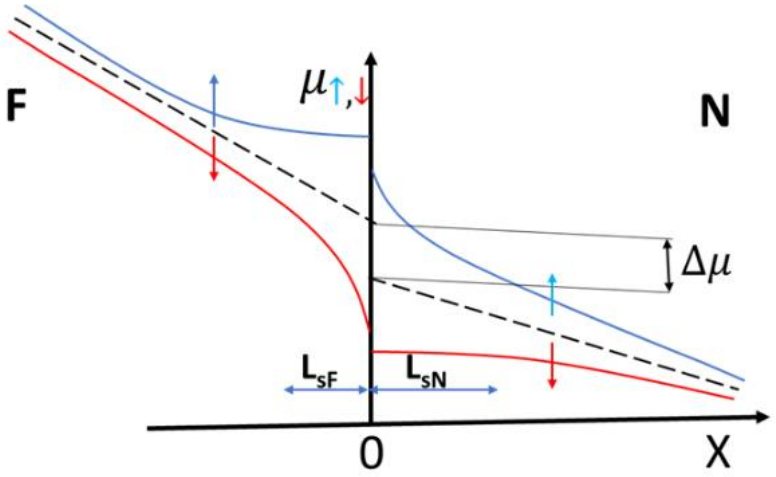

Fig: 1.7 At a ferromagnet/normal metal (FM/NM) junction, the spin-dependent electrochemical potentials vary spatially over a current-carrying interface. The spin diffusion lengths L_{sF} and L_{sN} in the FM and NM areas, respectively, define the decay of spin accumulation away from the interface [8].

The chemical potentials must be constant when the conduction electrons enter the NM, although there may be a slight variation because of the interface contact resistance. The spin accumulation is represented by $\Delta\mu$, which is the gap between the dotted lines indicated in fig. 1.7. Away from the interface, the spin accumulation $(\mu_{\uparrow} - \mu_{\downarrow})$ decays into the FM and NM regions. Over a spin diffusion length L_{sN}, this spin accumulation decays in the NM. The accumulation in the NM causes a backflow of spin-polarized electrons over a distance L_{sF} in the FM close to the interface. Understanding of this phenomenon is important for the application in the field of devices such as spin valves magnetic tunnel junctions, spin-based logic and communication system, spin hall effect-based devices etc.

1.4.8 Spin back flow

A fundamental consequence of spin transport in magnetic heterostructures is spin backflow, which happens when a spin current generated by a ferromagnet's dynamic magnetization is partially reflected at the boundary with a non-magnetic layer. In their theory for the description of spin pumping in thin ferromagnetic films, Tserkovnyak, Brataas, and Bauer (2002) presented the spin backflow [14]. In spin pumping, the nearby non-magnetic metal receives a spin current from the ferromagnet's oscillating magnetization. However, some of this spin current is reflected back into the ferromagnet due to the finite spin mixing conductance and spin buildup on the interface. In spintronic devices like spin-torque oscillators and magnetic random-access memory (MRAM), this reflected part, also known as spin backflow, has a significant impact on both the effective spin current and the magnetic damping. The spin mixing conductance $g_{\uparrow\downarrow}$ and the spin accumulation at the interface regulate the pumped spin current and the backflow component, which together make up the total spin current at the FM/NM interface. The schematic to understand the spin back flow is shown in the fig. 1.8 [14].

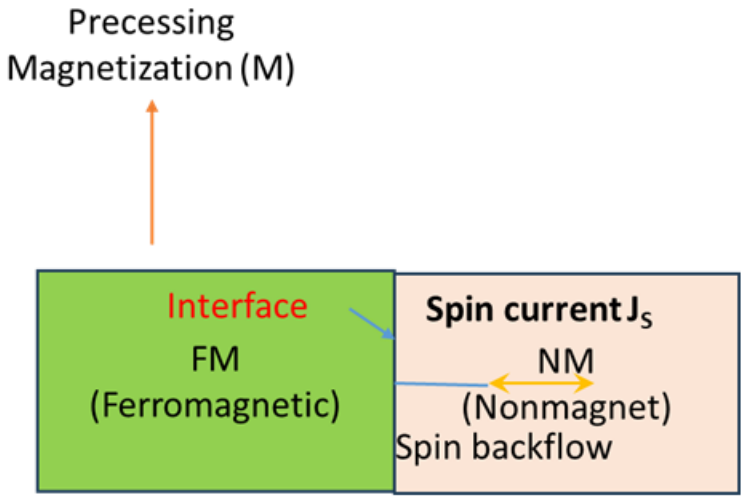

Fig. 1.8 Schematic to represent the spin back flow [14].

The following is an expression for the spin current density injected into the non-magnetic layer [14],

$$J_s^{pump} = \frac{\hbar}{4\pi} g_{\uparrow\downarrow}(m \times \dot{m}) \quad (1.29)$$

In this case, $g_{\uparrow\downarrow}$ is the spin mixing conductance, $\hbar$ reduced Plank's constant, m is the unit vector along the magnetization direction and $\dot{m}$ is the dime derivative of m. On the other hand, diffusive backflow current J_s^{back} due to spin accumulation at the interface emerges and can be expressed as,

$$J_s^{back} = \frac{\hbar}{4\pi} g_{\uparrow\downarrow}(m \times (m \times \mu_s) \quad (1.30)$$

In the above equation, μ_s is the spin accumulation at the interface. Therefore, the total spin current $J_s = J_s^{pump} + J_s^{back}$. The total spin current injected into the non-magnetic layer is effectively decreased by this backflow term, which also causes the damping constant seen in ferromagnetic resonance investigations to renormalize. Through the delivery of angular momentum into the non-magnetic layer, the spin pumping technique improves the effective ferromagnetic damping. However, finite spin buildup and defective contacts reverse the effect, reducing the net angular momentum transmission and reflecting spin current. Spin backflow depends on the spin mixing conductance, spin accumulation and spin diffusion length. For accurate ferromagnetic resonance linewidth interpretation, optimized interface properties, and increased energy efficiency in spintronic devices, spin backflow is essential. Spin backflow has its impact on improvement in ferromagnetic resonance dampening, effectiveness of injecting spin onto adjacent layers and performance of spintronic devices, such as spin-torque oscillators and MRAM [14].

27

1.4.9 Spin hall effect and inverse spin hall effect

The spin Hall effect (SHE) is the phenomenon where an electric charge current generates a transverse spin current with spins aligned perpendicular to both the current directions.

Since spin-orbit coupling (SOC) produces a transverse electric field, electrons with up and down spin can scatter in opposite directions perpendicular to the electric current. Fig. 1.9 (a) illustrates how this produces the spin up and spin down currents along a material's two opposing edges. In this case, the relativistic spin orbit coupling (SOC) plays the role of the magnetic field. In 1971, D'yakonov and Perel made a theoretical prediction about the SHE [124]. Inverse SHE (ISHE), a physical phenomena where a normal metal's spin current generates a transverse electric charge current, is the reciprocal effect of SHE (fig. 1.9 (b)).

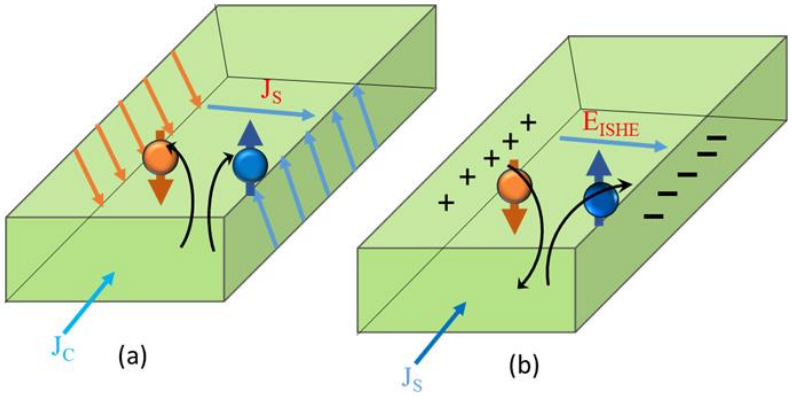

Fig. 1.9 (a) The spin Hall effect (SHE) causes a spin polarized current to be produced perpendicular to the charge current in a typical metal. (b) the inverse of SHE, which is also known as reciprocal of SHE, where a charge current is generated perpendicular to a spin-polarized current [125].

These two effects are related to the charge and spin of electrons, and they can be reversibly converted into each other. SHE and inverse SHE have been quantitatively measured and studied in a range of systems, including metals like Al and Pt and semiconductors like ZnSe and GaAs [124]. The interactions between spin orbits produce the spin Hall effect. The impurity potential creates an extra electric field when an electron travels through a

solid, and this additional field serves as an efficient magnetic field for the electron. Consequently, a spin orbit coupling (SOC) exists, which is defined as,

$$H_{SO}(k) = -\frac{1}{2}\sigma B(k) \tag{1.31}$$

In this case, σ represents the Pauli spin matrix vector, while $B(k)$ represents the effective magnetic field for the electron band in consideration in terms of k. This has the effect of causing spin-dependent perturbations to the conduction electron momentum. Furthermore, according to the paradigm, the SHE is categorized as intrinsic or extrinsic. The spin-dependent band structure of the material is linked to the intrinsic spin hall effect. The precession of spins around the suitable magnetic field B(k), which establishes the band structure, contributes to the intrinsic spin hall effect [126]. In metals, intrinsic effects can be disregarded because extrinsic effects are more common.

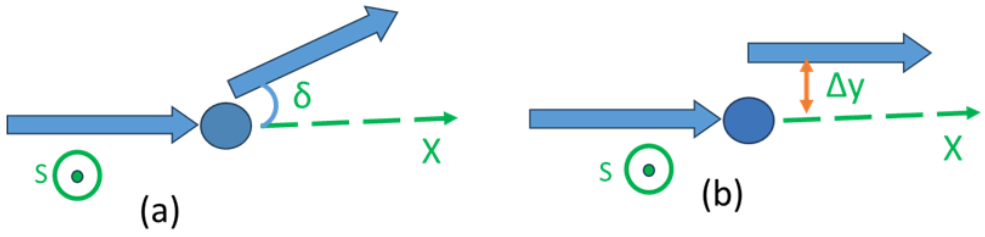

Fig. 1.10 average velocity of an electron after spin-orbit interaction and central potential scattering. (a) An angle δ deflects the trajectory after it collides with the impurity. (b) Diagram of the mechanism for side jumps. The spin (S) of the electrons is normal to the plane [127].

Because heavy metals like Pt have been used in both spin pumping and ISHE experiments, an emphasis on extrinsic effects is required. Based on the spin-orbit interaction between the crystal's particles, extrinsic methods can be divided into two categories: side-jump methods and skew scattering. When a central potential disperses electrons with asymmetric spin up and spin down distributions from the centre, skew scattering takes

place. A schematic depiction of the skew scattering mechanism is shown in fig. 1.10 (a). An angle deflects the electrons' path after they scatter from an impurity. This collision creates spin polarization using a polarized electron beam. Skew scattering's contribution to the spin Hall (SH) conductivity is determined by [127],

$$\sigma_{SS}^{SH} = \sigma_s \rho_{ss} \sigma_c \tag{1.32}$$

In this case, the spin conductivity is represented by σ_s, and Drude's conductivity by σ_c. In the context of effective mass m*, electron density η, electronic charge e and skew scattering rate $\frac{1}{\tau_{ss}}$, ρ_{ss} is resistivity which is written as $\rho_{ss} = \frac{m^*}{(\eta e^2 \tau_{ss})}$. Due to the anomalous nature of the velocity operator, spin-orbit coupled systems experience the side-jump process (fig. 1.10 (b)) [127]. It is described as a discontinuous transverse displacement of electrons (represented by a wave packet). Random collisions between electrons and impurities are the cause of this trend. The jump can occur in any direction and does not have to be transverse to the direction of the incident wave. The comparable displacement of up-spin and down-spin electrons in opposite directions results in the induced spin current transverse to the initial unpolarized charge current. The SH conductivity caused by the side jump mechanism is calculated using the following formula [128].

$$\sigma_{SS}^{SH} = -2\frac{e^2}{\hbar}\eta\lambda_c^2 \tag{1.33}$$

In the above equation, λ_c represents the coupling constant of conduction band. Consequently, the SH conductivity is composed by combining two more terms, namely,

$$\sigma^{SH} = \sigma_{SS}^{SH} + \sigma_{SJ}^{SH} \tag{1.34}$$

Additionally, electrical resistivity ρ has a squared and linear dependant term for the SH resistivity ρ_H [129].

$$\rho_H = \alpha_{skew}\rho + b_{side}\rho^2 \quad (1.35)$$

Temperature-dependent variables b_{side} and α_{skew} are utilized to define the side jump mechanism and skew scattering processes, respectively. The symbols for the charge current density J_C and spin current density J_S are correspondingly. The relationship of these two current densities is demonstrated by the following equations [129],

$$J_C = J_C^0 + \theta_{SHE}\frac{2e}{\hbar}(J_S \times \sigma) \quad (1.36)$$

$$J_S = J_S^0 + \theta_{SHE}\frac{2e}{\hbar}(J_C \times \sigma) \quad (1.37)$$

In this case, σ represent the spin polarization vector whereas J_S^0 and J_C^0 denotes the initial current densities. The spin Hall angle is represented by the material-dependent parameter θ_{SHE}. The combined effects of side-jump and skew scattering mechanisms provide the framework of the θ_{SHE}. Additionally, θ_{SHE} is defined as the "spin conductivity to electrical conductivity ratio" and is employed in the analysis of the SHE. According to equations (1.35) and (1.36), the spin current induces a transverse charge current, and vice versa. Converting the spin current produced by spin pumping into charge current is in the hands of the ISHE. One can obtain an average current density by averaging the Pt thickness d_{Pt} over the value of J_S, which can be obtained from the literature [130].

$$\overline{J_C} = \theta_{SHE}\frac{2e}{\hbar}\frac{\lambda_{sd}}{d_{Pt}}tanh\left(\frac{d_{Pt}}{2\lambda_{sd}}\right)J_S^0 \quad (1.38)$$

In the above equation (37), spin diffusion length of Pt denoted by λ_{sd}. The ISHE charge current can be expressed as $I_{ISHE} = A\overline{J_C}$, where A is the Pt layer's cross-sectional area. Consequently, $V_{ISHE} = I_{ISHE} \times R$, where R is the Pt layer's electrical resistance, is the ISHE's voltage. The development of spin-transfer torque devices, which use spin currents to alter magnetization, depends heavily on both SHE and ISHE. Spin currents enable low-power operation in magnetic random-access memory (MRAM). Spin-based logic circuits

and spin caloritronic, which use thermal gradients to generate observable spin currents through ISHE, offer novel approaches to information processing [131].

1.5 Objective of the thesis

The primary objective of the current thesis is to develop and thoroughly investigate multilayer heterostructures and thin films based on ferromagnetic and noble metals that develop using a variety of physical vapor deposition (PVD) techniques. These include DC and RF Sputtering and Pulsed Laser Deposition (PLD) techniques. The study is primarily focused on understanding the growth processes, structural changes, interfacial properties, and magnetic dynamics of these thin films as well as exploring their potential applications in the emerging field of spintronics. Yttrium Iron Garnet (YIG) has been chosen as the ferromagnetic material in this case because of its remarkable magnetic features, which include low Gilbert damping, high Curie temperature, and outstanding magnetic insulation behavior. Because of these qualities, YIG is a perfect platform for studying spin pumping effect and other spin transport phenomena. NiO as an antiferromagnetic material, whereas for heterostructures Pt, Cu and W considered as a nonmagnetic material for the development of multilayer structures.

The research objectives have been formulated based on a comprehensive literature review, which found that while spintronics has made significant progress, there are still unanswered questions about how deposition parameters, interfacial quality and multilayer configuration affect spin current propagation and damping mechanisms. The present study has been designed to systematically address these research gaps and the potential technological impact of spintronic materials. In in the context of this, the following are the objectives of this thesis:

1. Extensive literature survey on ferromagnetic/ nonmagnetic metal based thin films and their multilayer heterostructures for the application in the field of spintronics.

2. Optimization for development of magnetic thin film of yttrium iron garnet (YIG) using pulsed laser deposition (PLD) system and to study the effect of deposition parameters.
3. Study the spin pumping effect of YIG by development of multilayer heterostructures of $FM_1/NM/FM_2$ and FM/NM/AFM using PLD and sputtering techniques.
4. Study the spin pumping effect of YIG by development of multilayer heterostructures of FM/NM, $FM/NM_1/NM_2$ and $FM/NM_1/NM_2/NM_3/NM_4$ using PLD and sputtering techniques.
5. Detail investigation of magnetization dynamics of fabricated bilayer, trilayer and multilayer thin films using ferromagnetic resonance spectroscopy (FMR).
6. Investigation of microwave devices such as band stop filter, phase shifter an isolator using YIG thin films.

The optimization of deposition parameters and the methodical creation of magnetic thin films and multilayer heterostructures for spintronic applications have been the main focuses of the current research project. The main objective of the study is to use the Pulsed Laser Deposition (PLD) technique to fabricate and optimize yttrium iron garnet (YIG) thin films. YIG is an excellent candidate material for studying spin transport and magnetization dynamics phenomena because it is a ferrimagnetic insulator with a high Curie temperature and exceptionally low magnetic damping. To produce high-quality epitaxial YIG films with enhanced crystallinity, surface morphology, and magnetic properties, considerable experimental effort has been focused on fine-tuning the deposition parameters, such as substrate temperature, oxygen partial pressure, laser fluence, and target-to-substrate distance.

33

The research goes beyond the development of single-layer films to include the development of multilayer thin-film structures made of ferromagnetic/metal and ferromagnetic/metal/antiferromagnetic combinations. In order to investigate interfacial phenomena across dissimilar material interfaces, these multilayers were created by combining PLD, DC magnetron sputtering, and RF sputtering techniques.

The synthesized thin films and heterostructures have been systematically analysed using a variety of characterization techniques. Interfacial magnetization dynamics, a crucial component of spintronics that governs the effectiveness of magnetic damping and spin current transmission in multilayer systems, is given special attention in this study. The study intends to clarify the function of interfacial structure and spin mixing conductance through experimental investigations and thorough data analysis. These insights are expected to aid in the design and optimization of next-generation spintronic devices, such as spin valves, magnetic tunnel junctions, and spin Hall effect-based components, which hold promise for advanced information storage and processing technologies.

The results and findings have been methodically arranged into seven chapters in line with the overall goals of the study. The purpose of each chapter is to provide a thorough and comprehensive description of the experimental, theoretical research and analysis that was done. To give an overview of the thesis's organization and flow, a brief summary of each chapter's is provided below.

1.6 Thesis structure

This doctoral dissertation introduces new investigations on the development and fabrication of magnetic thin films, normal metal heterostructures and ultra-thin films of normal metal as well as the study of magnetic properties and spin dynamics features for applications in next-generation spintronics and high frequency microwaves. The growth, structural, and magnetic characterization of the yttrium-based yttrium iron garnet (YIG) epitaxial thin film, as well as the investigation of spin pumping by the measurement of produced emf across the film during FMR, are the primary focus of the first section. Second section focuses on the theoretical study on YIG thin film using HFSS to understand the reciprocal and non-reciprocal EM wave propagation in the range of microwave frequency. Fabrication of normal metal thin film on YIG as a bilayer and

multilayer heterostructure, and the investigation of spin pumping across ferromagnet-normal metal interface are the main focuses of the last section.

Chapter 2 Provides some context on the materials and experimental methods used in this dissertation. Every testing methodology is covered in detail. The characterization methods used to describe the various magnetic systems are demonstrated as well in this chapter.

Chapter 3 Introduces the YIG, effect of oxygen pressure on the deposition of YIG thin film. Both structural and magnetic characteristics of the epitaxial layer are described. magnetization dynamics analyses have been measured in relation to oxygen growth pressure. For possible application in spintronics-based devices, the FMR-induced emf across the YIG thin film has been measured and examined.

Chapter 4 Discusses theoretical as well as experimental investigation of the reciprocal and non-reciprocal EM wave propagation in the range of microwave frequency using thin film deposited under different oxygen growth pressure as an active element. HFSS simulation has been used to understand the reciprocal and non-reciprocal EM (Electromagnetic) wave propagation in the range of microwave frequency through different transmission line using YIG thin film as active element for its application in the field of microwave devices, a path towards the reduction of the size of microwave signal processing devices.

Chapter 5 Explains deposition of heterostructure of bilayer (YIG/Ta) and trilayer (YIG/Ta/Ni) on YIG. Demonstrated the controlled oxidation of Ni $\rightarrow$ NiO, deposited over YIG. Structural and magnetization studied performed of the multilayer nanometre thick film. To validate the spin pumping across the interface, magnetization dynamics measurements were performed on the heterostructures.

Chapter 6 Discusses deposition of nanometer thick NM (Noble/Normal Metal) over YIG. The multilayer thin film has been structurally characterized using XRD, RAMAN and AFM imaging. VSM mode of Physical properties measurement system used to characterise the magnetic properties of multilayer thin film deposited using the PLD and sputtering techniques. To validate the spin pumping across the FM/NM, FM/NM/NM and FM/NM/NM/NM interface, magnetization dynamics measurements were performed on the heterostructures.

Based on the findings and new approaches presented, the final **Chapter 7** summarizes the work presented in this dissertation, several suggestions for possible future research work and social impact of output of this research work.

Chapter 2

Experimental Method and Characterization Techniques

An outline of the fabrication, characterization, and experimental methods used in the current thesis work is given in this chapter. The fabrication of high-quality thin films and specific structures with minimal structural and compositional errors is essential for the effective application of nano-magnetic systems in the field of microwave and spintronics devices. Fundamentally, at the nanoscale, a material's intrinsic magnetic characteristics are heavily influenced by its surface quality, microstructure, and chemical order. Therefore, in order to analyze and optimize the corresponding magnetic properties, comprehensive characterization is also required. Polycrystalline bulk targets for pulsed laser deposition (PLD) were created using a solid-state reaction technique. In addition to pulsed laser deposition (PLD) process, DC and RF magnetron sputtering technique was used to deposit thin films. The structural characteristics of thin films were characterized using Raman spectroscopy and X-ray diffraction (XRD). Atomic force microscopy (AFM), scanning electron microscopy (SEM), and energy-dispersive X-ray spectroscopy (EDX) were used to analyze the thin films' morphology and elemental composition, respectively. A vibrating sample magnetometer (VSM)-equipped physical properties measurement (PPMS) equipment is used to analyze the films' magnetic characteristics. Additionally, we estimated the value of the damping parameter in our nm-thick deposited films by examining the magnetization dynamics of our films using Ferromagnetic Resonance (FMR) techniques. High frequency electromagnetic field simulations were carried out for theoretical investigations using ANSYS HFSS software.

2.1 Introduction

The synthesis, characterization, and analysis of thin films grown on a substrate are the main goals of this thesis. In order to gain a better understanding of the structural and magnetization dynamics of the yttrium iron garnet (YIG) materials, we used the pulsed laser deposition (PLD) technique to grow YIG on single crystalline $Gd_3Ga_5O_{12}$ (GGG) substrates with (111) orientations. The experimental approach and characterization technique used in the current investigation are summarized in this chapter. The primary objectives of the experimental portion are (a) creating the PLD target and its thin films, (b) characterizing its structural and magnetic properties, and (c) investigating FMR-based magnetization dynamics.

A generalized, systematic display of several experimental procedures, including synthesis and characterization methods, is provided in Fig. 2.1.

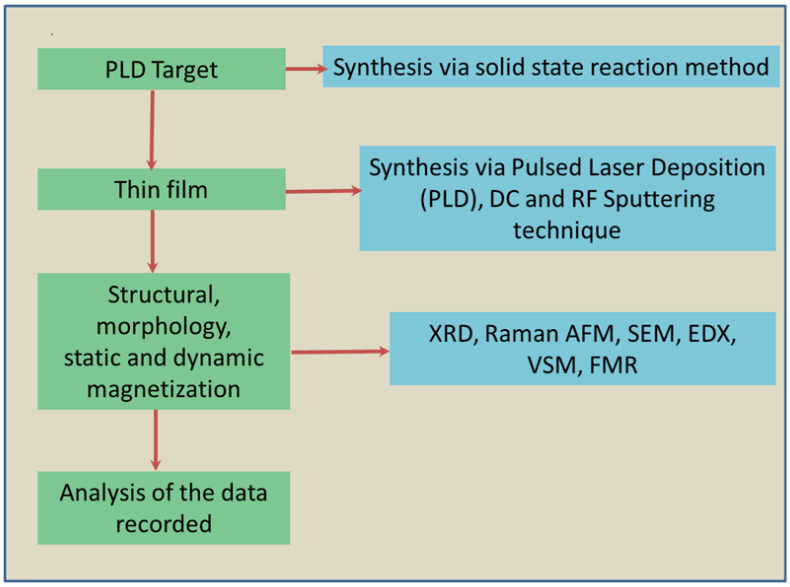

Fig. 2.1: A standard approach to systematic synthesis and characterization.

In the current investigation, a PLD procedure was used to deposit the thin films of the polycrystalline PLD targets of YIG, which were synthesized utilizing a solid-state reaction approach. On top of YIG thin films, noble/normal metallic thin films including Ta, Ni, Pt, Cu, and W have been deposited using the DC and RF sputtering techniques. Atomic force microscopy (AFM) and laser lithography techniques have been used to determine the thickness of the thin films that have been grown. The structural features of as-grown thin films are determined using Raman spectroscopy and X-ray diffraction methods. AFM, SEM, and EDX were used to examine the thin films' surface topography/morpholgy and elemental composition, respectively. Static magnetization has been evaluated using the Physical Properties Measurement System (PPMS), and FMR readings have been quantified using the Vector Network Analyzer (VNA).

2.2 Synthesis of samples

A crucial step in creating high-quality components for magnetic and spintronic devices is the synthesis of thin films. Because thin films have less dimensionality, interface effects, and strain than their bulk equivalents, they provide regulated structural, magnetic, and electrical properties. To provide the necessary crystallinity, thickness uniformity, interface sharpness, and compositional purity, sample synthesis necessitates exact control over the deposition settings.

2.2.1 Synthesis of PLD targets using solid state reaction method

Since stoichiometry, phase purity, and target density directly affect the structural and functional properties of the deposited films, excellent target preparation is essential when using pulsed laser deposition (PLD) for thin film deposition. The solid-state reaction process is a popular method for creating targets due to its ease of use, affordability, and uniformity of the final composition with regulated crystallinity [132]. The solid-state reaction technique is more frequently used to prepare polycrystalline samples [133]. This method involves the high-temperature, solvent-free reaction of solid-phase constituent

materials. This method yields a final polycrystalline product or a structurally pure powder with no waste. A ball mill or mortar and pestle is used to thoroughly combine the powders, resulting in a fine and evenly distributed powder that increases reactivity. Pellets are made by pressing the mixed material into a die using a hydraulic press that has a pressure range of 3 to 5 tons. To create the final product, these pellets are subsequently sintered in a high-temperature furnace for a few hours. The milling medium, milling time, milling speed, and the precursors utilized are some of those factors that affect the growth of the synthesized sample. Most precursors used are oxide-based compounds, which typically require very high temperatures (>1100 ^{O}C) in a tube furnace to complete the manufacturing process and produce the desired material. The solid-state reaction technique was used in the present dissertation to synthesize yttrium iron garnet (YIG) targets.

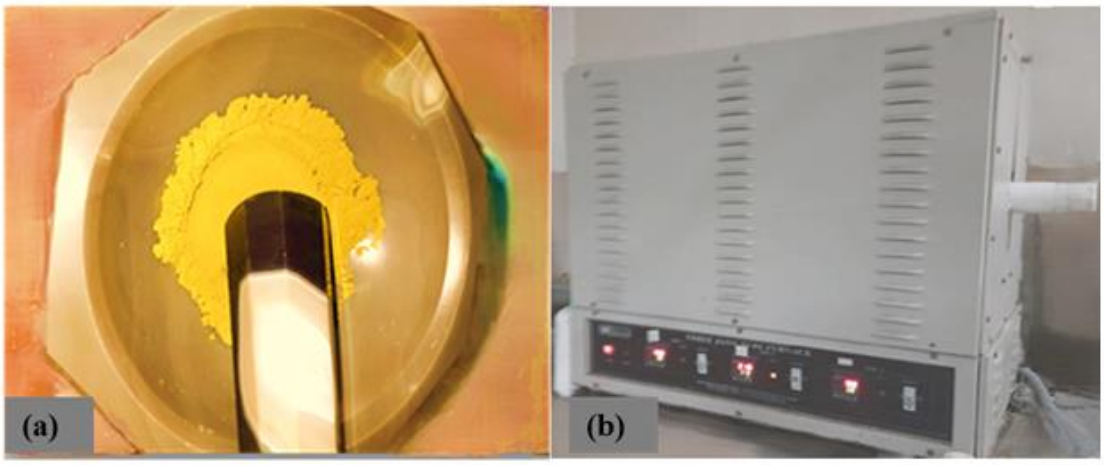

Fig.-2.2 (a) A mortar and pestle with a powered sample inside (b) high-temperature tube furnace (≈1400 ^{O}C).

Yttrium oxide (Y_2O_3) and iron oxide (Fe_2O_3) powders were milled for 14 hours prior to being calcined at 1100 ^{O}C. Following a calcination operation at 1200 ^{O}C, the grounded mixture is displayed in fig. 2.2 (a). To create a 1-inch PLD target, the calcined powders

were molded into 1-inch pellets and sintered at 1300 ^{O}C. Our lab's three zone tube furnace, which we used to calcinate and sinter PLD targets, is seen in fig. 2.2(b). It promotes chemical interaction and solid-state diffusion. Molded 1- inch pellets are very much useful for the deposition of yttrium iron garnet (YIG) using pulsed laser deposition (PLD) system, it can also be used for sputtering technique.

2.2.2 Physical vapor deposition (PVD) technique

One of the most widely used thin-film deposition techniques for creating high-purity, tightly-bonded, and controlled coatings on substrates is physical vapor deposition, or PVD. In PVD, the source material is physically transformed into vapor within a vacuum chamber, and when it condenses, it is deposited as a thin layer on a substrate. Due to its ability to deposit films with precise thickness and homogeneity, PVD finds extensive application in microelectronics, spintronics, optics, and protective layers [132].

Table 2.1: Thin film deposition method based on PVD

Method of deposition	**A quick description**
Electron beam evaporation	Bombardment with electrons in a high vacuum
Thermal evaporation	Electrically resistive heating at high vacuum
Sputtering	bombarded with plasma discharge under a high vacuum
Molecular beam epitaxy	Ultra-high vacuum electron beam evaporation to produce a highly epitaxial film
Pulsed laser deposition	In a high vacuum chamber, laser ablation

Nowadays, thin films have been explored for a variety of applications and are continuously being developed to create a broad spectrum of them [134,135]. The properties and quality of thin films are significantly influenced by the deposition process. Two of the most used methods for depositing thin films are PVD and CVD. Whereas CVD employs chemical reactions at the layered surfaces, PVD only uses physical processes, including high-temperature vacuum evaporation or plasma sputtering a target material. Table 2.1 lists thin film deposition method based on PVD.

There are three fundamental steps in the PVD process: The source material is vaporized via laser ablation, sputtering, or heating. To minimize contamination, the vapor species are transported from the target to the substrate in a low-pressure vacuum chamber. On the substrate's surface, condensation and film growth provide thin-film creation with regulated microstructure and characteristics [136].

2.2.2.1 Electron beam evaporation

One of the PVD method for creating thin films with excellent adhesion, precise thickness control, and high purity is electron beam evaporation (EBE). In applications including microelectronics, optics, and spintronics, it is particularly well-suited for evaporating metals, oxides, and semiconductors. To achieve better deposition rates and make it easier to evaporate substances with exceptionally high melting points, EBE uses a narrow, high-energy electron beam to melt and evaporate the target material inside a vacuum chamber, as opposed to typical thermal evaporation [132]. In EBE, an electric field is applied to accelerate an electron beam created by heating a tungsten filament. Within a water-cooled copper crucible, the beam is focused on the target, which is often a solid ingot or pellet. When the electrons collide, their kinetic energy is transformed into heat, which causes the target material to heat up locally and evaporate. In the vacuum chamber, the evaporated atoms travel and form a thin layer that condenses on the substrate. The stoichiometric transfer of source material to the film is made possible by the high vacuum conditions

(10^{-6}–10^{-7} Torr), which also reduce contamination and give vapor atoms a lengthy mean free route [137]. It has several advantages some of these are, the capacity to evaporate materials with a high melting point, such as W, Ta, and NiO, high deposition rate and good homogeneity, high-purity films as a result of the perfect vacuum environment and support for in situ monitoring systems (such as a quartz crystal microbalance for controlling thickness).

Electron beam evaporation is widely used in semiconductor devices, protective coatings, optical coatings (antireflection layers, mirrors), and spintronic materials. It enables the deposition of sharp-interface ferromagnetic and oxide layers in spintronics, which are essential for studying spin transport processes and interfacial spin dynamics.

2.2.2.2 Thermal evaporation

One of the simplest and most used physical vapor deposition (PVD) techniques for creating thin films is thermal evaporation. This method involves heating the source material in a vacuum chamber to cause it to evaporate. The atoms that have evaporated then condense on a substrate to form a thin layer. Thermal evaporation is an essential technique in material science, microelectronics, optics, and spintronics because of its affordability, ease of use, and capacity to evaporate a wide range of metals and compounds [132, 137].

High vacuum conditions (10^{-5}–10^{-7} Torr) are used during the process to reduce contamination and improve the mean free path of evaporated atoms. A resistively heated boat, filament, or crucible—typically made of refractory metals like tungsten or molybdenum is used to hold the source material, which can be either metal or oxide. A phase transition transforms the material from a solid to a vapor when sufficient energy is applied. As the vapor's atoms approach the substrate in line of sight, they nucleate and form a thin layer. The most used filament basket material is tungsten due to its chemical inertness, ease of formation, and resistance to temperatures of up to 3000° C. The source

material and the samples are typically more than 20 cm apart in resistive thermal evaporators.

The growth process can be controlled in real time with a quartz crystal microbalance (QCM), which is typically used to manage the film thickness and deposition rate. It has several advantages few of them are inexpensive and easy method, versatile in accurately controlling thickness and uniformly depositing thin coatings, high rates of deposition in contrast to chemical or sputtering techniques and applicable to dielectric films, metals, and certain semiconductors. With the advantage it has limitation as well like, the difficulty of evaporating minerals with extremely high melting points (such as W and Ta) and line-of-sight deposition results in ineffective step coverage on complex geometry. In comparison to sputtered films, films may show decreased density and stickiness.

Thermal evaporation has been widely used in spintronics for the deposition of metallic thin films and multilayers, optics for reflective and antireflection coatings, and microelectronics for metallization. Tunnel junctions, ferromagnetic/non-magnetic heterostructures, and other structures whose thickness and purity must be regulated are particularly prepared by thermal evaporation.

2.2.2.3 Growth of thin films via pulsed-laser deposition technique

This section discusses the use of the pulsed laser deposition (PLD) technique to fabricate thin films with high performance for research and development purposes, impact of deposition parameters on thin-film properties are also covered. In this work, magnetization dynamics on PLD-produced YIG thin films were investigated. In terms of both concept and performance, PLD is the most inventive and simple of the thin film deposition techniques listed in table 2.1. A simplified design of a PLD setup is displayed in fig. 2.3. Target and substrate holders are placed inside a vacuum chamber within the scope of the setup. This is a high vacuum chamber driven by a strong Turbo molecular

pump, which can cause the vacuum to drop as low as 10^{-8} Torr. PLD can be thought of as a three-step thin film development process that consists of the subsequent steps:

1. Target material is illuminated by a high-power excimer (KrF) pulsed laser beam.

2. The target material is struck by laser energy, which causes it to vaporize and create a laser plume.
3. The plume consists of a variety of energetic species, including "ions, atoms, and molecules," which rapidly expand from the surface of the target to the vacuum, creating a nozzle jet that is subsequently deposited on the substrate.

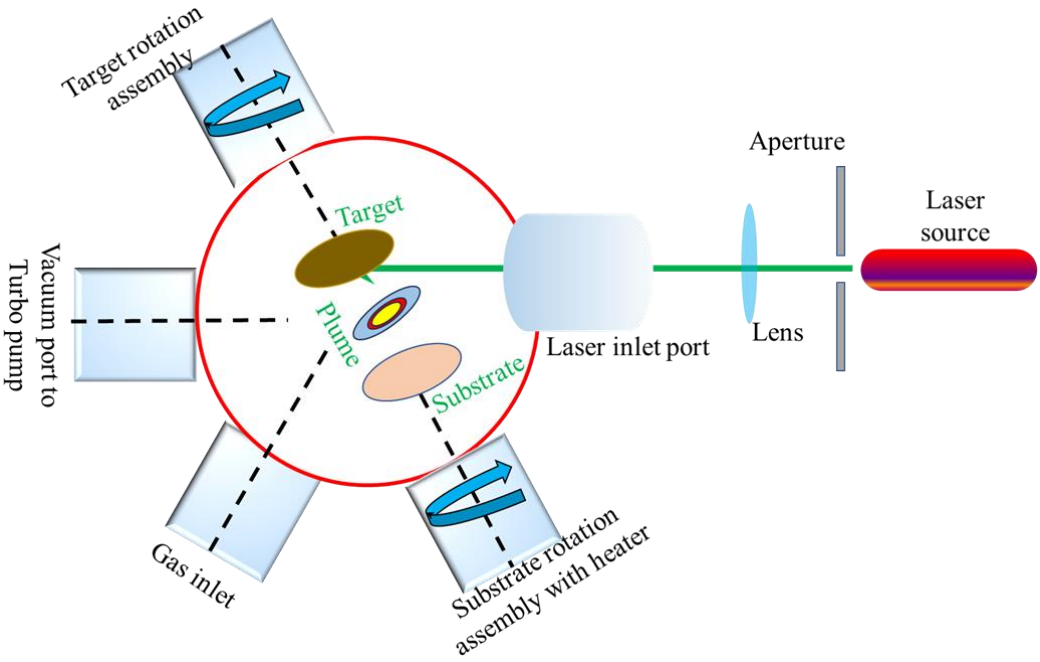

Fig.: 2.3 A diagram of a PLD configuration.

Fig. 2.4 depicts the PLD system that is in place at our lab Special Centre for Nanoscience (JNU). This system uses a KrF excimer laser from COHERENT with a maximum energy of 750 mJ and a pulse width of 25 ns. The deposition is highly forward and directed, and

it is perpendicular to the surface of the target. Using an optical train made up of mirrors, apertures, and lenses, the laser beam is focussed and moved across the target surface. Thin films can be grown in reactive and inert atmospheres using fluid gases, including argon, nitrogen, and oxygen [138-140]. To maintain film uniformity, substrates and targets are rotated around during the deposition process.

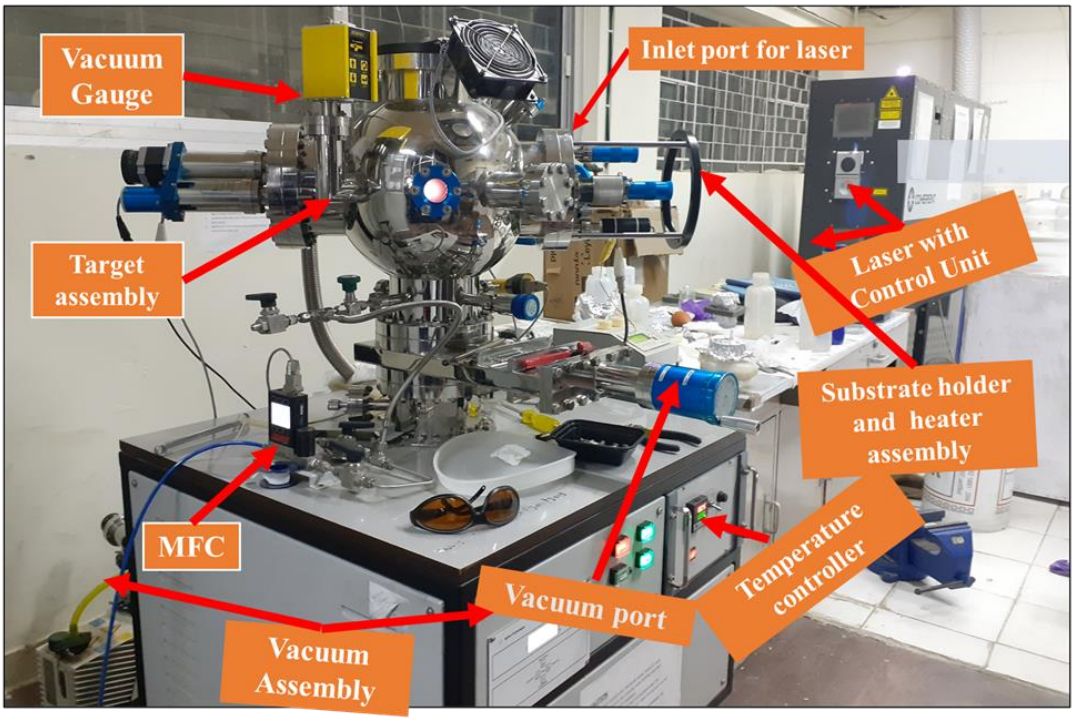

Fig.:2.4 The actual PLD equipment used for ferromagnetic thin-film deposition in the laboratory.

A carousel of targets can be used to load or choose many targets at the same time, enabling the deposition of multilayer structures and films with different compositions at different substrate temperatures in this system. The advantage of PLD over other methods is that it can produce thin films with a standard composition that is the same as the Target structure. In many applications, the production and existence of finely formed PLD device has been

an issue since the technology's adoption. Even while PLD works best for films with precise average stoichiometry, a variety of deposition parameters can be adjusted and finished to produce individual phase films as well as specific nanostructures and shapes in thin films. In our system, films can be deposited at the maximum temperature of 850 °C. In this thesis, the PLD technique was used to generate YIG thin films of the necessary thickness in-situ on (111) oriented GGG substrates.

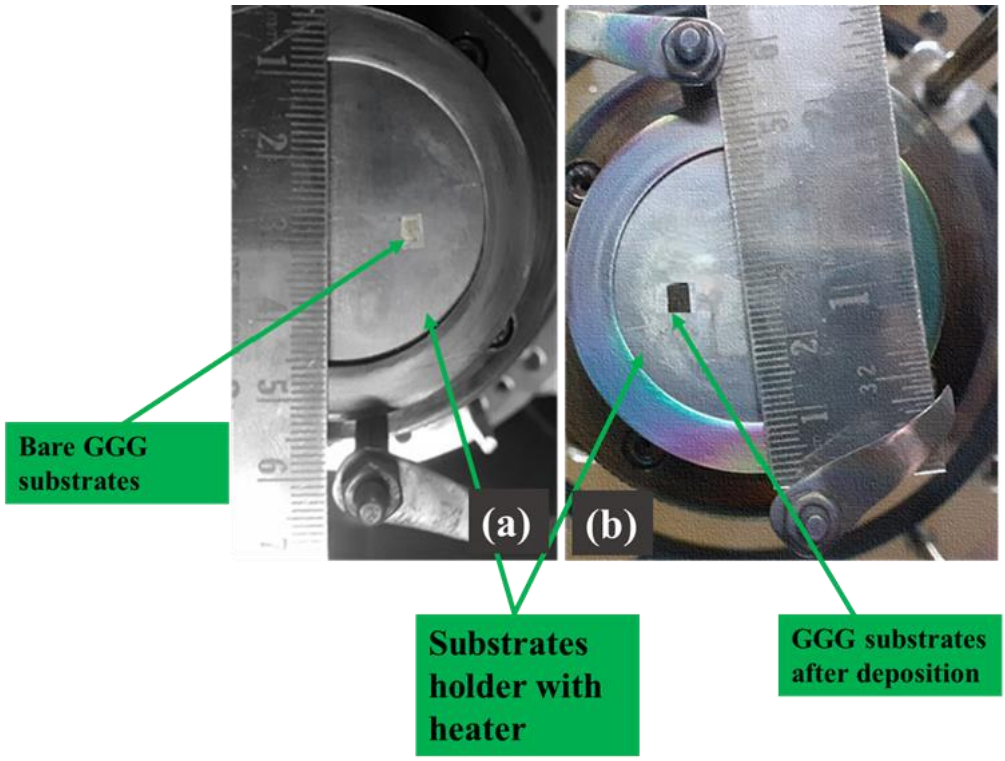

Fig.: 2.5 PLD substrate holder with heater

Fig. 2.5 (a) and (b) depicts the PLD substrate holder attached with the heater before and after the deposition respectively.

Before the deposition procedure started, the GGG substrates and the deposition chamber were first thoroughly cleaned and evacuated to a base vacuum of 2×10^{-6} mbar. We used a KrF excimer laser (248 nm) to ablate the targets at 300 mJ of energy with a pulse

frequency of 10 Hz. Oxygen pressure, substrate temperature, substrate distance from the target and all other parameters of PLD setup like frequency, energy was optimized for the deposition of nanometer thick YIG film. This technique has few limitations like; plume geometry limits the scalability of large-area substrates, the smoothness of the film may be reduced by particulate formation (droplets) and it involves precisely regulating the substrate's conditions and the laser's settings. Over the restriction it has several advantages in thin film deposition process like complicated target compositions deposited stoichiometrically into thin sheets, flexibility in depositing multilayers, nitrides, and oxides, the ability to create epitaxial thin films with interfaces that are atomically abrupt and moving between different targets for multilayer deposition rather quickly. PLD has been widely utilized to generate heavy metal heterostructures (Pt, W, Ta) and Yttrium Iron Garnet (YIG) thin films, which are essential for studying interfacial spin dynamics, spin pumping, and the spin Hall effect. Additionally, PLD is widely used in the formation of ferroelectrics, multiferroics, and high-temperature superconductors, where stoichiometry retention is crucial [141]

2.2.2.4 Growth of thin films via DC and RF sputtering technique

One popular physical vapor deposition (PVD) technique for thin-film generation is sputtering, which is particularly useful for creating optical thin films, magnetic heterostructures, and microelectronic devices. High-energy ions created in a plasma are impacted on a solid target during sputtering, causing atoms to spatter from its surface. To form a thin film, these atoms go through the vacuum chamber and settle on a substrate [136]. The sputtering technology is advantageous for usage in the semiconductor, optical, magnetic storage, and other sectors due to the comparatively high homogeneity of the sputtered thin films. For research and development purposes, this section addresses the use of DC and RF sputtering technique to create high-performance thin films. It also covers the effects of deposition parameters on the properties of thin films. The magnetization dynamics on sputtering grown noble/normal metals (Pt, W, Cu, Ni,) on PLD

grown YIG were examined in this work. In a basic sputtering operation, a target material gets bombarded with extremely energetic ions produced by the glow discharge plasma that is situated in close proximity to the target. This method falls under the plasma deposition category. This procedure involves electrically ionizing sputtering gas to create a plasma, then ejecting material from the target to the substrate and removing the target material via ion bombardment. The actual sputtering is often carried out in a high-vacuum chamber with an inert gas, such as argon. An electric field ionizes the argon gas to create a plasma when a voltage is supplied between the cathode (target) and anode. Surface atoms are atomically ejected from the target due to momentum transfer caused by positively charged Ar^+ ions being propelled in the direction of the negatively biased target. A thin layer is formed on the substrate by the atoms that are sputtered, which move across the chamber [132].

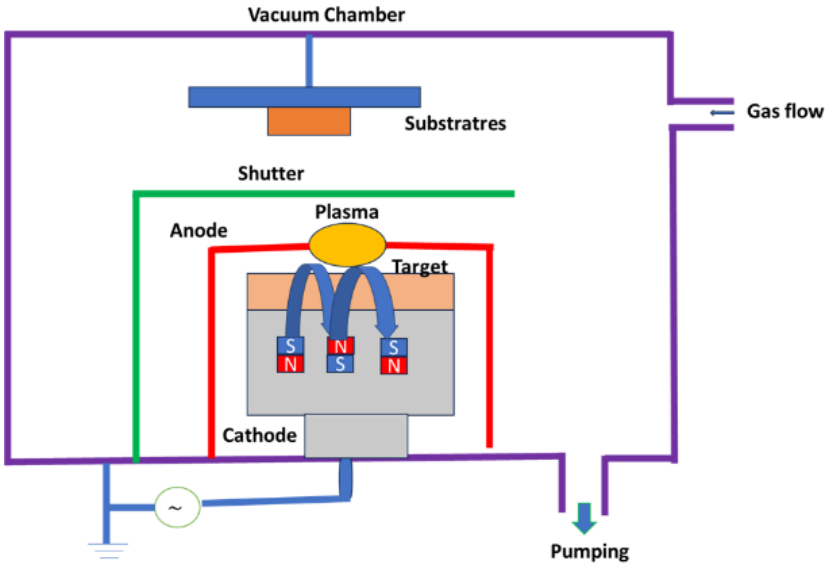

Fig.: 2.6 Sputtering system schematic diagram.

Sputtering's primary benefits include: (a) a high rate of deposition for DC sputtering. (b) Consistency of film throughout wide regions. (c) Control of surface thickness and smoothness. (d) Since it relies on momentum transfer rather than thermal or chemical

reactions, it is a versatile method that can sputter any type of material. An external high voltage power source powers two electrodes in a vacuum inside the sputtering deposition chamber. The substrates are positioned on the earthed sample wheel, and the material to be deposited is referred to as the target and serves as the cathode.

In fig. 2.6, a sputtering system schematic diagram is displayed. Argon or nitrogen, an inert gas, is refilled into the growth chamber during the sputtering process. An electric discharge is produced when a voltage is introduced between the cathode and anode. The gas becomes partially ionized as a result, and when these ions hit the target with enough energy, surface atoms are ejected from the target and settle onto the substrate. This causes the gas to become even more ionized as the voltage accelerates the ionized gas and the liberated electrons, which then continue to collide. At last, the plasma stabilizes and a breakdown condition is obtained. Secondary electron emission is the main supply of electrons needed to keep the plasma flowing. The ratio of incident ions hitting the target to the mean number of ejected atoms from the surface is known as the sputter yield, and it provides a measure of ejected surface atoms. The following variables affect the sputter yield: (a) incident particle energy; (b) target atom and ion atomic weights; (c) incident particle angles; and (d) target surface crystal structure. Between 10 and 100 keV is the high-energy region where the sputter yield reaches its greatest value. Between 60^{O} and 80^{O} incidence angles, the highest yield is seen. Depending on the substance to be deposited, sputtering techniques can be divided into two categories: DC and RF. While RF sputtering is used to produce thin insulator coatings, DC sputtering is utilized to deposit metal. A DC voltage of about 400 V is used in DC sputtering to produce plasma between the electrodes. A voltage that oscillates at radio frequency (RF), usually 13.56 MHz, is delivered in RF sputtering to bias the electrode and maintain the glow discharge. The alternating current will stop a surface charge of positive ions from accumulating on the insulator's front side. Ion bombardment of the target to be sputtered proceeds on the negative cycle, while electron attraction to the cathode creates a negative bias on the

positive cycle. The ejected atoms are deposited on the substrate after being sputtered. Permanent magnets are positioned underneath the target for magnetron sputtering in order to use the Lorentz force to confine the plasma. The major types of sputtering are explained below:

DC Sputtering

In direct current sputtering, a high-voltage direct current (DC) power source creates a glow discharge between a target or source material and a substrate in a low-pressure inert gas atmosphere (usually argon is employed). Fig. 2.7 demonstrates the schematic representation of DC sputtering. In the vacuum chamber opposite the substrate is the target, or material to be deposited. The chamber is provided with a low-pressure argon gas atmosphere to facilitate the sputtering process. A high voltage applied to the target material ionizes the argon gas, resulting in a plasma or glow discharge.

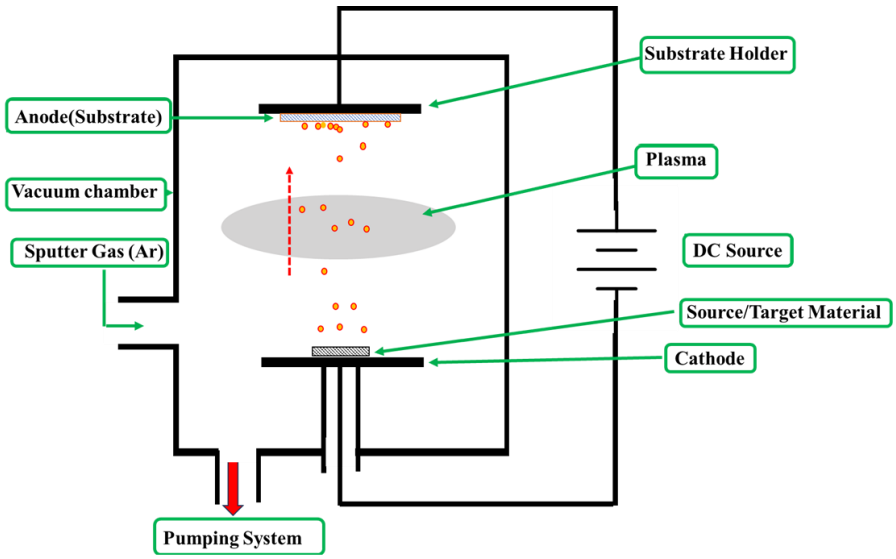

Fig: 2.7 Schematic representation of DC sputtering

Positively charged argon ions are pulled toward the target material. When accelerated argon ions strike a target material, they push atoms or molecules away from the target

surface, a process known as sputtering. The sputtered atoms or molecules create a thin layer that is similar to the target material in properties after passing through the vacuum chamber and settling on the substrate surface. It has limitation like; only conductive targets can be used because it is ineffective at sputtering non-conductive materials and one of the most important limitations it may cause considerable substrate heating, making it unsuitable for substrates that are sensitive to temperature changes. But even with limitation it has few advantages also, compared to RF sputtering systems, DC sputtering equipment is more affordable and simpler and one important advantage is higher deposition rates are typically attained, which makes it appropriate for applications needing high throughput or thick films.

RF Sputtering

Ion current density can be increased and problems related to charging insulating cathodes can be resolved by using radiofrequency power instead of a DC voltage at the cathode. While 13.56 MHz is the most commonly used frequency for RF, other frequencies between 60 Hz and 100 MHz have also been used.

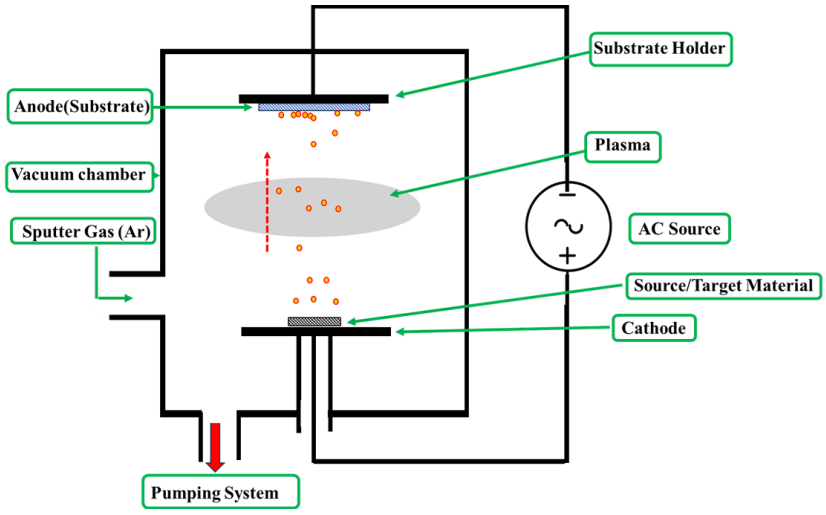

Fig: 2.8 Schematic representation of RF sputtering.

A plasma that oscillates mostly at the same frequency is produced by the RF voltage applied to the cathode, which is typically in the range of several kV. Fig. 2.8 depicts the schematic representation of RF sputtering. The electron will move quickly toward the cathode and neutralize the majority of the atoms or molecules from the source/target material, whereas the Ar+ ions will move slowly toward the anode during the first half of the cycle. The Ar+ atoms will travel quickly toward the target and eject the atoms at a high speed when the cycle changes, that is, in the second half of the cycle. Every atom that is expelled will travel in the direction of the substrate, where it will condense into a thin layer. Disadvantage of RF sputtering is, compared to DC sputtering systems, the equipment is more costly and sophisticated, requiring RF power sources and associated networks, requires RF generation and matching, which increase power consumption and could increase operating expenses. It has several advantages also like; both conductive and non-conductive materials can be sputtered, demonstrating adaptability for a wide range of applications and produces films of superior quality that are dense, adhesive, and have good control over thickness and homogeneity.

Magnetron Sputtering

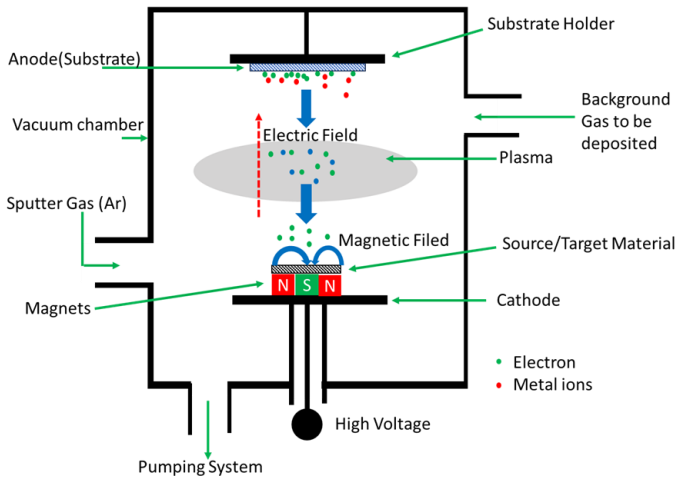

Fig: 2.9 Schematic illustration of magnetron sputtering

Magnetron sputtering employs a magnetic field behind the cathode plate in addition to an applied electric field, unlike ordinary sputtering, which simply uses an applied electric field. Charge carrier mobility is effectively limited by the electric and magnetic fields working together. Originally aligned with the electric field lines, they now orbit the target surface in a spiral trajectory, specifically cycloid orbits. This increases the number of collisions per electron and extends their trajectory. When the magnetic field is parallel to the target surface, the electron density is at its highest. This leads to an increase in ionization. Sputtering is highest on the target because the ions are quite heavy and are not greatly deflected by the magnetic field. There is sputtering on the target. Fig. 2.9 depicts the schematic illustration of magnetron sputtering.

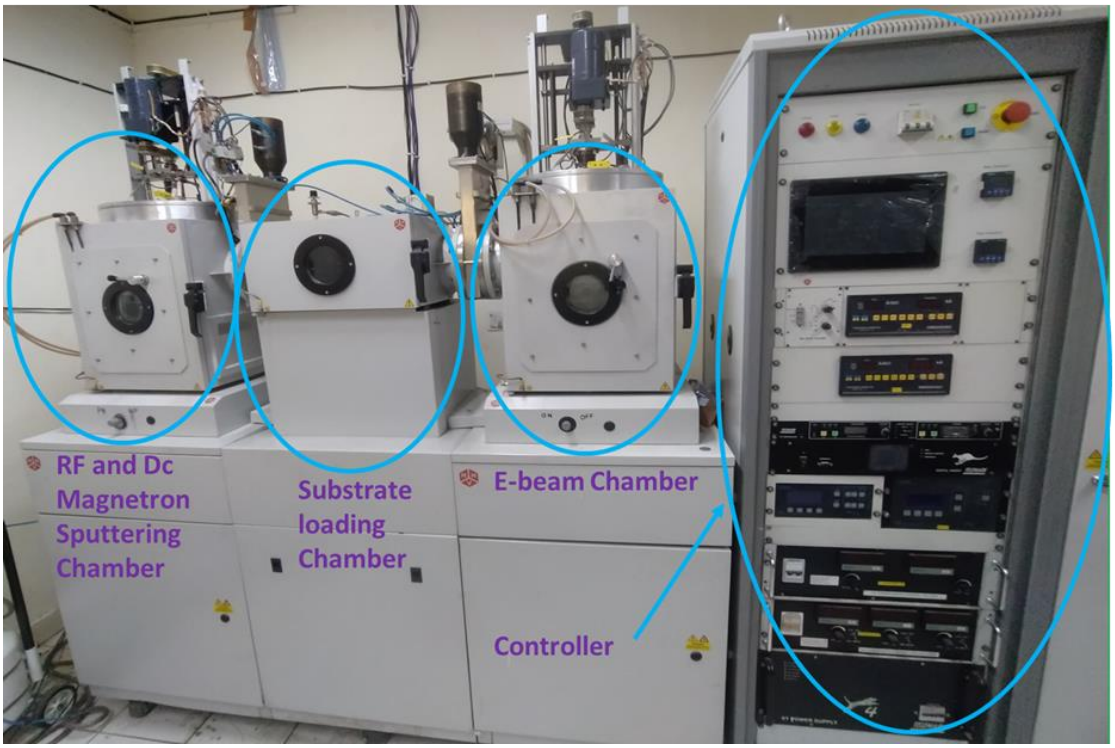

Fig.: 2.10 HHV-made Dual Beam (RF/DC magnetron sputtering) system

As illustrated in Fig. 2.10, this dissertation utilizes the HHV-made Dual Beam System (Sputtering and E-beam) for RF/DC Magnetron Sputtering. We have used sputtering

system for the deposition of heterostructure on PLD deposited YIG. This system used for the deposition of noble/normal metal for magnetization dynamics study.

Because magnetic fields and elaborate power sources are used, the equipment is more complicated and costly than in basic DC or RF sputtering systems. Effective sputtering of magnetic materials and specific geometries can be difficult because of the magnetic field's influence. With this limitation it is very much useful in thin film research, due to its increased plasma density, magnetron sputtering achieves better deposition rates than conventional sputtering techniques, it is appropriate for thin-film applications and substrates that are sensitive to temperature because it reduces substrate heating.

Reactive sputtering is also one of the technique comes under the sputtering process, this process deposits compound like oxides or nitrides by introducing a reactive gas (such as O_2 or N_2) into the chamber.All the above explanation may be summarised as, for conductive targets, DC sputtering is perfect, Oxides and other insulating targets are used with RF sputtering and Magnetic fields around the target are used in magnetron sputtering to confine electrons, increase plasma density, and accelerate deposition rates.

2.2.3 Chemical Vapor Deposition (CVD)

In contrast to PVD, which requires solid precursors, chemical vapor deposition applies solid materials straight from a gas state—usually diluted in carrier gases—to a substrate by vaporizing the material to be deposited straight from a solid target. It belongs to the category of vapor-transfer processes and is an atomistic process. Fig. 2.11 shows the schematic representation of chemical vapor deposition (CVD) system. In chemical vapor deposition (CVD), gaseous precursors react chemically at a heated substrate to form a thick deposit. Solid materials with excellent performance and purity are produced via a chemical process known as CVD. This technique is suitable for creating coatings, powders, fibers, and monolithic components and is commonly utilized in thin film

applications. By altering the experimental parameters, materials with a variety of properties can be generated.

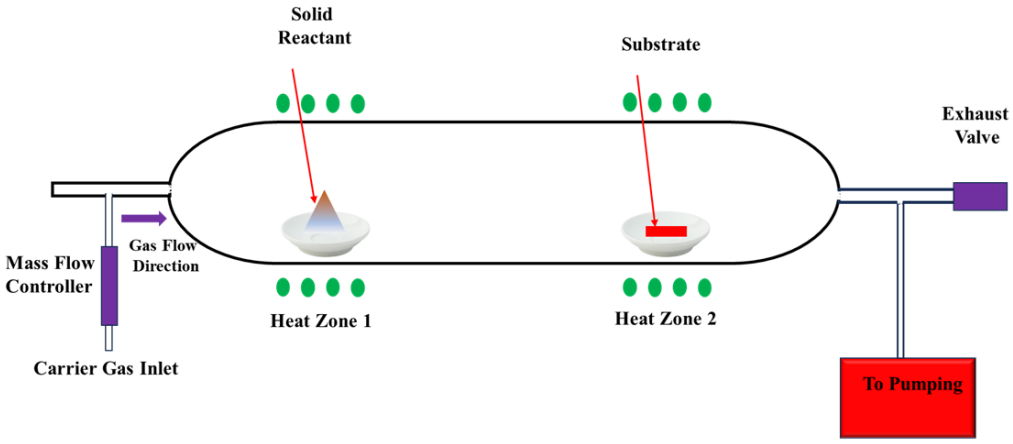

Fig.: 2.11 Schematic representation of chemical vapor Deposition (CVD) system

2.2.4 Thin film thickness measurement

Bi-YIG and normal metal (NM) thin film thickness was measured in this study using techniques like laser lithography and AFM. We used PLD laser shots to calibrate the thin film thickness. A silicon substrate is covered with photoresist via spin coating, then laser photolithography is used to create straight line patterns on the photoresist-coated substrates. Using a pattern-drawn substrate, thin films of the necessary material were deposited using the PLD process. To get rid of the photoresist covering, the PLD-grown thin film must subsequently be wet etched. The thickness of the grown samples is then estimated from the AFM profile image by scanning the AFM tip across the line pattern region. With the following PLD parameters, the AFM profile image of the Bi-YIG thin film generated by the PLD process is shown in Fig. 2.12: 3000 laser beams with 300 mJ of energy and a frequency of 10 Hz. In fig. 2.12 image (a) shows the bright field image of pattern generated using the lithography technique, fig. 2.12 (b) the acquired AFM image of pattern and fig. 2.12 (c) shows the height profile of AFM image to determine the height

of deposited film. Bi-YIG thin films have an estimated thickness of 20 nm for 3000 shots, and the thickness of Pt and Cu, W, Ni thin films has been calibrated using a similar method.

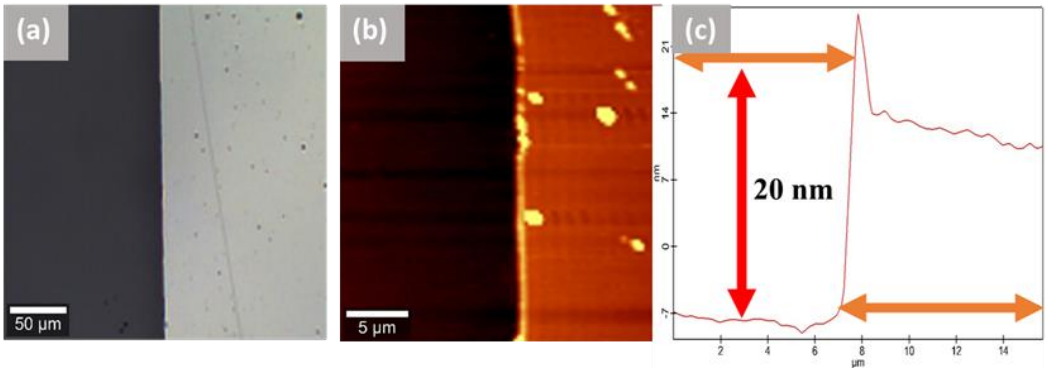

Fig.: 2.12 (a) Bright field image of pattern (b) AFM image of pattern (c) Height Profile of AFM

2.3 Characterization

Thin film characterization is a crucial procedure in many scientific and industrial domains since it ensures the expected characteristics and functionality of materials and device. In spintronics and materials science research, characterization techniques are crucial tools because they provide details on the morphological, electrical, magnetic, and structural characteristics of thin films and heterostructures. Establishing a connection between the growing process and the final physical characteristics of the films requires a systematic knowledge of these characteristics. Understanding the physical characteristics and possible uses of the film is aided by analyzing the crystal structure. To know the structural properties and chemical composition of grown film is very important to understand the required application of the film. Finding distinct phases inside the thin film shows how these phases affect the performance and characteristics of the material. Application of thin film in the field of spintronics could be understand using the magnetization dynamics study of the grown film. Measurement of thickness is essential because it influences the mechanical, optical, and electrical characteristics of the film, which in turn impacts how

well it works in its intended purpose. Roughness and surface characteristics aid in forecasting how the film will interact with its surroundings, influencing characteristics like reflectance and adhesiveness. Surface morphology and the elemental composition of film is vital parameter for the prominent application of the thin film. For electronic applications where conductivity, resistivity, and dielectric constant affect device performance, measuring these characteristics is essential. Understanding the behavior and performance of materials is aided by describing flaws, grain size, and grain boundaries. Maintaining uniformity across the film is essential for reliable performance in applications like displays and large-area coatings. Reliability is ensured by knowing how the film's characteristics alter in different environmental settings. Therefore, characterization is essential tools to the fabrication of devices and its potential application in the field of spintronics and material science research. In the current work, various characterization techniques were employed to evaluate the surface morphology, magnetic characteristics, crystallinity, and quality of thin films and multilayers.

2.3.1 Structural Characterization

Structural characterization methods are critical in determining the crystallographic perfection, purity of phases, and epitaxial growth of thin films and multilayer heterostructures. Structural properties like lattice parameter, strain, grain size, crystallographic orientation, and interface sharpness are important in magnetic thin films as they largely influence the magnetic and spin transport properties. Among the several techniques, X-ray diffraction (XRD) is a very common method used, as it gives accurate information regarding crystal structure, orientation, and epitaxial relations between the film and substrate [142]. X-ray reflectivity (XRR) is also generally used to calculate film thickness, interface roughness, and density, which are important parameters in spintronics where interfacial effects play a pivotal role.

2.3.1.1 X-ray diffraction (XRD)

The material's crystal structure can be determined using the X-ray diffraction technique. It is a non-invasive method of understanding out the crystalline structure and growth direction of a material. The basis of this method is the coherent interference of scattered waves from areas with a high electron density. The foundation of it is Bragg's law [143,144], which addresses the interference of X-rays continually dispersed by crystals. According to Bragg's law, constructive interference must meet certain requirements.

$$\eta\lambda = 2d\sin\theta \tag{2.1}$$

Where, η is the order of reflection, λ is the X-ray wavelength, and d is the interplanar spacing, as shown in Fig 2.13.

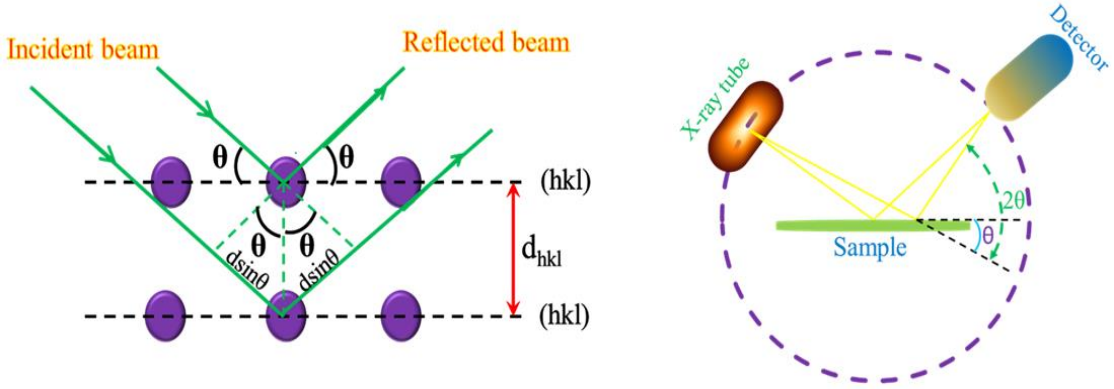

Fig.:2.13 (a) X-ray diffraction from atomic planes in a crystal and (b) Schematic of XRD

Atoms within crystals are arranged in a regular pattern. There will be various diffracted X-ray beams leaving the sample in distinct directions, and when an X-ray beam incident on the crystal plane, there will be constructive interference in that particular direction [145-147]. Therefore, a diffracted beam is a group of many scattered rays from the crystal that are reinforcing each other equally. Basic geometry provides the $n\lambda$=$2dsin\theta$ condition, as seen in Fig. 2.13 schematic representation.

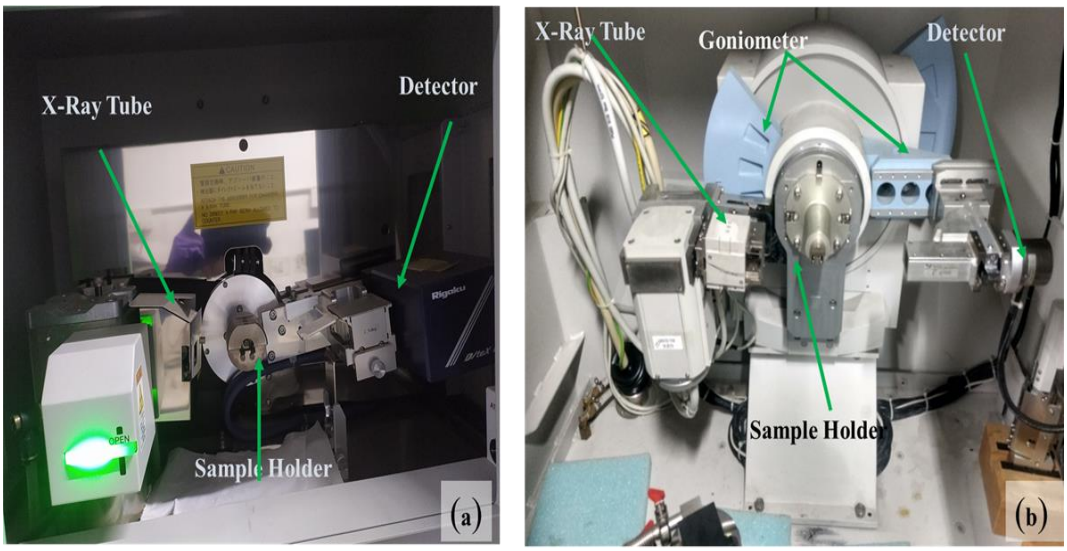

Fig. 2.14 (a) Powder XRD From Rigaku, Miniflex 600 equipment and (b) X'Pert PRO from PANalytical with a lower gazing angle of incidence.

XRD machine from Rigaku Miniflex 600 shown in fig. 2.14 (a), which uses $Cu - K_\alpha$ radiation with a wavelength of 1.5405 Å, and X'Pert PRO from PANalytical diffractometer shown in fig. 2.14 (b), which is equipped with a $Cu - K_\alpha$ unit of wavelength 1.54 Å and a lower gazing angle of incidence of 1^0, used to perform the full XRD characterization of magnetic thin film as well as heterostructures.

2.3.1.2 Raman spectroscopy

A sensitive nondestructive optical characterization technique that provides information about a material's rotational, vibrational, and other low-frequency modes is Raman spectroscopy. It is based on the inelastic scattering of monochromatic light, usually from a laser, in which the incident photons encounter material phonons, causing the scattered radiation to change in energy [148]. Absorption, reflection, or scattering are the three ways that monochromatic light interacts with the "lattice phonons" when it directly hits the sample [149]. The Raman measurement is determined by analyzing scattered radiation. It is possible to distinguish between the inelastic and elastic components of scattered radiation [150]. Rayleigh scattering scatters light without altering its frequency since it is

an elastic mechanism. Conversely, Raman scattering is described as a change in the frequency of light. Depending on the molecules' vibrational state, the frequency of this scattered light may be higher or lower. Electron-hole pairs are created through electron radiation interaction when an incoming photon with wave vector k_i and frequency ω_i interacts with the lattice. These electrons recombine with the hole due to electron-lattice interaction, creating a phonon (wave vector k_i and frequency ω_i). The conservation law can be used to express the wave vector and scattered photon frequency. When $\omega_s < \omega_i$, there is Stokes scattering; when $\omega_s > \omega_i$, there is anti-stokes scattering. A change in frequency known as the Raman shift provides details on structural and chemical alterations in the material, including bond vibration and serves as the material's fingerprint. For the analysis of the magnetoelectric coupling caused by structural distortion in multiferroic materials, this bond vibrational energy is crucial. Fig. 2.15 depicts the schematic of traditional RAMAN spectroscopy.

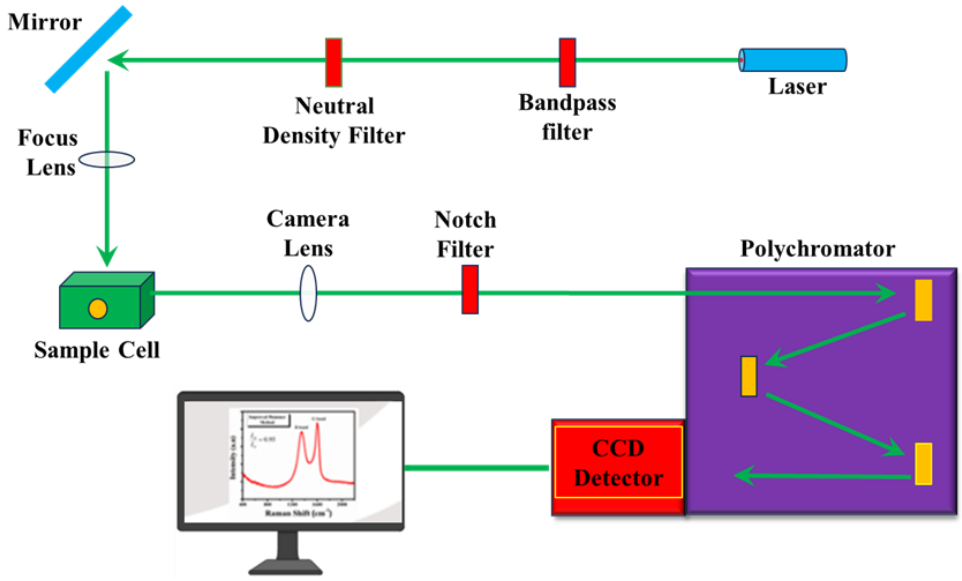

Fig.: 2.15 Schematic representation of Raman spectroscopy

A radiation source, optics (such as mirrors and lenses for focusing light on the sample and catching dispersed light), a spectrometer, and a detector are the four main parts of the

Raman system. Usually, a monochromatic laser producing ultraviolet, visible, or near-infrared light serves as the light source.

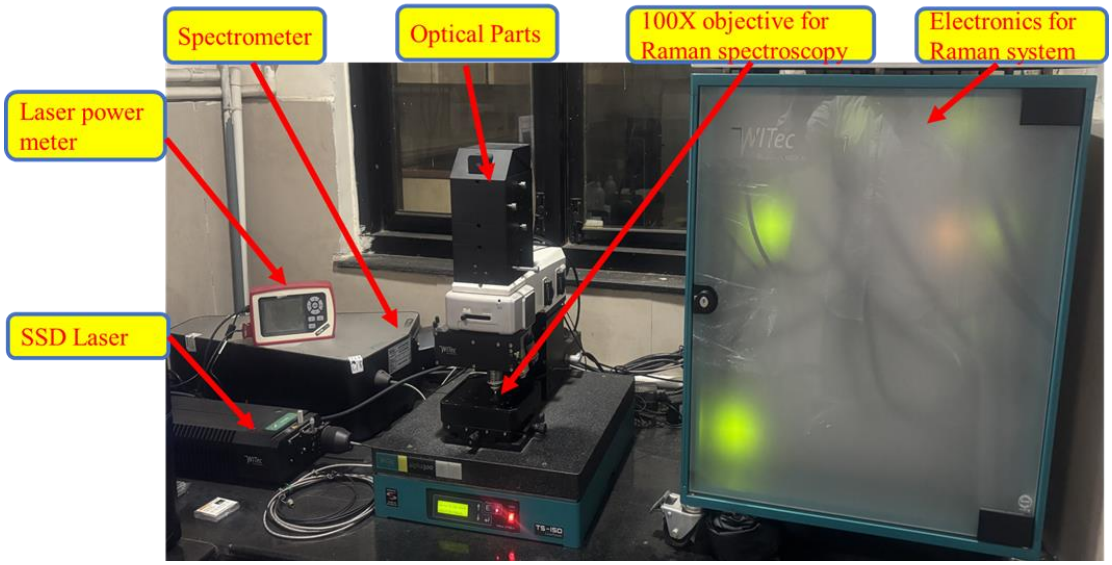

Fig.: 2.16 Raman Spectroscopy alpha 300 RA from WITec

Gas lasers, including Ar+, diode-pumped solid-state lasers, and tunable lasers are among the different types of lasers. Before the scattered light reaches the spectrometer and the detector (CCD camera), notch filters are used to reduce the Rayleigh line amplitude. One useful technique for characterizing oxide thin films is Raman spectroscopy. Few specific advantages of Raman spectroscopy apply to thin films and heterostructure are mentioned here; useful tools in confirming phase purity and crystal structure, examining lattice distortions, strain, and stress, as these factors significantly affect magnetic and electrical characteristics and detecting defects, disorders, and secondary phases that can occur in the deposition process. Fig. 2.16 shows the Witec make alpha 300 RA Raman spectroscopy equipped with 532nm of solid-state laser diode. is frequently utilized for yttrium iron garnet (YIG) films in order to assess crystallinity and confirm the garnet phase's growth. Characteristics Fe–O and Y–O vibration-corresponding Raman-active phonon modes are reliable markers of superior epitaxial YIG films [151]. Furthermore, as metals often lack Raman-active modes, the absence of Raman peaks caused by metal layers confirms the

existence of heterostructures of nonmagnetic metals. Therefore, Raman spectroscopy is a complementary technique to X-ray diffraction (XRD) that helps to better understand the vibrational characteristics, interfacial quality, and structural quality of magnetic thin films used in spintronics. Raman spectroscopy in the 100 - 4000 cm^{-1} range was performed using a WITEC Raman spectrometer equipped with a green laser light source of wavelength 532 nm.

2.3.2 Surface and morphology characterization

The electrical, spin transport, and magnetic properties of thin films are strongly influenced by their surface and shape, particularly in spintronic devices where interfacial phenomena are important. Therefore, it is essential to characterize microstructural characteristics, grain size, and surface roughness in order to determine growth quality and performance. Their interface sharpness, grain size, and roughness have a major impact on the dynamics of magnetization, spin pumping, and spin current transmission. To establish a relationship between the deposition process, film quality, and device performance, it is crucial to accurately characterize the surface and morphology.

2.3.2.1 Atomic force microscope (AFM)

Atomic force microscopy typically used ultrahigh sensitive scanning probe technique to investigate the topography and surface morphology of thin films at the nanoscale. Binnig, Quate, and Gerber invented AFM in 1986. Finding the interaction forces between a sharp probe (cantilever tip) and the sample surface is the foundation of AFM. It is a versatile technique for imaging almost any material, including oxides and insulators like YIG, because it does not require vacuum settings or conductive layers like electron microscopy requires. The term "atomic force" refers to a force that is Microscopy is a kind of scanning microscope that gathers information about the profile by scanning the sample surface with a tip [152, 153]. It offers three-dimensional pictures of the film's surface and enables the quantitative assessment of surface homogeneity, grain size, and root mean square (RMS)

roughness. Surface roughness in magnetic thin films like YIG is closely related to the existence of other scattering mechanisms including two-magnon scattering, which can increase damping and broaden the ferromagnetic resonance (FMR) linewidth [154, 155]. As a result, AFM is an effective technique for enhancing deposition conditions to produce smoother surfaces and minimal magnetic losses. The sample surface is scanned by an AFM tip to produce topographical images. The radius of curvature of the AFM sharp tip is a few nanometers which is positioned in the bottom of silicon or silicon nitride made cantilever. Surface roughness causes the AFM probe tip to bend while scanning. A laser beam reflection at the tip end was used to measure the bending angle. Beam movement can be detected by the photodiode array and communicated as surface topography. A simplified illustration of the key elements of a typical AFM can be found in fig. 2.17. With an AFM, three imaging modes are usually available: contact, noncontact, and tapping [156]. In contact mode, cantilevers with lower stiffness are used to prevent drift and excessive noise. The sample may shatter on the surface, though, if there is a sufficient attraction between it and the tip. For the scanning force to be guaranteed to be repulsive, a constant deflection must be maintained.

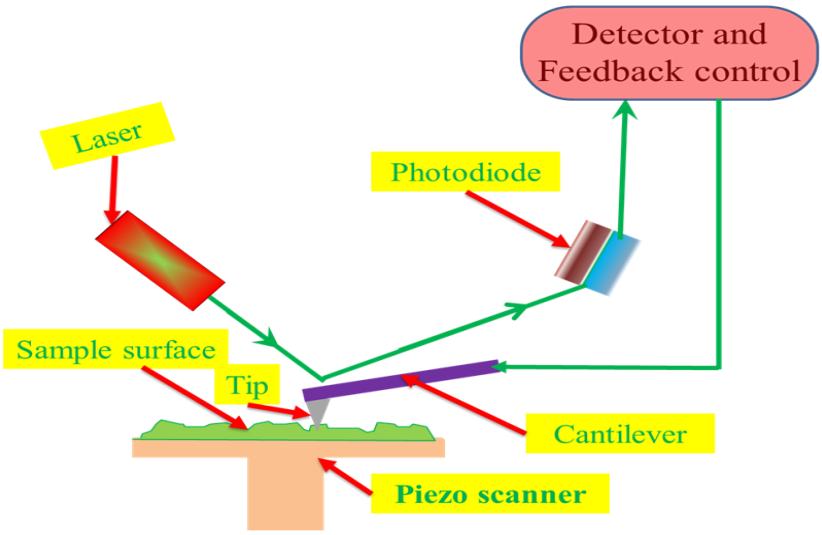

Fig.: 2.17 Schematic representation of AFM

The oscillation frequency in non-contact mode is influenced by a force between the tip and the sample surface, and it is marginally greater than natural resonance. A WITec AFM, Model No. alpha 300 RA, operating at room temperature was used in the present work (see figure 2.18).

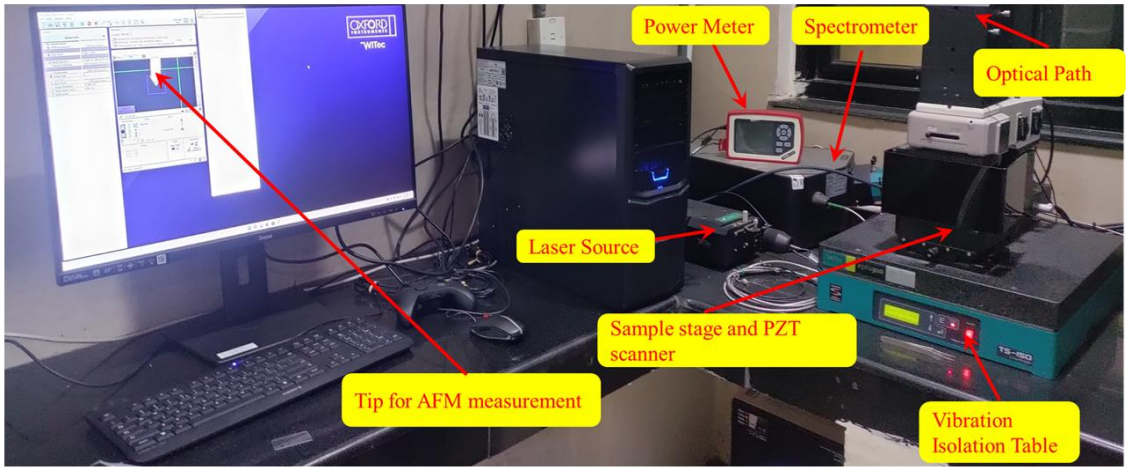

Fig.: 2.18 Alpha 300 RA AFM from WITec

This signal shift is detected via a feedback loop, which modifies the tip's location and frequency constant. A topographical image of the sample can be produced using the movement distance. This mode eliminates the possibility of overbending the tip, which could shatter and damage the sample, particularly if it is made of a sensitive material. However, in non-contact mode, the image quality may be impacted by a thin layer of moisture that forms on the sample in the absence of a vacuum. A contact mode tip, on the other hand, may get through this layer and pick up a stronger signal from the surface. Lastly, there is the tapping mode for scanning.

The increased oscillation amplitude (beyond 10 nm) causes the AFM scans to typically be slower in this mode than in any other. As it gets closer to the surface, the contact force would increase, reducing the oscillation amplitude. It may be possible to monitor and modify the cantilever's height using feedback loops. Each mode has its own benefits and

is selected based on the sample type and desired resolution. This tool's ability to detect nanoscale details and assess roughness makes it incredibly helpful for improving thin film performance for its application in the field of spintronics.

2.3.2.2 Scanning electron microscope (SEM)

One of the most flexible techniques for examining the microstructural characteristics, grain size, and surface topography of thin films is scanning electron microscopy (SEM). SEM uses a high-energy electron beam that is focused to nanoscale resolution, as opposed to wavelength-limited optical microscopy. Because of this, it is a particularly helpful technique to characterize heterostructures and thin films used for spintronics. In SEM, an electron beam is generated using a thermionic or field-emission electron source, and it is focused onto the sample surface using a system of electromagnetic lenses. Secondary electrons (SE), backscattered electrons (BSE), and characteristics X-rays are among the signals produced by electron–matter interactions as the beam moves across the sample.

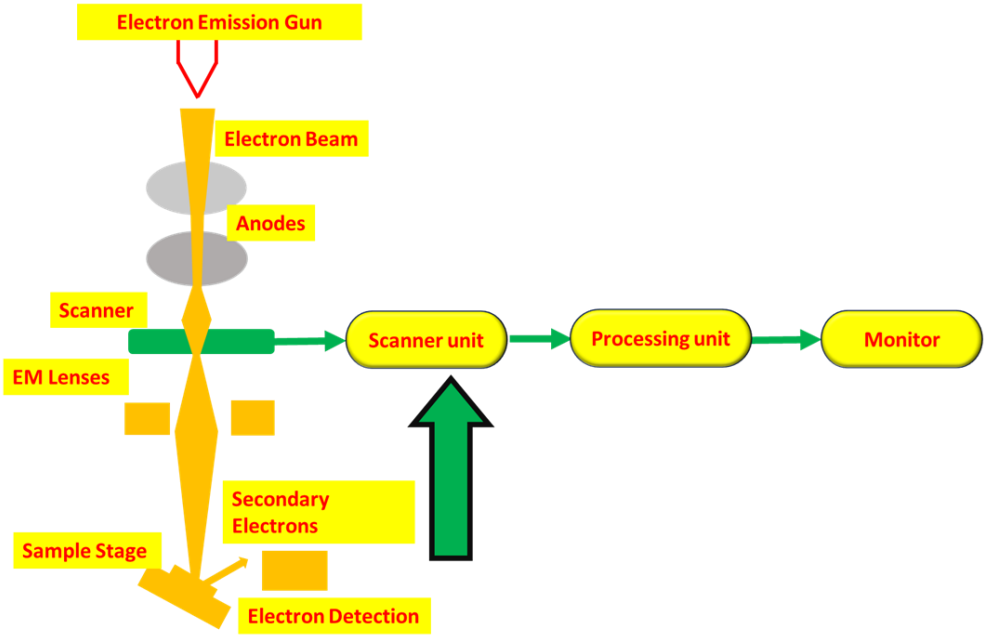

Fig.: 2.19 Schematic representation of SEM

Secondary electron detection, which provides accurate information on surface topography, texture, and morphology, is the most widely used secondary electron imaging approach. Surface profile research makes considerable use of SEM, a type of electron microscopy. By scanning the sample surface with extremely high-energy electron beams and interacting with the sample atoms, the scattered electrons provide details on the structure and topography of the surface [157-159].

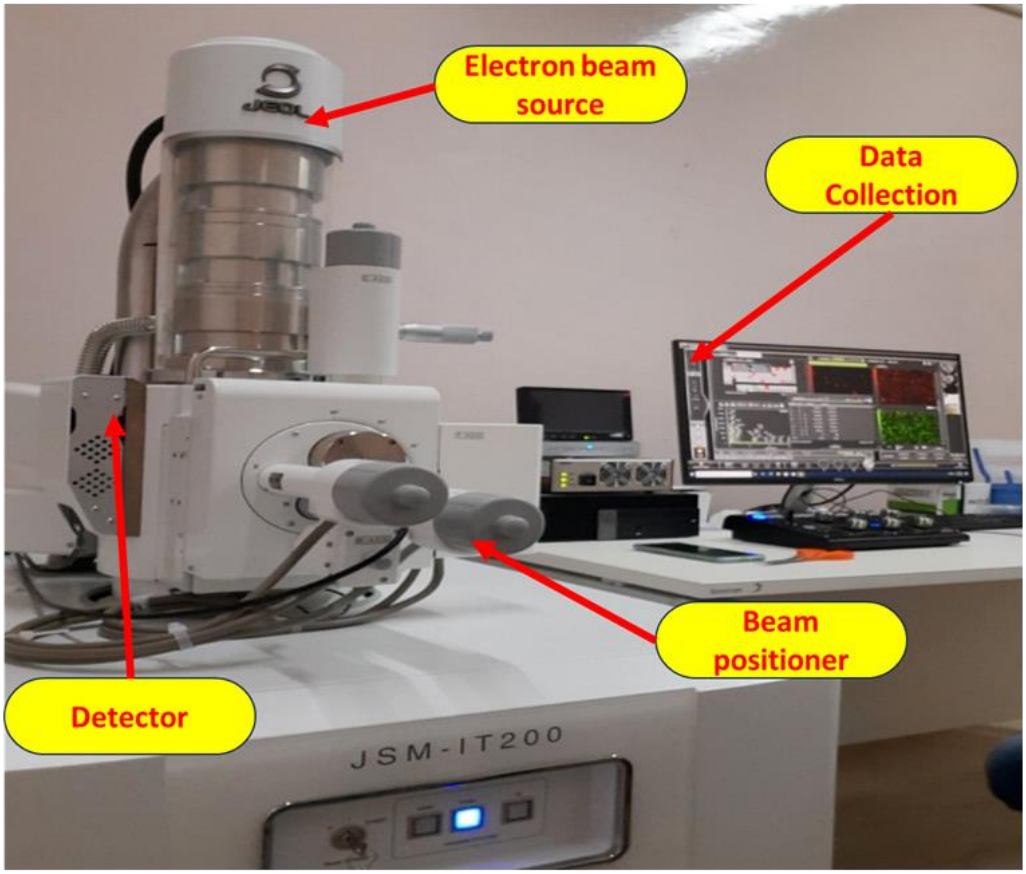

Fig.: 2.20 SEM model JSM-IT200 from Jeol

It is possible to improve the resolution to a few nanometers by applying a high acceleration voltage to the electron beam.

One of the main benefits of SEM imaging is that, because of its wide field profile, the area being examined may be rather big. To enable exact focus, the electromagnetic focusing lenses can be adjusted to a very fine level. Schematic diagram of scanning electron microscope is shown in fig. 2.19. SEM is one of the most significant instruments in Surface and Materials Science because of these two compensation techniques, which give researchers more details about a single sample.

Furthermore, there are certain disadvantages to the conventional SEM. Because the sample and detector are kept in a traditional vacuum chamber under about $10^{-5}\ mbar$ of pressure, a high-energy electron beam may ionize airborne carbohydrates and produce carbon pollution in the sample. Furthermore, under extreme conditions, the experiment would not be viable for the analysis of non-conductive materials since the electric charge would be developed on the sample surface. The ideal solution is to apply a small layer of carbon or a highly conductive yet chemically stable metal, such as gold (Au), to the isolating surface. For thin film research, SEM analysis offers several advantages: visualization of the growth orientation and surface grain structure and detection of microstructure defects, pinholes, and cracks, in multilayered systems, cross-sectional imaging enables evaluation of interface quality, layer stacking, and film thickness. When combined with Energy-Dispersive X-ray Spectroscopy (EDX), SEM can further reveal elemental composition and distribution, which is useful for confirming the deposition of metals (Pt, Cu, W, NiO, etc.) on YIG. SEM helps ensure smooth and flat film growth for spintronic thin films. The effectiveness of spin transport can be compromised by any morphological defects or defects in grain boundaries acting as scattering centers. Therefore, SEM offers both qualitative and semi-quantitative information concerning thin film morphology, making it a complimentary technique to Atomic Force Microscopy (AFM) and Transmission Electron Microscopy (TEM). A JEOL (JSM-IT200) SEM-EDX apparatus (shown in figure 2.20) is used in this thesis for elemental analysis and surface morphology study.

2.3.2.3 Energy dispersive X-ray spectroscopy (EDS/EDX)

42

For the elemental examination of materials, Energy Dispersive X-ray Spectroscopy (EDS or EDX) is a common analytical technique used in conjunction with Transmission Electron Microscopy (TEM) or Scanning Electron Microscopy (SEM). When a specimen is exposed to a high-energy electron beam, it produces distinctive X-rays, which are then measured by EDS. Core holes are created when the sample is struck by an incoming electron beam, which excites and ejects inner-shell electrons from the sample's atoms. X-rays with energies typical of the elements included in the material are released by the ensuing electronic transitions from higher energy to lower energy. To determine the elemental composition of the thin films both qualitatively and quantitatively, EDS measures the energy and intensity of these produced X-rays [157]. Schematic representation of EDS is shown in fig. 2.21. EDS has several applications in the field of thin film research few of them discussed below,

Elemental Identification: Confirms the elemental composition of film deposited and the anticipated single layer / heterostructure's composition.

Depth and Interface Information: To verify element distribution across interfaces, EDS can probe a multilayer stack in cross-section mode.

In spintronics, where interfacial quality is crucial for spin current transmission, impurity detection is crucial for detecting accidental contamination or oxidation.

Complementary Analysis: EDS helps XRD and Raman by confirming the chemical composition of the layers, even though they provide phase and structural data. Despite providing precise elemental identification, EDS's accuracy for light elements ($Z < 5$, such as H, Li, or B) is low due to its low X-ray emission efficiency. Nonetheless, it continues to be one of the most effective and widely used compositional analysis methods for oxide and metallic thin films.

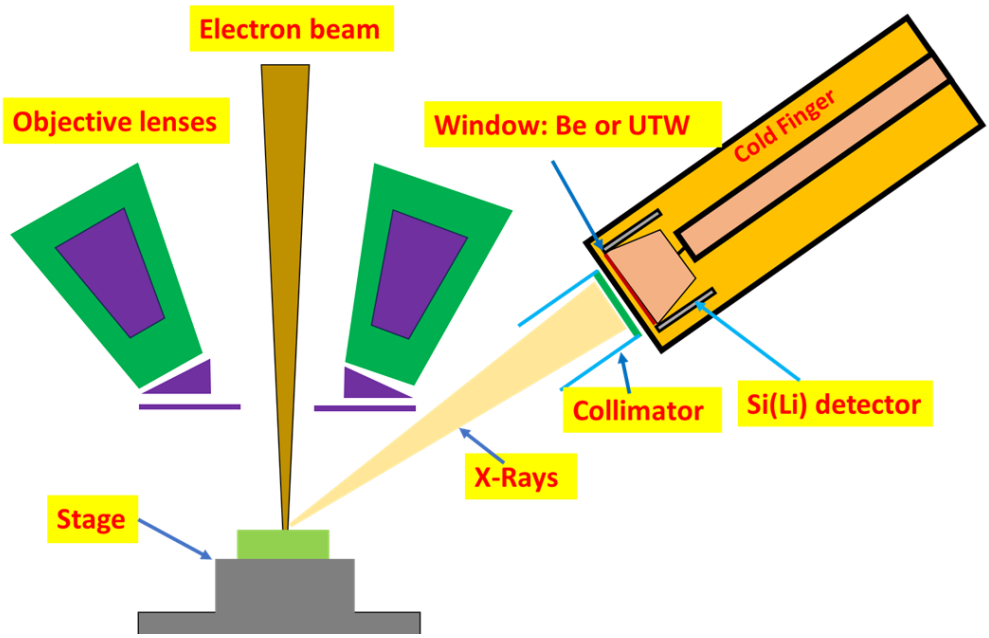

Fig.: 2.21 Schematic representation of EDS

In this work JEOL make JSM-IT200 equipped with EDS shown in fig. 2.20 used for elemental composition detection and complementary to the XRD and Raman techniques.

2.3.3 Magnetic characterization techniques

Because our work is focused on the deposition of magnetic thin film, multilayer and its application in the field of spintronics, it's critical to figure out their magnetic properties**.** Applications in spintronics and magnonics require an understanding of dynamic behavior and magnetic characteristics. Methods of both static and dynamic characterization are used in this work. The most widely used methods for analyzing magnetization dynamics in thin films, multilayers, and heterostructures are the Vibrating Sample Magnetometer (VSM) and Ferromagnetic Resonance (FMR).

2.3.3.1 Vibrating sample magnetometer (VSM)

One of the most popular techniques for examining the static magnetic characteristics of material systems, including bulk, thin-film, and nanoscale structures, is vibrating sample magnetometry (VSM). Because of its high sensitivity and multimode capabilities, it was initially developed by Foner in 1959 and has since become a standard instrument in magnetic characterization [160]. In a VSM, the sample is mechanically oscillated, frequently using a piezoelectric transducer, and exposed to a uniform magnetic field. The electromotive force (emf) produced by the sample's alternating magnetic dipole moment is proportional to the magnetic moment of the pickup coils around it. A lock-in amplifier is used to measure this induced voltage, enabling high sensitivity even for weak magnetic signals. The two most popular types of magnetometry are inductive and force-based. This thesis uses vibrating sample magnetometry (VSM), the most used inductive method. The superconducting quantum interference device (SQUID) magnetometer is another kind of measurement that falls within this category. To determine the type of magnetic ordering present and if phase transitions occur at critical temperatures or magnetic fields, both approaches necessitate placing the sample within a magnetometer [161]. Schematic representation of VSM is shown in fig. 2.22.

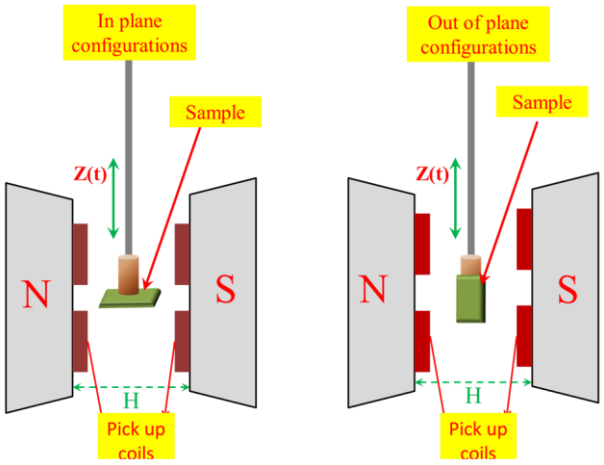

Fig.: 2.22 Schematic representation of VSM

We used the J3120 model of cryogenic made physical properties measurement system (PPMS) for the magnetic properties measurement with variable temperature insert (VTI) and equipped with the VSM probe [162]. The maximum magnetic field of this equipment is between -14 and +14 Tesla, while the temperature range is between 1.6 and 600 K for magnetic measurement. A sample is positioned inside a specifically designed set known as pick-up coils in the VSM technique. A magnetic moment is induced in the sample by a homogeneous magnetic field in proportion to the applied field strength and sample susceptibility. Faraday's law of induction states that when the sample is vibrated, an electrical signal proportional to the magnetic moment m is induced into the coils. Actual setup of PPMS with VSM probe is shown in fig. 2.23.

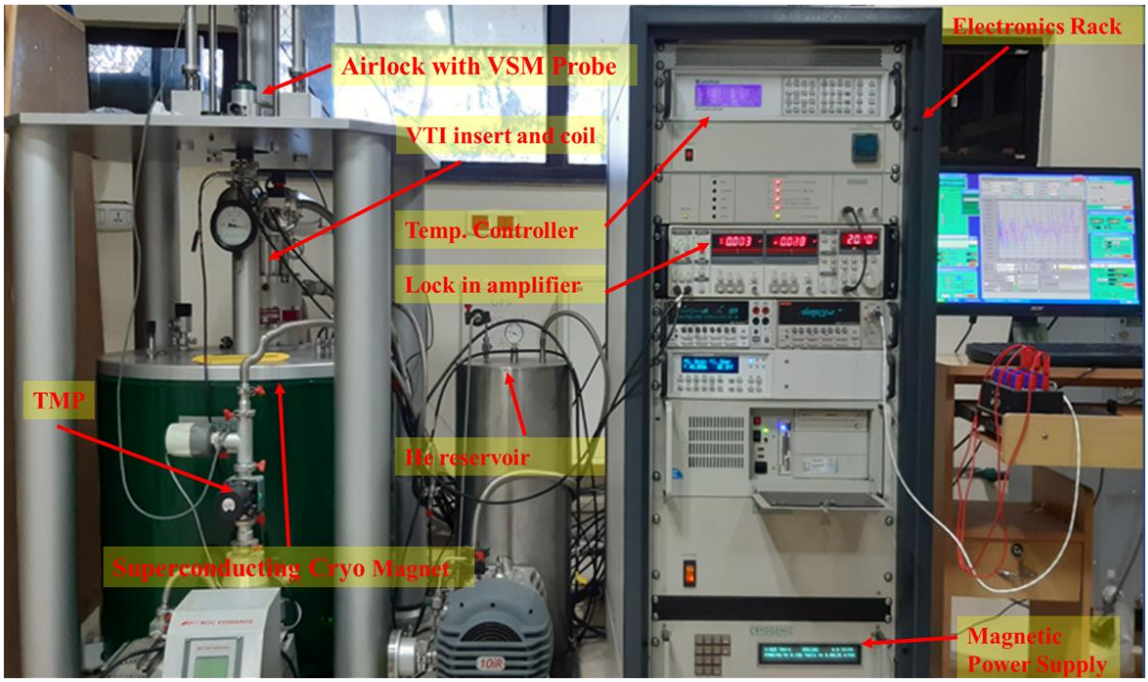

Fig.: 2.23 PPMS system J3120 equipped with VSM probe from cryogenic limited.

This equipment is cryogen free system and using the superconducting magnet for high magnetic field and lowest possible temperature is 0.3 K with the helium-3 probe. Cryogenic make PPMS system equipped with a cryostat, a variable temperature inserts

(VTI), VSM Coil, a superconducting magnet, and a cryo-cooler. It is having different probes HT-VSM, LT-VSM probe for magnetic measurement and complete electronics rack with lock in amplifier, temperature controller, magnetic power supply, source and voltmeter and valve control system. VSM is used for several application few of them is mentioned here; Studies on magnetic materials, such as ferrimagnetic, antiferromagnetic, and ferromagnetic materials, is carried out, research on thin films, nanostructures, and magnetic nanoparticles, evaluation of magnetic properties for data storage, magnetic sensors, and magnetic recording media and investigating the magnetic hysteresis loops and domain structures. VSM is essential for evaluating the intrinsic ferromagnetic character of thin films while taking substrate contributions into account (e.g., the paramagnetic response of GGG in YIG films). It is possible to comprehend domain features, interfacial effects, and magnetization reversal processes by looking at hysteresis loops. In magnetic heterostructure research, where precise control of magnetic parameters directly influences spintronic processes such as spin pumping, spin-transfer torque, and spin-orbit torque, VSM is essential because it can provide a quantitative explanation of magnetization.

2.3.3.2 Ferromagnetic resonance (FMR)

The dynamic magnetic behavior of ferromagnetic and ferrimagnetic materials can be effectively examined using Ferromagnetic Resonance (FMR). Unlike equilibrium-probing static techniques such as VSM, FMR investigates the precessional motion of magnetization while an external magnetic field is present and acted upon by a microwave field [100]. When the magnetization of a magnetic substance is directed against the direction of the external magnetic field, a torque is present. This torque will be the cause of the magnetization precession [100, 163, 164]. When the angle remains constant during the precession, this is known as uniform precession. In real materials, the precession will be dampened by the interactions of the magnon-phonon, magnon-electron, and magnon-magnon. The precession angle will progressively drop to zero in the absence of a driving

force. This type of phenomenon is called magnetization relaxation. Ferromagnetic resonance is frequently used to study the kinetics of magnetization [29]. The FMR response measurement gives information about the material's static magnetic properties, like saturation magnetization and anisotropy field, as well as its dynamic magnetization characteristics, like damping and relaxation rate. One of the main challenges in magnetic insulator-based spintronics is the reciprocal relationship between spin currents and magnetization precession. A spin current can influence magnetization precession by angular momentum transfer at the interface between the normal/noble metal (NM) and ferromagnetic insulator (FMI). This is accomplished by either spin pumping or interfacial spin distribution. The FMR approach is a straightforward technique for statistically assessing the effectiveness of angular momentum transfer and measuring damping. FMR is the most widely used method for researching magnetization dynamics, as was previously mentioned. A driving force that overcomes the damping will allow the magnetization to continue without causing the precession angle to decrease. This phenomenon is known as "driving precession". The schematic representation of FMR is shown in fig. 2.24 whereas actual VNA-FMR setup used for this work is shown in fig. 2.25.

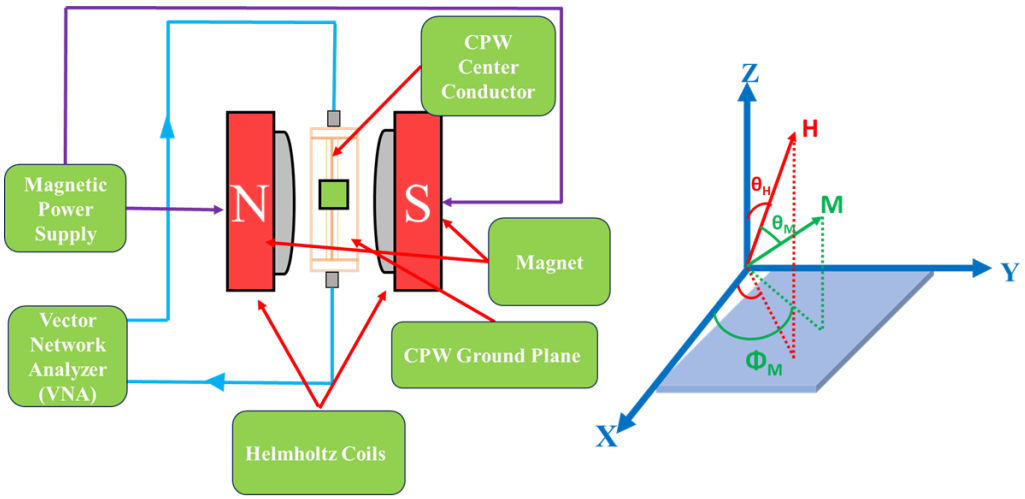

Fig. 2.24 Schematic representation of FMR and its co-ordinate system

A microwave magnetic field-oriented perpendicular to the external magnetic field serves as the FMR system's driving force. In order to understand the dynamics of magnetization, one can apply the Landau-Lifshitz-Gilbert equation [165].

$$\frac{d\vec{M}}{dt} = -\gamma\left(\vec{M} \times \vec{H}\right) + \frac{\alpha}{M_S}\left(\vec{M} \times \frac{d\vec{M}}{dt}\right) \tag{2.2}$$

The damping constant, represented by α, can be determined using FMR measurements. Field scans and frequency scans are the two categories of FMR scan methods. While the magnetic field swings continuously, the former functions at a constant microwave frequency, while the latter maintains a constant magnetic field while varying the frequency. Whatever scan mode is used, the material will absorb the most power until the field/frequency reaches resonance. During measurements, the sample is positioned near the center of the magnetic field, either in the cavity or the shorted waveguide. The microwaves are subsequently emitted by the microwave generator and reach the sample via the waveguide. Depending on the microwave frequency, the FMR linewidth changes.

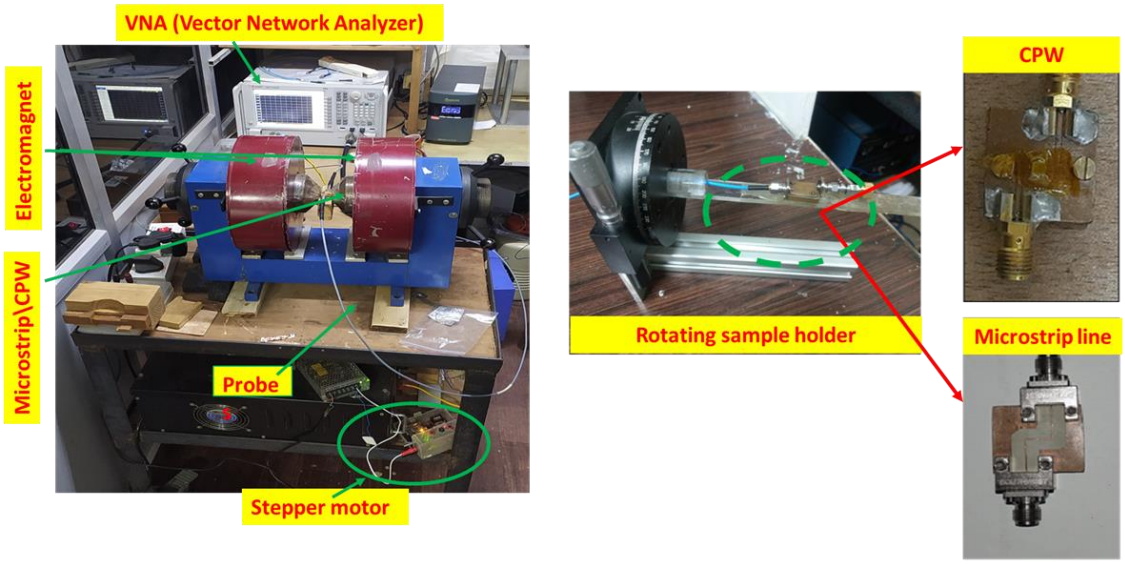

Fig.: 2.25 VNA-FMR System with different measurement setup

The relationship between the frequency and the FMR linewidth is described by the linear equation.

$$\Delta H_{pp} = \Delta H_0 + \frac{4\pi\alpha}{\gamma} f \tag{2.3}$$

The Gilbert damping constant is measured here by the slope, and a steeper slope indicates a higher damping constant. Frequency-dependent FMR data can be used to calculate the samples' Gilbert damping values. We used the experimental vector network analyzer ferromagnetic resonance (VNA-FMR) to perform FMR measurements across a broad frequency range. The N5224A VNA from "Keysight Technologies," which operates in the frequency range of 10 MHz to 43.5 GHz, was used in this experiment. The flip-chip arrangement is used for the measurements. According to this, the sample is oriented downward onto the co-planar wave guide (CPW). The VNA connected to the CPW determines the S-parameters in respect to the external magnetic field (H) and the excitation frequency (f). Since we perform a continuous wave experiment, we obtain S-parameters for a distinct external magnetic field (H) and angles (θ, ϕ). FMR is used to investigate spin pumping, spin mixing conductance, and interfacial damping mechanisms in thin film heterostructures, where it is particularly significant. FMR is consequently essential for the development of spintronic and magnonic devices since it not only provides intrinsic insight into magnetization dynamics but also directly connects to spin transport effects.

Chapter 3

Effect of oxygen growth-pressure on microstructural and magnetic properties of pulse laser deposited epitaxial YIG thin films

We investigated the effect of oxygen growth-pressure on the structural and magnetic properties of epitaxial YIG thin films. YIG films were grown on single crystalline GGG substrates with (111) orientations by pulse laser deposition technique. In-situ oxygen-gas pressure variations in the range of 0.0025 mbar to 0.15 mbar was adopted to demonstrate the perfect growth. Structural analysis confirmed that the films were single crystalline in nature. Atomic force microscopy analysis indicated that roughness of the films decreases with increase of oxygen pressure. Saturation magnetization was enhanced by a factor of 17% over increase of oxygen pressure. Through angular dependent ferromagnetic resonance (FMR) measurements along film's in-plane (φ-variation) and out-of-plane (θ-variation) geometries, resonance fields$[H_r(\theta_H, \varphi_H)]$ and FMR linewidths$[\Delta H_r(\theta_H, \varphi_H)]$ were obtained. Using theoretical analysis important material parameters such as; saturation magnetization, gyromagnetic ratio, uniaxial anisotropy, cubic anisotropy and Gilbert damping were evaluated. We have obtained lowest Gilbert damping $\sim 4.37 \times 10^{-5}$ for 0.15 mbar oxygen pressure deposited YIG film.

3.1 Introduction

Yttrium iron garnet ($Y_3Fe_5O_{12}$, YIG) a well-known ferrimagnetic insulator has been extensively explored in various applications of spintronics, magnonics and microwave passive and active devices [92, 166-171]. This is due to its low magnetization damping ($\sim 10^{-5}$) which allows spin-wave propagation to be observed over hundred-micron distance. In addition, YIG also has high Curie temperature (560 K) which makes it suitable for these applications. Recently, YIG thin films have attracted a lot of interest in the fundamental study of spin wave propagation, spin-wave logic devices, spin-transfer-

torque oscillator and spin pumping studies etc. [172-175]. The magnetization relaxation plays a crucial role in sub-micron thin films from technological perspective for fabricating nanometer scale devices. The magnetization relaxation mechanism comprises of intrinsic and extrinsic contributions which involve magnon-magnon interaction, magnon-phonon interaction, scattering due to sample defects and two-magnon scattering at the interface and/or surface of the films, are of particular interest now-a-days [175-182]. These relaxation process can be understood fundamentally by the knowledge of Gilbert damping. Further, there is an intense surge for understanding the phenomenological importance of magneto-crystalline anisotropies such as uniaxial anisotropy and cubic anisotropy which arises due to phonon-magnon interactions in ultra-thin films, especially the epitaxial films. One can achieve possible device applications in spintronics by tailoring the anisotropy and Gilbert damping parameters through deposition processes/parameters [22, 182]. Spintronics has immense potential to provide logic and memory devices with high speed, low power and high-density capabilities [183].

High quality YIG thin films can be prepared by variety of chemical and physical techniques [19-21]. In general, physical methods using vacuum-based processes are preferred to improve the quality and phase of YIG thin films to achieve low damping. Pulsed laser deposition (PLD) technique has several advantages in controlling the stoichiometry, thickness and magnetic properties of thin films. Recently, high quality YIG thin films have been deposited using pulsed laser deposition technique (PLD) [23,24, 184-186]. Lichuan et al. studied the effect of annealing temperature on material composition and magnetic properties and reported Gilbert damping constant of 5.74×10^{-4} for YIG thin films annealed at 800 °C [20]. Van et al., investigated the role of annealing temperature on the crystallinity, surface roughness and line width of ultrathin YIG films [187]. Bhoi et al. observed that saturation magnetization increases and the FMR linewidth decreases with the increase of film thickness [170]. Bhoi et al. also reported the effect of oxygen pressure on the saturation magnetization and FMR linewidth of YIG films deposited on quartz substrates [188].

None of these above studies reported were on epitaxially grown YIG films. Further, no studies have been reported so far on the angular dependent FMR measurements of epitaxial YIG thin films deposited on GGG (111) substrates along with the effect of variation of oxygen gas growth pressure during film growth. These gives us immense motivation to artificially engineer the above-mentioned material properties specially for microwave device applications with the variation of oxygen gas pressure during thin film growth.

In the present work, high quality single-crystalline YIG thin films were deposited on GGG (111) substrates using pulsed laser deposition technique (PLD) at elevated temperature. The influence of different oxygen gas pressure during thin film growth have been investigated on the structural and magnetic properties. The phase formation and crystallinity of the films were examined using X-ray diffraction (XRD) and Raman spectroscopy. Surface morphology was visualized using atomic force microscopy (AFM). DC magnetic properties were investigated using vibrating sample magnetometry (VSM). The angular dependent FMR measurements in the "in-plane (φ-variation)" and "out-of-plane (θ-variation)" geometries were performed to evaluate various magnetic anisotropy and Gilbert damping parameters. We observed that the Gilbert damping constant and anisotropy constants are strongly dependent on the oxygen gas pressure during the growth of epitaxial YIG films. The micromagnetic simulations using Landau-Lifshitz-Gilbert formalism were performed to determine the FMR mode positions and linewidths.

3.2 Experimental details

For the fabrication of YIG thin films, we prepared YIG target (diameter - 1 inch) synthesized by conventional solid-state reaction method using yttrium oxide (Sigma - Y_2O_3, 99.99% pure) and iron oxide (Sigma - Fe_2O_3, 99.99% pure) powders. Pulsed laser deposition (PLD) technique was employed to prepare YIG thin films on single crystalline GGG (111) substrates from MTI Corporation (Richmond, USA). Prior to deposition, the

substrates and the vacuum chamber were cleaned thoroughly. The PLD system consists of a KrF excimer laser of wavelength 248 nm. To grow high quality YIG thin films we have used pulse repetition frequency of 10 Hz to ablate the target at 300 mJ energy. The distance of substrates from the target was kept fixed at 4 cm. The base pressure was maintained at 1×10^{-6} mbar using turbo molecular pump. The substrates were pre-heated at 800 ºC to remove top layer impurity if any. The deposition was carried at four different oxygen pressures with a wide variation (of three order of magnitude), vide values from 0.0025 mbar, 0.025 mbar, 0.10 mbar and 0.15 mbar at same annealing temperature. The films were grown at a rate of ~ 0.5 Å/sec. A fixed number of shoots of 15,000 were applied for film deposition at each oxygen pressure. Detailed deposition parameters were tabulated in table 3.1. The as-grown thin films were annealed in-situ for 2 hours at 800 ºC and then cooled down to room temperature in the presence of oxygen throughout the process. After deposition, the film thicknesses were measured by using AFM and found to be ~90 nm.

The structural properties of the thin films were investigated by X-ray diffraction (XRD - Miniflex Rigaku diffractometer) technique using Cu K_α radiation (λ =1.5406Å). The roughness and quality of the films were measured with the help of an atomic force microscopy (AFM - WItech Alpha 300 RA) system using AC (tapping mode) mode with the help of non-contact cantilever of low force constant (45 N/m) and high resonant frequency (250 KHz). The dc magnetic measurements were carried out using physical properties measurement system (PPMS – Cryogenics Limited (Model – J103), UK) with magnetic field applied along in-plane geometry of the film.

Detailed ferromagnetic resonance (FMR) measurements were carried out by using a Vector Network Analyzer (VNA - Keysight, USA) system in conjunction with a “S” shaped coplanar waveguide (CPW) in a flip-chip configuration, where dc magnetic field was applied perpendicular to the high-frequency magnetic field (h_{RF}). We have performed two different variety of FMR experiments. (i) In the first set-up we have rotated the CPW inside the electro magnet pole pieces in the plane of the film to perform the “in-plane (φ-

variation)" measurements to deduce the angular variation of resonance fields "H_r" and resonance linewidths "ΔH". These experiments are extensively performed to verify the epitaxial growth of the thin YIG films on GGG (111) substrates and to derive the uniaxial and cubic magneto-crystalline anisotropy parameters. (ii) In the second set of experiment, to perform the "out-of-plane (θ-variation)" studies we have rotated the CPW set-up inside the magnet pole pieces from film in-plane direction to out-of-plane (*i.e.* film perpendicular to dc magnetic field direction) and further rotated to in-plane direction covering all 360° angles at a step of 10° to observe the FMR resonance fields and resonance linewidths from zero degree to 360° at each 10° increments. The CPW used to perform these experiments was fabricated on a RT/duroid® 5870 high frequency laminate having double side lamination with PTFE fiber-glass dielectric substrate. The designed signal line width was 1 mm and the gap between the signal line and the ground plane was 38 μm to maintain an impedance of 50 Ohms for the transmission line structure.

The FMR spectra were obtained at a fixed frequency in the field sweep mode by sweeping the dc magnetic field by a computer-controlled sweeping system with a rate matching to VNA data acquisition rate. The field sweep was performed from 0 to 8 kOe magnetic field range. Further, the measurements were performed at different frequencies in the field sweep mode to derive FMR resonance fields and resonance linewidths from zero degree to 360° at each 10° increments to applied dc magnetic field both for "in-plane (φ-variation)" and "out-of-plane (θ-variation)" configurations. Thereafter, various magnetic parameters of the YIG thin films were derived using computer generated fitting routine to the Landau-Lifshitz Gilbert (LLG) equation suitable for thin film geometry.

The theoretical modeling was done using a micromagnetic code developed in Fortran programming language. Various parameters like FMR mode positions, intensity and linewidth were obtained which strongly depend on the equilibrium spin configuration.

Table 3.1: Deposition parameters used for YIG thin films on GGG (111) substrates.

Deposition Parameters	**Value**
Substrate Temperature (°C)	800
Oxygen Pressure (mbar)	0.0025, 0.025, 0.10 and, 0.15
Laser Energy (mJ)	300
Pulse repetition frequency (Hz)	10
Target to substrate distance (mm)	50

3.3 Results and discussion

3.3.1 Microstructural analysis

3.3.1.1 X-Ray diffraction patterns analysis

X-ray diffraction (XRD) technique was used to characterize the structural properties of the YIG thin films. Fig. 3.1 (A) confirms that only (111) oriented reflection family exist in YIG films and there is no indication of any additional phase. Fig. 3.1 (B-D) shows the XRD patterns of the deposited YIG thin films at different oxygen pressure conditions. All the deposited films showed the signature of single crystallinity over GGG (111) substrate. The narrow region was scanned repeatedly to thoroughly examine the YIG peak (as shown in the inset). The split peaks observed in the (111) plane of the GGG substrate were attributed to the $K_{\alpha1}$ and $K_{\alpha2}$ lines of the incident X-ray. The weak peaks at $2\theta = 50.5°$ and $50.8°$, corresponds to the $K_{\alpha1}$ and $K_{\alpha2}$ (111) plane of the YIG film. The lattice constant, lattice strain (lattice misfit *with respect to* substrate), and lattice volume were determined from the XRD data and are tabulated in Table 3.2.

Lattice constant $\boldsymbol{a}$ for the cubic structure is evaluated using [189],

$$\boldsymbol{a} = \frac{\lambda\sqrt{h^2+k^2+l^2}}{2\sin\theta} \quad (3.1)$$

where λ is the wavelength of Cu-Kα radiation, θ is the diffraction angle, and [h, k, l] are the miller indices of the corresponding XRD peak.

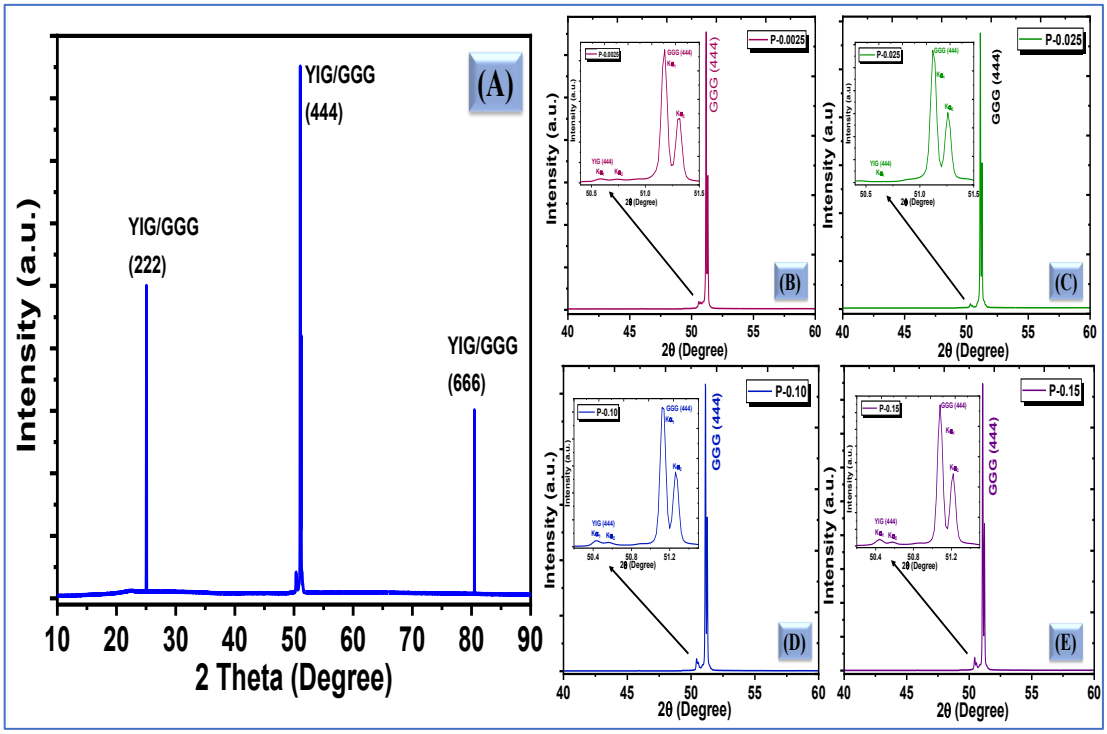

Fig.3.1: (A) Wide scan diffractogram of 0.15 mbar YIG thin film. (B-D) XRD spectra of YIG thin films on GGG substrate at different oxygen pressure. Inset shows the zoom out of arrowed region.

Lattice misfit $\left(\frac{\Delta a}{a}\right)$ is evaluated using Eq. (3.2) [190, 191],

$$\frac{\Delta a}{a} = \frac{(a_{film} - a_{substrate})}{a_{film}} \times 100\% \qquad (3.2)$$

where a_{film} and $a_{substrate}$ are the lattice constant of film and substrate respectively. The lattice constant of pure YIG bulk is 12.377 Å and of GGG substrate is 12.383 Å [192]. It is observed that the lattice constant increases from 12.379 Å to 12.458 Å with the increase in oxygen pressure from 0.0025 mbar to 0.15 mbar. The lattice strain of YIG films also

changes from 0.0032 % to 0.0040 % with oxygen pressure which corresponds to small lattice mismatch. The increase of oxygen partial pressure resulted in the lattice expansion during film growth [193] and the strain induced by the thermal expansion between the film and substrate enlarged the lattice constant [194].

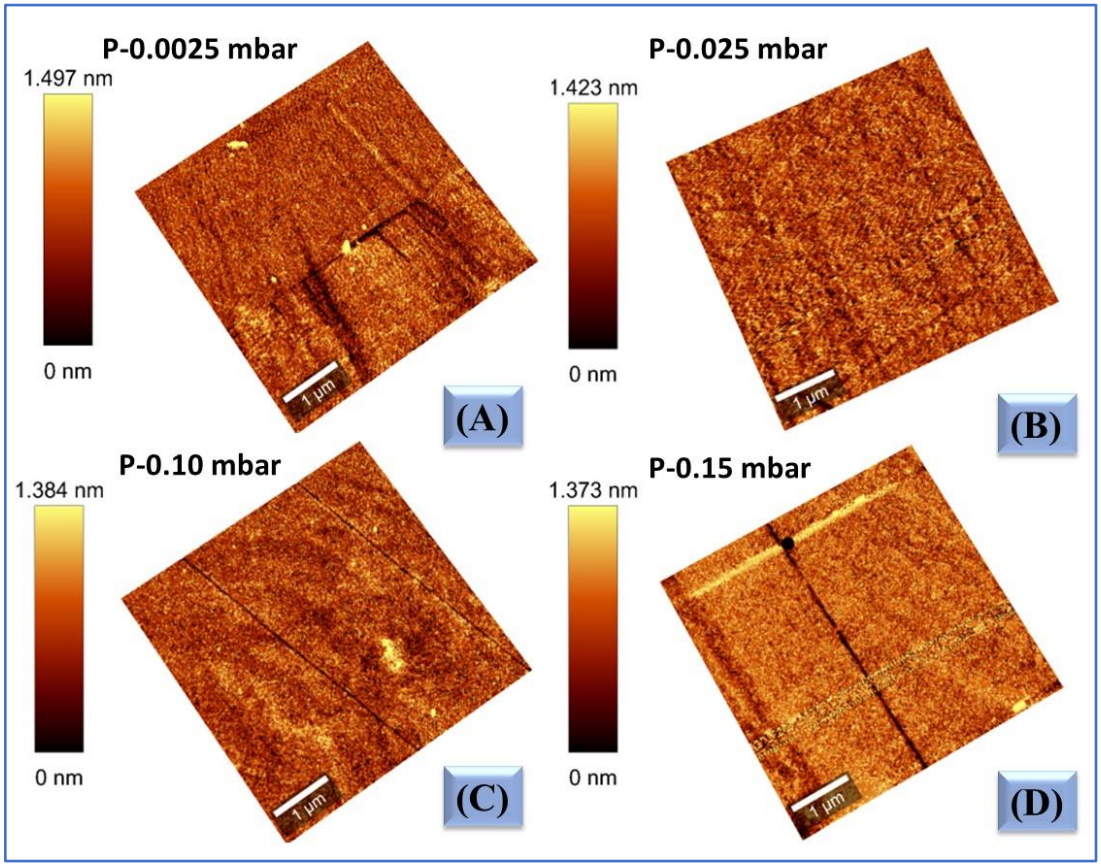

Fig.3.2: AFM images of YIG thin films at oxygen pressure of (A) 0.0025 mbar (B) 0.025 mbar (C) 0.10 mbar and (D) 0.15 mbar respectively.

3.3.1.2 AFM micrograph analysis

Fig. 3.2 (A-D) shows the surface morphology of the films at all the oxygen pressures samples using AFM. The root mean square (rms) roughness was extracted from the topographic images of all the samples and was found to be less than 0.6 nm. Low rms

roughness indicates that all the films exhibit a smooth and continuous surface which further improves with increasing oxygen pressure. Hence, it is verified in the present investigation that the high oxygen pressure permits sufficient oxygen required for phase formation and resulted in a perfect epitaxial growth to achieve a smooth continuous film with enhanced crystallinity. The crystallite parameters and surface roughness for all the samples are tabulated in table 3.2.

3.3.1.3 Raman spectra analysis

Fig. 3.3 (A) shows the Raman spectra of all the investigated YIG thin films. According to group theory, the cubic symmetry of YIG based crystal structure represents 25 Raman modes ($3A_{1g}+ 8E_g + 14 F_{2g}$) [195, 196]. The Raman spectra of YIG thin films studied in the present work demonstrates peaks around 168, 180, 235, 269, 381, 415, 485, 580, and 600 cm^{-1} respectively. The ferrimagnetic nature can be linked with the most intense peak at 269 cm^{-1} which represents $L[FeO_4]^{5-}$ translational modes. The A_{1g} modes at peaks 355 and 741 cm^{-1} is associated to internal vibrations of GaO_4 and GaO_6 in GGG substrates respectively [197]. The peak intensity of the Raman spectra increases for higher oxygen gas pressure (0.1 and 0.15 mbar) samples which also confirms better crystallinity [198, 199].

Table 3.2: Structural parameters such as lattice constant, lattice strain, lattice volume and root mean square value of YIG thin films as a function of oxygen gas pressure.

Oxygen Pressure (mbar)	Lattice constant (Å)	Lattice strain (%)	Lattice volume ($Å^3$)	RMS (nm)
0.0025	12.379	0.032	1894.95	0.57
0.025	12.388	0.036	1895.95	0.44
0.10	12.456	0.040	1896.98	0.33
0.15	12.458	0.040	1896.98	0.27

3.3.2 Magnetic Characterization;

3.3.2.1 VSM data analysis

The M-H curve of YIG thin films prepared by PLD technique as a function of oxygen gas pressure are shown in Fig. 3.3 (B). The contribution of the paramagnetic behavior of GGG substrate has been subtracted using a linear function from the raw data obtained from VSM. The saturation magnetization of YIG films at higher oxygen pressure was found to be near the bulk value of YIG. The coercivity remain almost constant around 12 ± 2Oe for all oxygen pressure samples. The YIG films shows excellent soft magnetic nature due to low coercivity values. The low coercivity values corresponds to low magnetic inhomogeneities in YIG thin films [199]. Further, low magnetic inhomogeneities can also be depicted by almost independent strain as observed and tabulated in Table 3.2.

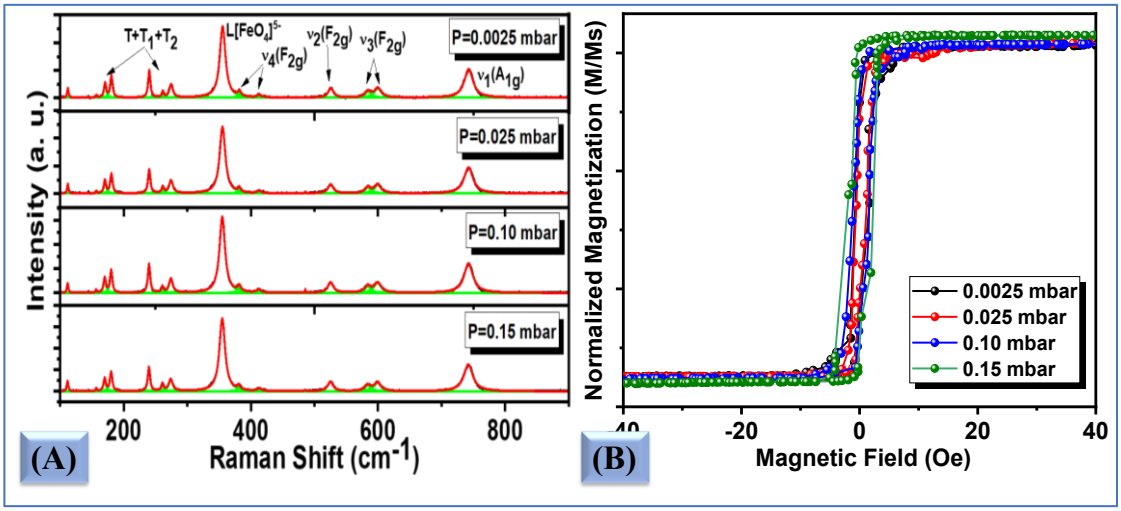

Fig.3.3: (A) Raman spectra of investigated YIG thin films at various oxygen pressure, here green solid curves correspond to individual peak fitting with Lorentzian profile function whereas red solid line represents the cumulative fitting of Raman spectra, (B) Hysteresis loop of all the samples at different oxygen pressure.

3.3.2.2 FMR data analysis

To understand the effect of oxygen gas pressure on various magnetic anisotropies and Gilbert damping we performed the angular dependent FMR measurements on epitaxial YIG thin films along "in-plane (φ-variation)" and "out-of-plane(θ-variation)" configurations as described in experimental section. The resonance fields and field line widths were derived from the FMR spectra using Lorentzian fits.

In the present investigation, [111] direction of cubic lattice is perpendicular to the film plane andθ_H and φ_H are the polar and azimuthal angle of the magnetization with respect to film direction.

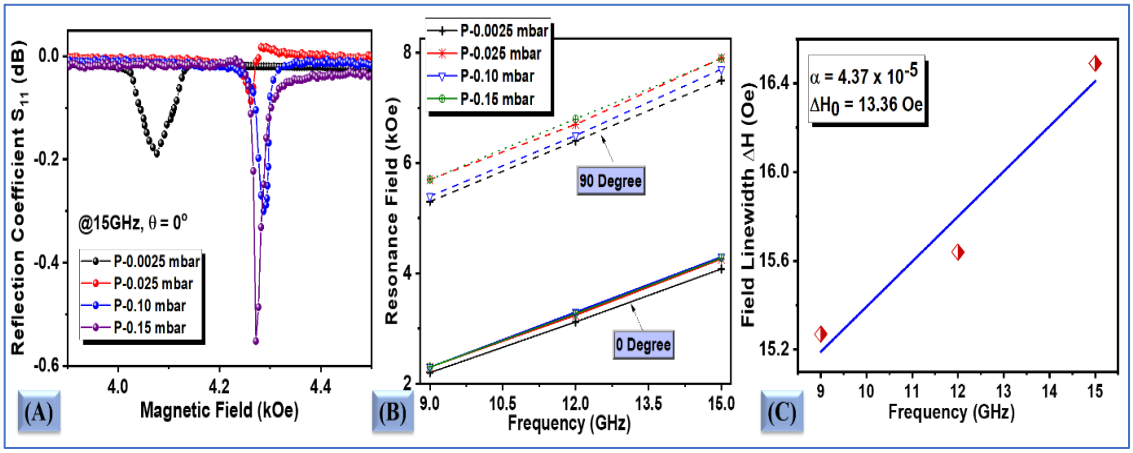

Fig. 3.4: (A) Oxygen pressure variation of FMR spectra of YIG samples as a function of pressure at 15 GHz and $\theta_H = 0°$. (B) Resonance field as a function of frequency for $\theta_H = 0°$ *and* 90°. (C) Frequency versus field linewidth for 0.15 mbar pressure sample.

The equilibrium orientation (θ, φ) of magnetization can be obtained by minimizing the free energy and the FMR resonance equation in equilibrium is given by [200].

$$\left(\frac{\omega}{\gamma}\right)^2 = \frac{1}{{M_s}^2 \sin^2\theta_M}\left[\frac{\partial^2 F}{\partial {\theta_M}^2}\frac{\partial^2 F}{\partial {\varphi_M}^2} - \left(\frac{\partial^2 F}{\partial\theta_M \partial\varphi_M}\right)^2\right] \quad (3.3)$$

where γ is the gyromagnetic ratio and M_s is the saturation magnetization. The angles θ_M and φ_M are chosen as the magnetization direction.

Applying the equilibrium conditions on the resonance equation (3.3), the film in-plane (φ-variation) and out-of-plane (θ-variation) geometries equations were derived as follows [201, 202].

For Out-of-plane (θ-variation):

$$\left(\frac{\omega}{\gamma}\right)^2 = \{Hcos(\theta - \theta_H) - 4\pi M_{eff}cos2\theta + H_{4\perp}(cos2\theta - cos4\theta)\}\{Hcos(\theta - \theta_H) - 4\pi M_{eff}cos^2\theta + 2H_{k_4}(cos^2\theta - cos^4\theta)\} \quad (3.4)$$

where, $4\pi M_{eff} = 4\pi M_s - H_{2\perp}$ is the effective field, $H_{2\perp}$ and $H_{4\perp}$ are out-of-plane uniaxial anisotropy and out-of-plane cubic anisotropy. For YIG (111) films, magneto-crystalline anisotropy gives rise to an easy-axis anisotropy along the film's in-plane direction. Hence, derivation and comparison of second and fourth order cubic magneto-crystalline anisotropies are important to justify the perfect epitaxial growth parameters.

For In-plane (φ-variation):

$$\left(\frac{\omega}{\gamma}\right)^2 = \left\{H + H_{4\parallel}cos4\varphi - H_{2\parallel}\cos\left(2\varphi - \frac{\pi}{2}\right)\right\}\left\{H + 4\pi M_{eff} + \frac{H_{4\parallel}(3+cos4\varphi)}{4} + H_{2\parallel}sin^2\left(\varphi - \frac{\pi}{4}\right)\right\} \quad (3.5)$$

where, $H_{2\parallel}$ is the in-plane uniaxial anisotropy, $H_{4\parallel}$ is the in-plane cubic anisotropy and $4\pi M_{eff} = 4\pi M_s - H_{2\perp}$, $H_{2\perp}$ corresponds to the out-of-plane uniaxial anisotropy in this case. Derivation of uniaxial and cubic anisotropies from angular variation in-plane FMR data justify the optimal growth parameters for epitaxial growth of YIG thin films.

Fig. 3.4 (A) shows the FMR spectra of YIG thin films at different oxygen pressure in the out-of-plane geometry of film at a frequency of 15 GHz and with $\theta = 0°$. The low oxygen pressure YIG samples (0.0025 and 0.025) show broader FMR spectra, whereas the high oxygen pressure samples (0.10 and 0.15) have much narrower FMR spectra. As we have already demonstrated in AFM images that high oxygen pressure YIG films have much

lesser surface roughness than lower O_2 pressure YIG samples. It is theoretically demonstrated in earlier publications [155, 203, 204] that surface roughness enhances two-magnon contribution to line width, hence we observed broader FMR spectra for 0.0025 and 0.025 O_2 pressure YIG films. Therefore, another marked feature of perfect epitaxial growth for higher O_2 pressure YIG films is that their spectra are much narrower and the resonance absorption dip are dipper than the low O_2 pressure films [see Fig.4.4 (A)].

Fig. 4.4 (B) demonstrates the resonance field as a function of frequency for all the samples at polar angle 0° and 90°. It is clear that for 90° orientation large magnetic field (greater than saturation magnetization) is required to drag the magnetic moments from easy in-plane direction to out-of-plane direction. Hence, the preferential direction of magnetic moments in our epitaxial YIG films are along the film plane. Fig. 4.4 (C) shows the field linewidth as a function of frequency for YIG thin film with pressure 0.15 mbar. The Gilbert damping (α) parameters were estimated from the fitting of the phenomenological equation [205]

$$\Delta H = \Delta H_0 + \frac{4\pi\alpha}{\gamma} f \tag{3.6}$$

We observed that the Gilbert damping constant decreases with the increase of O_2 pressure. The lowest Gilbert damping constant of 4.37×10^{-5} was observed for highest oxygen pressure 0.15 mbar grown film as compared to 3.55×10^{-4} for 0.0025 mbar oxygen pressure grown sample. Such a low Gilbert damping is a novel observation in our perfect-grown epitaxial YIG films. Hence, these low damping YIG films grown at higher O_2 pressure are very good and promising candidate for many spintronic applications, viz. magnetic memory, sensor and microwave narrow-band filters, etc.

ΔH_0 is another important parameter which represents the frequency independent ($f = 0$) contribution to the linewidth produced by inhomogeneous broadening, which is also called as extrinsic contribution to sample linewidth. Lower is the value of ΔH_0, lesser is the spin wave scattering at the film-substrate interface and/or in the bulk of the film, which arises due to increased inhomogeneities [206, 207]. We have observed the lowest ΔH_0 of 13.3

Oe for the 0.15 mbar oxygen pressure YIG sample. This is also a conclusive evidence to justify that the higher oxygen pressure grown YIG thin films are the best epitaxial films among the four YIG films grown at different O_2 pressure in this investigation.

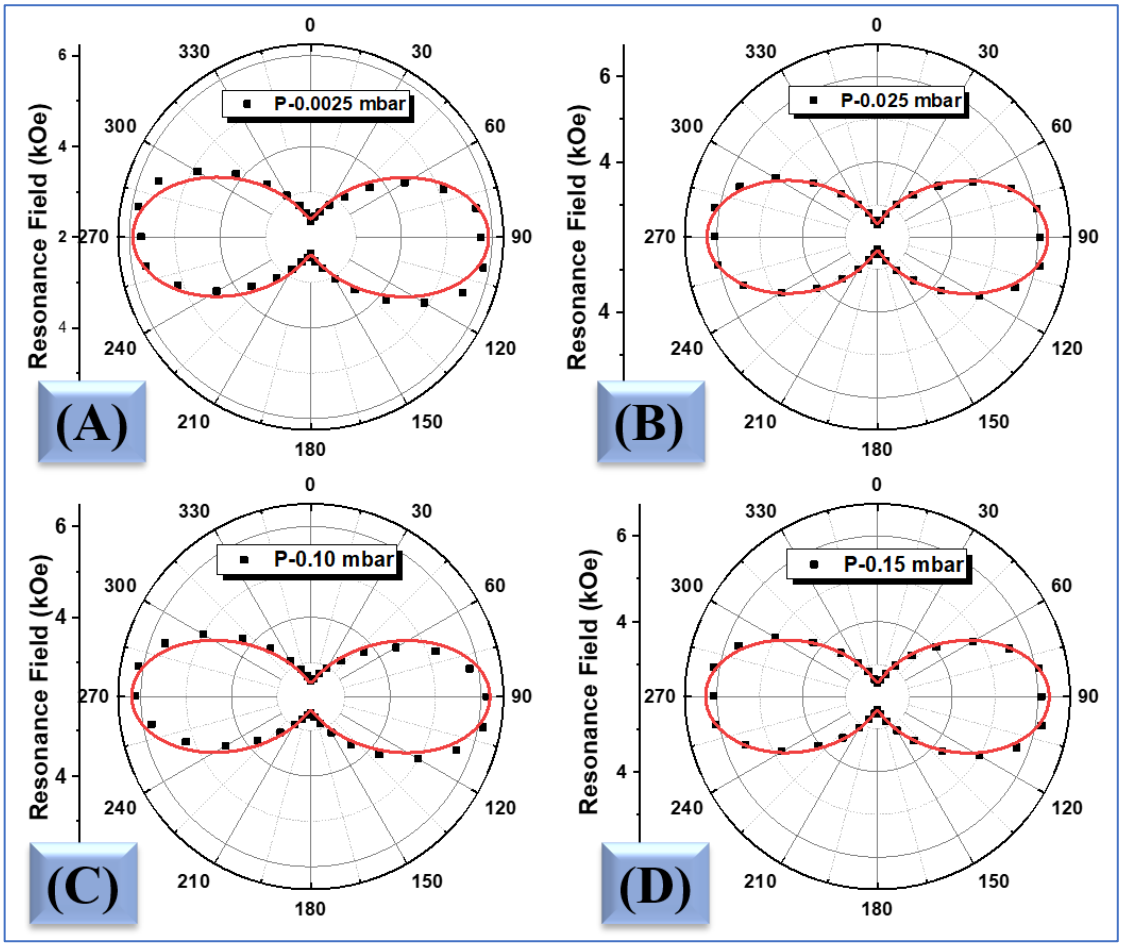

Fig. 3.5: (A-D) θ_H-variation (out-of-plane angular dependence) of the resonance fields for all oxygen pressure samples, solid line corresponds to fitting using Eq. (3.4).

The out-of-plane (θ-variation) angular dependent resonance field for all four YIG films are shown in Fig. 3.5 (A-D). For a better understanding of easy and hard axis along with anisotropy orientation graphs are shown in polar plots. A minimum in the resonance field indicates an easy axis of magnetization. We can see that the overall easy-axis of

magnetization is along the in-plane direction. There are maxima of resonance fields at normal to sample plane directions. A maximum along normal direction confirms magnetization hard axis. In Fig. 3.5 solid squares are the experimental data points and the solid lines in each plot correspond to the best theoretical fit of the experimental data using Eq. (3.4) as mentioned above. The fitted parameters such as saturation magnetization, gyromagnetic ratio, $H_{2\perp}$ and $H_{4\perp}$ are tabulated in table 3.3. It is observed that the saturation magnetization approaches near the bulk value of YIG as the oxygen gas pressure is increased above 0.10 mbar.

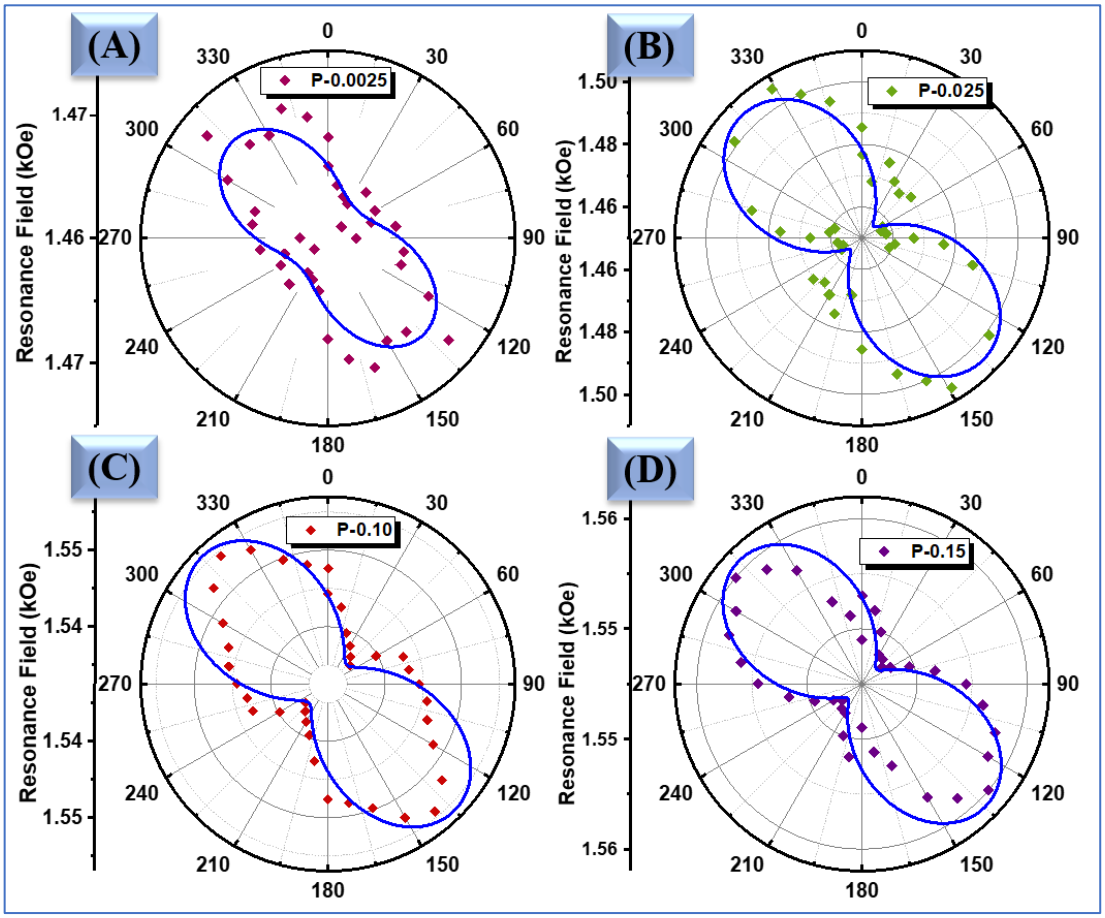

Fig. 3.6 (A-D): In-plane angular dependence of the FMR field. The symbols correspond to the experimental data whereas solid lines represent the numerical fits obtained from Eq. (3.5).

Further, the out-of-plane uniaxial anisotropy ($H_{2\perp}$) decreases whereas in-plane cubic anisotropy ($H_{4\perp}$) increases with oxygen pressure increment. This indicates that the easy axis of YIG films is in the (111) direction which is in good agreement with earlier reported works [201, 208]. The origin of strong anisotropy contribution can be caused by a combination of shape, surface and magnetoelastic anisotropy [87].

Fig. 3.6 (A-D) shows the in-plane angular dependence of FMR resonance fields.

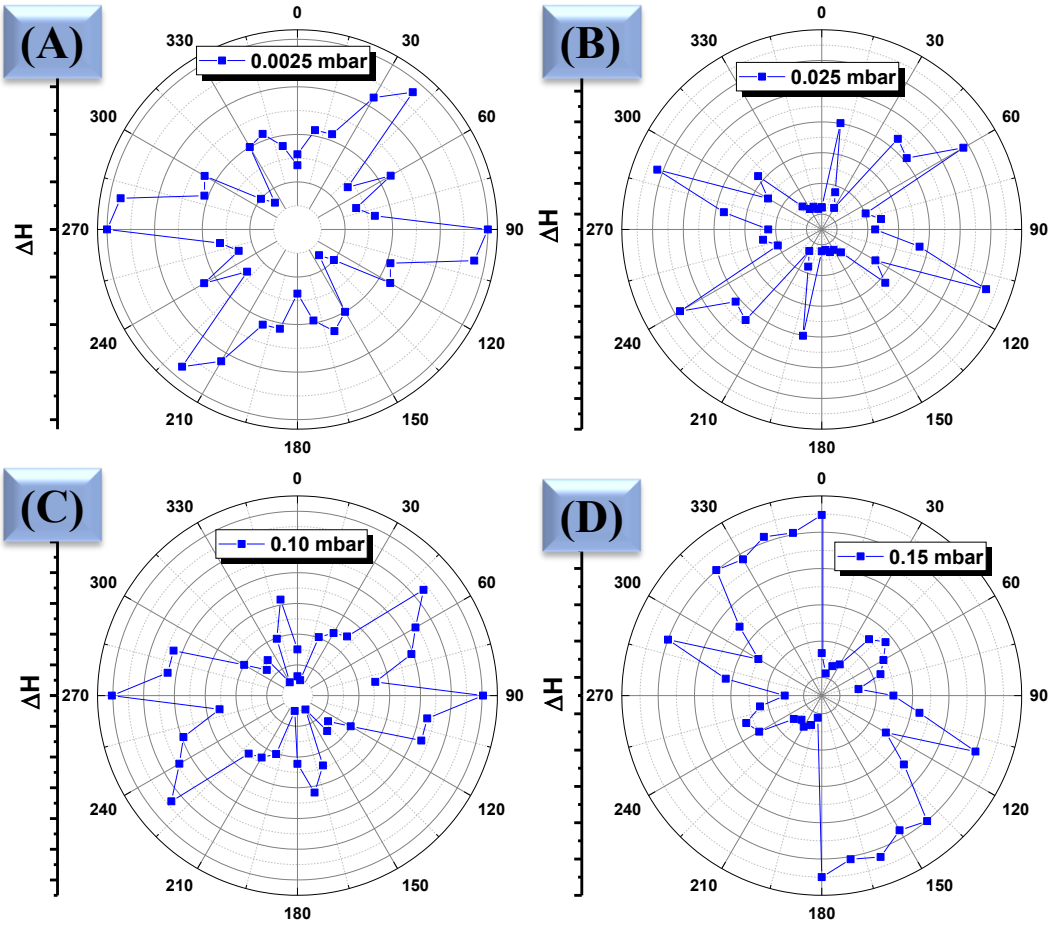

Fig. 3.7(A-D): In-plane angular dependent field linewidth for all oxygen gas pressure variation samples

A close examination of the polar plots of out-of-plane FMR resonance fields data and in-plane FMR resonance fields indicate that the YIG thin films are preferentially oriented

along the easy-axis direction. In Fig. 3.6 the solid lines are derived from the fitting of Eq. (3.5) assuming $\theta = \theta_H = 90°$ and $\varphi = \varphi_H$. For fitting of the in-plane resonance field data, the saturation magnetization was kept the values derived from θ-variation.

The in-plane two-fold symmetry is observed for resonance field which indicates contribution from uniaxial and cubic anisotropy. The generation of in-plane uniaxial anisotropy can be explained by the influence of surface inhomogeneities due to variation of oxygen pressure [209]. The derived parameters revealed that the contribution of in-plane uniaxial anisotropy and cubic anisotropy increases with oxygen gas pressure increment. The in-plane uniaxial anisotropy ($H_{2\parallel}$) is maximum for 0.10 mbar oxygen pressure film to be around 0.7 Oe and cubic anisotropy ($H_{4\parallel}$) around 10 Oe. The out-of-plane uniaxial anisotropy ($H_{2\perp}$) is observed to be around – 11.02 kOe, the negative sign indicates that the anisotropy contribution favors in-plane alignment of the magnetization. The derived parameters for all the samples are tabulated in table 3.3.

The in-plane angular dependent field linewidths are shown in Fig. 3.7 (A-D). The measurements reveal a dominating six-fold symmetry in the plane of (111)-oriented YIG thin films. One might attribute this to the combination of uniaxial anisotropy and magneto-crystalline cubic anisotropy observed in FMR linewidth. This is expected as a contribution from the miscut of the substrate. These results match with the in-plane angular variation of coercive field [209, 210]. The minimum ΔH was observed to be around 9 Oe for 0.15 mbar sample which further confirmed that we have achieved best epitaxial films for highest oxygen pressure.

Therefore, it is important to understand the effect of deposition parameters mainly oxygen pressure on various magnetic anisotropies of ultra-thin epitaxial YIG films for spintronic device applications.

Table 3.3: Parameters obtained from FMR

Oxygen Pressure (mbar)	θ Variation Parameters				φ Variation Parameters	
	M_s (kOe)	$H_{2\perp}$ (kOe)	$H_{4\perp}$ (kOe)	γ' (GHz/kOe)	$H_{2\parallel}$ (Oe)	$H_{4\parallel}$ (Oe)
0.0025	1.586	-0.384	0.723	3.21	0.63	3.83
0.025	1.689	-0.367	0.739	2.93	0.92	25.0
0.10	1.720	-0.228	0.760	2.70	0.70	10.0
0.15	1.860	-0.187	0.798	2.75	0.51	7.00

3.3.3 Micromagnetic calculation:

In this section, we have described the micromagnetic simulation which is essentially used to demonstrate the relationship between microstructure and magnetic properties of materials [211]. The purpose of this calculation is to show how on the basis of the Landau-Lifshitz-Gilbert formalism of micromagnetic simulations, modes of magnetic films can be identified in the presence of magneto-crystalline interaction and dipolar fields. In numerical simulations, we have considered a rectangular sample measuring 10×10 nm^2 cells. The material parameters used are: exchange constant (A) = 0.47×10^{-6} erg/cm for YIG, gyromagnetic ratio ($\gamma'=\gamma/2\pi$) = 2.93 GHz/kOe. We have provided saturation magnetization, anisotropy parameters and Gilbert damping obtained from experimental FMR studies on the four YIG samples under investigation.

A two-dimensional configuration (Y-Z plane) is put out in a convenient form to show the magnetization orientation in the cell. This is shown in part (A) of Fig. 8. At this point, the microwave field turned on and the program start to generate data of microwave energy absorbed by the sample at each magnetic field values. The FMR absorption versus frequency data are found in part (B) of Fig. 8. The dynamic spectrum generates the main

'FMR mode' as shown in part (C) of Fig. 3.8. The investigated system shows resonant peak associated with the "bulk" or the main FMR mode.

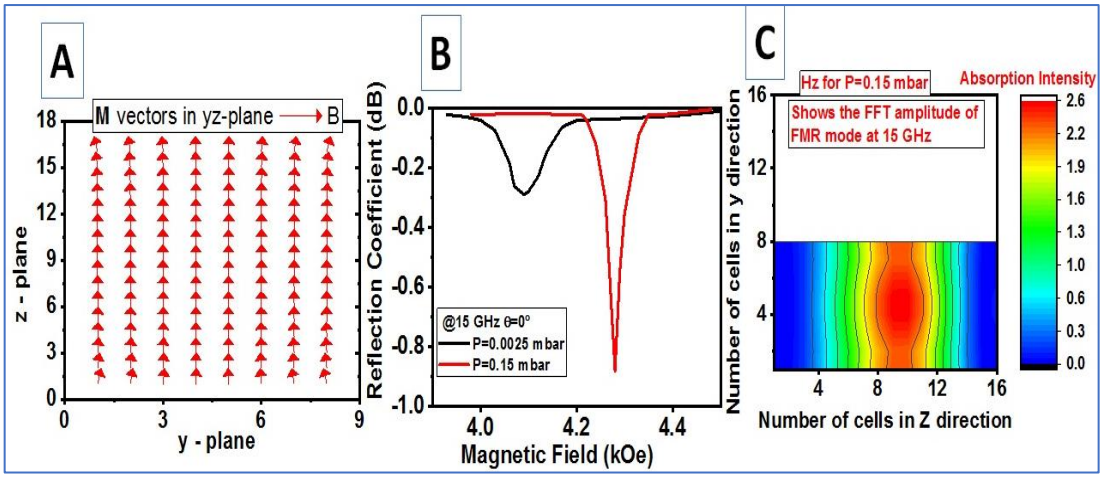

Figure 3.8: (A) Demonstrates magnetic moments at equilibrium configuration in a cell of $10 \times 10\, nm^2$ size of YIG film grown at 0.15 mbar oxygen pressure. (B) Field-swept modes at 15 GHz in two YIG thin films, one at lowest Oxygen pressure (0.0025 mbar) and the second at highest oxygen pressure (0.15 mbar). (C) Spectrum of main FMR mode of YIG film grown at 0.15 mbar oxygen pressure. The highest absorption levels are depicted as red and the lowest levels is blue, as shown in FFT amplitude and the bar graph.

It is to be pointed out that in two YIG films, high intensity peak corresponds to the main FMR resonant modes. The spectra are different in the sense that lowest oxygen pressure grown film has broader linewidth and appear at a lower magnetic field value. Whereas, for the highest oxygen pressure grown YIG film has much intense FMR peak with a much narrower linewidth arises due better microstructure and magnetic properties.

3.4 Conclusions

We have reported the structural, magnetic and microwave properties of pulsed laser deposited epitaxial YIG thin films on GGG(111) substrates by varying the oxygen gas pressure. All experimental observations indicate that the oxygen pressure variation during growth significantly influence the uniformity and crystallinity of YIG films. The saturation magnetization was enhanced by a factor of 17% for highest oxygen pressure

(0.15 mbar) grown film. We have observed very low coercivity for all samples. Angular dependent FMR spectra of epitaxial YIG (111) thin films for in-plane and out-of-plane geometries indicate that the perfect single crystal growth of YIG can be done at 0.15 mbar O_2 pressure. By comparing the FMR data to a theoretical model based on the Liftshitz-Landau formalism we determined various parameters such as saturation magnetization, gyromagnetic ratio, uniaxial and magneto-crystalline anisotropy and Gilbert damping constant. The in-plane cubic magneto-crystalline anisotropy is found to be more as compared to uniaxial anisotropy for high oxygen pressure samples. All the observed parameters clearly indicate that YIG films grown at higher oxygen pressure (>0.1 mbar) have perfect epitaxial growth in comparison to YIG films grown at lower O_2 pressure. It is also observed that low damping constant is achievable at high oxygen gas pressure grown YIG films which makes these films suitable for spintronics applications, for example narrow band filters. The micromagnetic simulations using Landau-Lifshitz-Gilbert formalism provide microstructure and magnetic properties dependent magnetization dynamics, FMR mode positions and linewidth of different oxygen pressure grown YIG films.

Chapter 4

Reciprocal and non-reciprocal electromagnetic wave propagation in sub-100 nm epitaxial YIG thin films deposited under different oxygen growth pressure

Directional dependent transport of information in magnetic thin films offers a great opportunity to realize reciprocal and nonreciprocal microwave devices, such as filters, phase shifter, isolators and circulators. Electromagnetic wave (EM) propagation in sub-100 nm thin magnetic film is critical, yet reciprocal and non-reciprocal wave propagation and its accurate measurements remain a challenge. We investigated reciprocal and non-reciprocal wave propagation in 90 nm thick epitaxial thin films of yttrium iron garnet ($Y_3Fe_5O_{12}$: YIG) grown by pulse laser deposition (PLD) technique on gadolinium gallium garnet [GGG (100)] substrates. The effect of oxygen growth pressure during deposition of YIG films exhibit directional dependence properties of electromagnetic wave propagation. The reciprocal EM wave propagation was generated by a S-type transmission line to achieve microwave (RF) magnetic fields ($\boldsymbol{h_{RF}}$) perpendicular to applied dc magnetic fields ($\boldsymbol{H_{DC}}$), to ensure the ferromagnetic resonance (FMR) condition. The center frequency is tuned up to 20 GHz with an applied magnetic field of 6 KOe. The tuning of the center frequency was achieved as of 85.3% with H_{DC} of 6 KOe. To achieve non-reciprocal EM-wave propagation one straight microstrip line was used to ensures a parallel configuration (parallel pumping FMR condition) of $\boldsymbol{h_{RF}}$ to $\boldsymbol{H_{DC}}$. The nonreciprocity observed is due to the presence of gyrotropic properties in the YIG thin films and it enhances when YIG film was placed in asymmetric geometry. Further, oxygen growth pressure (> 0.1 mbar) grown YIG films enhances the nonreciprocity by 21.6%. The experimental results were successfully validated using high-frequency structure simulator (HFSS). Hence, these results indicate that controlled deposition parameters can

be a crucial parameter in the design of reciprocal and nonreciprocal microwave signal processing devices.

4.1 Introduction

Microwave devices which can be primarily categorized into reciprocal and non-reciprocal devices are extensively used in microwave front-ends communication systems. These includes filters, power splitters, couplers, phase shifters, isolators, circulators, gyrators, microwave amplifiers, etc. [212-216]. Systems that require EM-wave propagation in one direction and significant attenuation in the opposite direction employ nonreciprocal devices. Microwave isolators' unidirectional characteristics are important for shielding the output of load-sensitive devices from undesirable reflections. An isolator, for instance, can be added to an oscillator's output to prevent load-pulling. Thus, in an isolator, for example, propagation in a "forward" direction can be allowed but propagation in the "reverse" direction is blocked. They improve stability, performance, and reliability of microwave systems. In addition, certain applications, e.g. one-port-amplifiers, cannot be realized at all without the use of circulators or isolators. In principle, nonreciprocal devices can be built without any magnetic materials using semiconductor operational amplifiers. However, the drawbacks of this “semiconductor” approach are that such devices are active, which require energy for their operation, can operate only at relatively low frequencies (typically below 1 GHz), and operate only at low power, not exceeding 1 mW.

Another convenient way to realize nonreciprocal devices is to exploit the gyrotropic properties of magnetic materials, like ferrites. In terms of bandwidth, power, and excellent isolation performance, none of the above technologies can compete with ferrite-based solutions. The nonreciprocity can be developed mainly in specific anisotropic media such as magnetic materials which on interaction with the magnetic component of the electromagnetic waves [217-219]. The non-reciprocity arises only due to the time-reversal and spatial symmetry breaking in magnetic materials due to its gyrotropic nature. At high frequencies, the propagation in a planar structure is no longer be transverse

electromagnetic (TEM), as there may be an appearance of longitudinal component of the microwave magnetic field. When a circularly polarized electromagnetic wave penetrates into a magnetic material which is magnetized with the application of a dc magnetic field applied perpendicular to the direction of propagation of EM-wave can be absorbed differently ($S_{21} \neq S_{12}$). Thus, the resulting elliptically polarized microwave magnetic field in the asymmetrically placed magnetic material on one side of the signal line over the dielectric can result in nonreciprocal operations. A resonant isolator can be fabricated by attaching ferrite films at the air–dielectric interface between the conductors. This effect is maximum at the gyromagnetic resonance frequency of the ferrite [220-223]. Although, ferrite isolators provide higher performance, only a few types provide frequency tunability. The final adjustable planar waveguide design employs a non-magnetic substrate with a ferrite film. Loaded waveguide devices are difficult to manufacture, and the positioning of the ferrite can considerably affect the design's performance. Magnetic moments of a ferromagnetic material precesses with an operating frequency at around their mean position in the presence of an external magnetic field.

Uniform precession of spins with zero wave-vector ($\boldsymbol{k} = 0$) results in ferromagnetic resonance whereas spin waves propagation is due to non-zero wave-vector ($\boldsymbol{k} \neq 0$), known as magnons [47, 224-228]. Perpendicular ($\boldsymbol{h_{RF}} \perp \boldsymbol{H_{DC}}$) and parallel ($\boldsymbol{h_{RF}} \parallel \boldsymbol{H_{DC}}$) pumping ferromagnetic resonances, birefringence, rotation of the plane of polarization and many more phenomena can be seen with the propagation of electromagnetic waves in anisotropic magnetic materials. These phenomena are essential to engineer the contemporary microwave devices. Further, conventional ferrite-based microwave devices are several centimeters in size and hence occupy large space and are disadvantageous for on-chip fabrication of microwave devices and hence provide limitation when scaling with semiconductor-based systems are required. This opens up exploration of new opportunities to design on-chip devices which will be few orders of magnitude smaller than conventional microwave ferrite devices. With the advancement of thin films deposition process, the fabrication of good quality thin films with epitaxial growth is

possible [186, 229-230]. Specifically, yttrium iron garnet (YIG) thin films have attracted a lot of interest due to its extremely low damping and long propagation distance for spin waves [21, 231-232].

Various deposition techniques were used for the growth of high-quality single crystal YIG thin films on gadolinium gallium garnet (GGG) substrates such as molecular beam epitaxy (MBE), liquid phase epitaxy (LPE), magnetron sputtering and pulsed laser deposition (PLD) [185, 233-235]. It is also apparent that there is significant room for improvements in the film quality by varying the growth parameters. Recently, we reported the effect of oxygen growth pressure on the magnetization dynamics of epitaxial YIG thin films grown on GGG substrates developed by PLD technique [229]. However, the effect of growth condition, especially oxygen growth pressure on the reciprocal and non-reciprocal EM wave propagation in sub-100 nm epitaxial YIG thin films are rarely investigated. This will allow us to optimize the growth conditions to achieve the best magnetic properties of our YIG films. Specifically, we will seek growth conditions which will give us the maximum value of the in-plane anisotropy (H_k), proper value of the saturation magnetization (M_s), high squareness of the hysteresis loop, and the lowest possible value of the FMR linewidth at high frequencies. These effects can be utilized in the fabrication of monolithic microwave signal processing devices such as planar (on-chip) isolators and planar notch filters, which are still not well-studied. Moreover, magnetostatic modes can be excited in YIG thin films using double antenna structure due to the large effect of magnetic medium on the current distribution and radiated power [57-59]. This can lead to devices such as spin-wave filters and isolators which have great potential in applications of novel compact and low-cost reconfigurable microwave devices.

In the present study, we utilized S-type microstrip line for electromagnetic wave propagation with $\boldsymbol{h_{RF}} \perp \boldsymbol{H_{DC}}$ in YIG thin films (flipped on center conductor) to demonstrate the reciprocal propagation through FMR effect. We have also demonstrated

by using a straight microstrip line with $\boldsymbol{h_{RF}} \parallel \boldsymbol{H_{DC}}$ for non-reciprocal EM-wave propagation in parallel configuration in YIG thin films. This experiment was performed in flip-chip geometry, i.e., with YIG film flipped asymmetrically to demonstrate specifically the non-reciprocal propagation of EM waves. Additionally, the influence of different oxygen gas pressure during thin film growth have been investigated on the nonreciprocal wave propagation. A strong theoretical component is a key element in the reciprocal and non-reciprocal device design, and to closely coordinate with the experimental work. We have numerically modelled using full-wave simulations of the isolator structures using software packages of Ansoft HFSS. The full-wave modeling capability represents an important bridge between the theoretical work and the experimental results obtained. The dispersion relation of the reciprocal and non-reciprocal wave propagation is thoroughly studied in YIG thin films.

4.2 Experiment part

The epitaxial YIG films of thickness ~ 90 nm were grown on GGG substrates using PLD technique. We prepared a YIG target (diameter: 1 in) for the fabrication of YIG thin films using yttrium oxide (Sigma – Y2O3, 99.99% pure) and iron oxide (Sigma – Fe2O3, 99.99% pure) powders synthesized via a conventional solid-state reaction procedure. The YIG thin films were deposited using the pulsed laser deposition (PLD) method onto single crystalline GGG (111) substrates supplied by MTI Corporation in Richmond, USA. The substrates and the vacuum chamber were meticulously cleansed prior to deposition. The PLD system is comprised of a 248 nm-wavelength KrF excimer laser. We ablated the target at a 300 mJ energy level with a pulse repetition frequency of 10 Hz in order to produce YIG thin coatings of superior quality. Substrate separation from the target was maintained at 4 cm. Through the utilization of a turbo molecular pump, the background base pressure was preserved at $1x10^{-6}$ mbar. Substrate preheating at 800 °C eliminated any impurities from the top layer. The deposition process involved subjecting the films to growth at four distinct oxygen pressures: 0.0025 mbar, 0.025 mbar, 0.10 mbar, and 0.15

mbar, with the growth temperature maintained at 800 °C. The rate of film growth was approximately 0.5 Ω/s. A consistent quantity of 15,000 shots was utilized to deposit film at every oxygen pressure. Throughout the procedure, as-grown thin films were annealed in situ at 800 °C for two hours before being cooled to room temperature in the presence of oxygen [229]. The dimensions of the YIG thin films that are deposited are of 2.5 mm by 5 mm. The investigation of the thin films' structural properties was conducted utilizing X-ray diffraction (XRD) with a Miniflex Rigaku diffractometer and Cu Kα radiation (λ=1.5406Ω). Using a physical properties measurement instrument (PPMS – Cryogenics Limited (Model – J103), UK) with a magnetic field applied along the in-plane geometry of the film, DC magnetic measurements were obtained. Using a broadband vector network analyzer (PNA N5224A) and a microstrip line geometry-based spectrometer, the microwave measurements (for both perpendicular and parallel pumping configurations) were performed.

Two different microstrip lines were used to measure stop-band filter and isolator response of EM-wave propagations. A straight-type microstrip line was used to investigate non-reciprocal transmission ($S_{12} \neq S_{21}$) of EM-waves to demonstrate the isolation characteristics in the YIG films (Fig. 4.1 (A)) in parallel pumping geometry between $\boldsymbol{h_{RF}}$ and $\boldsymbol{H_{DC}}$. Microwave waveguide or other transmission systems (in our case a microstrip line) of a finite width 'w' will excite a packet of collective spin waves having wavevectors in the interval $|k| < 1/w$. On the other hand, one S-type microstrip line was used for stop-band filter measurements in perpendicular geometry to analyze the reciprocity ($S_{12} = S_{21}$) effects (Fig. 4.1 (B)) EM-waves propagation which satisfy the FMR condition. Both straight-type and S-type microstrip lines were fabricated on Rogers RO4350B™ Laminates dielectric substrate with $\varepsilon_r = 3.48$. In our designed microstrip line the signal line width ('w') was 38.4 μm to maintain matching impedance of 50 Ohms to match the source impedance. As shown in Fig. 4.1(A), for asymmetric condition the YIG/GGG thin films was flipped on the microstrip line with YIG surface touching the center conductor

of the transmission line. The microwave signal in the frequency range of 3 – 20 GHz was applied to the microstrip line at a constant external magnetic field. To demonstrate the tuning of the reciprocal and non-reciprocal behavior external magnetic field was varied from 0 to 6 KOe. Before the sample characterization, the microstrip lines were properly calibrated using Through-Reflection-Load (TRL) calibration method. The transmission coefficients (S_{12} and S_{21}) as a function of frequency at different external magnetic fields were recorded.

Measurements were performed in the frequency sweep mode to determine the resonant frequencies and their line-widths/band-widths. We have defined the measure of non-reciprocity (isolation) as the difference between forward (S_{21}) and the reverse (S_{12}) transmission of EM-waves in dB. Other, YIG film parameters such as saturation magnetization, gyromagnetic ratio, Gilbert damping, were determined from resonance frequency and frequency line-width by analytical fitting of transmission (S parameters) data.

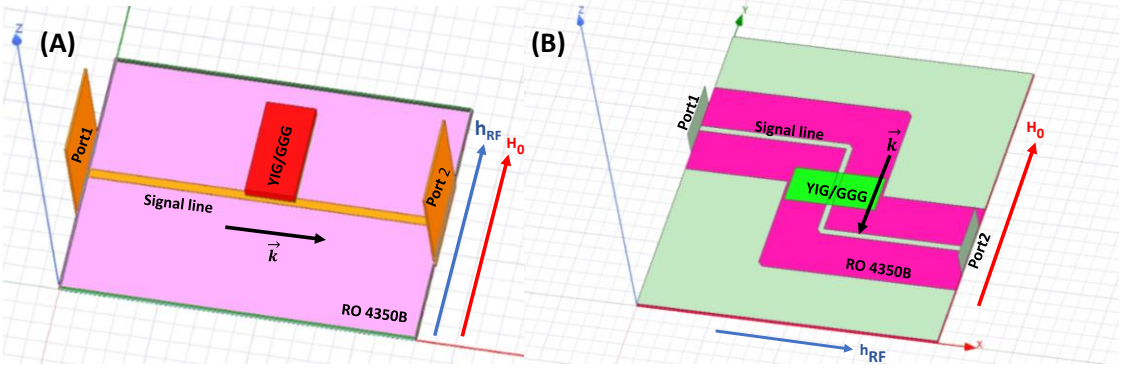

Fig. 4.1. (A) Structure for the EM-wave propagation for non-reciprocal isolation on straight-type microstrip line in asymmetric geometry. (B) Structure for the reciprocal EM-wave propagation by the S-type microstrip transmission line which satisfy FMR condition.

4.3 Results and discussion

4.3.1 Structural and magnetic characterization:

Fig. 4.2 (A) demonstrates the XRD pattern of YIG thin films deposited at different oxygen growth pressure. The deposited films exhibited the characteristic of being single-crystalline over the GGG (111) substrate. The limited area was subjected to many scans in order to conduct a comprehensive analysis of the YIG peak. In Fig. 4.1 (A), the deposited YIG films showed the signature of single crystallinity over GGG (111) substrate. The pattern confirms that only (111) oriented reflection family peaks exist in YIG and there is no indication of any additional phase. We observe that the lattice constant of YIG films increases from 12.379 Å to 12.458 Å as the oxygen pressure rises from 0.0025 mbar to 0.15 mbar. The elevation of oxygen growth pressure leads to thermal expansion between the film and substrate further contributes to the enlargement of the lattice constant [194]. Fig. 4.2(B) displays the M-H curve of YIG thin films, with the oxygen gas pressure being the variable. A linear function was used to remove the contribution of the paramagnetic behavior of the GGG substrate from the raw data collected from VSM. The saturation magnetization of YIG films at increased oxygen pressure approached to that of the bulk value of YIG. The coercivity remains rather stable at around 12 ± 2 Oe for all samples subjected to varying oxygen pressure. The YIG films exhibit exceptional soft magnetic properties as a result of their low coercivity values. The low coercivity values correspond to a magnetic homogeneity in YIG thin films [199]. Fig. 4.3 (C) shows the FMR resonance fields as a function of out-of-plane angular variation for all the investigated samples. Resonance field values measured from in-plane to out-of-plane rotation of the film with respect to dc magnetic field are plotted and the are fitted to Landau-Lifshitz-Gilbert equation to obtain various dynamic parameters. The detailed magnetic parameters of the deposited films are shown in table 4.1.

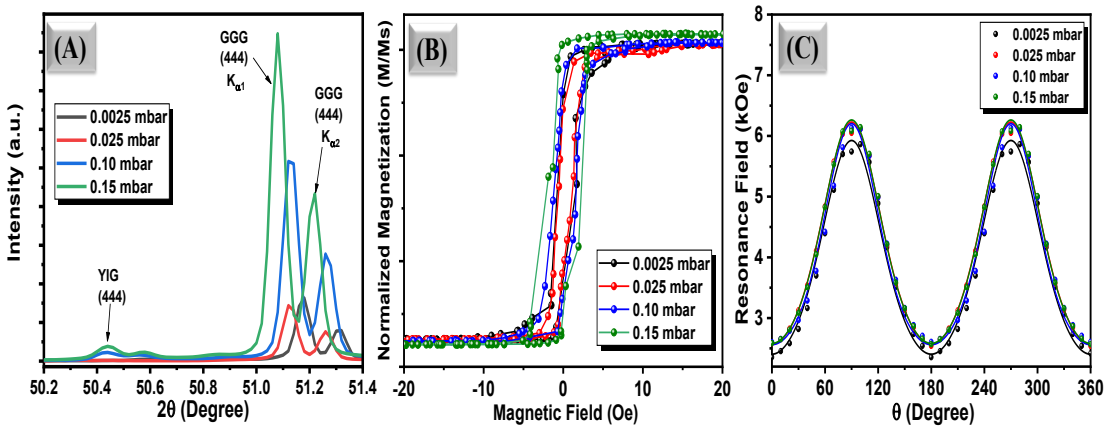

Fig. 4.2. (A) The XRD spectra of YIG thin films on GGG substrate at different oxygen pressure (B) magnetic hysteresis loop of all the samples for different oxygen pressure, (C) resonance field as a function of out-of-plane angular variation of all the samples for different oxygen pressure. The solid line represents fitting of experimental data to LLG equation.

Table 4.1: Experimentally observed static and dynamic magnetic parameters of all the samples.

Oxygen Pressure (mbar)	**M_s (kOe)**	**γ' (GHz/kOe)**	**Gilbert damping**	**Anisotropy Field (kOe)**
0.0025	1.586	3.21	3.55×10^{-4}	0.28
0.025	1.689	2.93	3.4×10^{-4}	0.30
0.10	1.720	2.70	1.58×10^{-5}	0.32
0.15	1.860	2.75	4.37×10^{-5}	0.36

4.3.2 Microwave simulation:

ANSYS HFSS software was used to perform high frequency electromagnetic field simulations. The principal technique is a specific accurate finite element method (FEM) that implements a frequency domain EM full-wave analysis of the structure under study. We have used Maxwell solver to derive fundamental mode of FMR. We have performed theoretical calculations for the reciprocal and non-reciprocal propagating EM waves by using same parameters of the substrate as used in experiment. We have designed both S-type microstrip line and straight microstrip line on the Rogers: 4350B, $\varepsilon_r = 3.48$ substrate with width of the signal line 38.4 μm. The thickness of YIG film, micro-strip copper line and dielectric substrate are 90 nm, 16 μm and 168 μm respectively. The number of grid cells corresponding to YIG film, microstrip line and dielectric substrate are 1865, 4400, and 47676, respectively. The YIG thin films were flipped on the signal line to observe the absorption of EM wave propagation. Anisotropic and frequency-dispersive permittivity and permeability tensors are used in the software, so that the effect of conducting or non-conducting resonant magnetic layers can be studied and optimized. The microstrip line loaded with YIG thin films were simulated by applying appropriate boundary conditions. To consider the role of oxygen growth pressure the magnetic parameter such as saturation magnetization, linewidths were varied during simulation. Two wave ports, port 1 and port 2 were defined as the source of microwaves. Wave ports assignment, applied boundary conditions and simulation strategies are shown in Fig. 4.1. "Driven Modal" was chosen as a solution type and a frequency sweep in the range of 1 – 20 GHz was varied. DC magnetic bias ($\vec{\boldsymbol{H}}_{\boldsymbol{0}}$) was applied to the YIG thin films (90 nm) in perpendicular direction to the rf magnetic field ($\vec{\boldsymbol{h}}_{\boldsymbol{RF}}$) to satisfy the FMR condition; $\vec{\boldsymbol{h}}_{\boldsymbol{RF}} \perp \vec{\boldsymbol{H}}_{\boldsymbol{0}}$ as shown in Fig. 4.1 (B). Non-reciprocity of wave transmission spectra was simulated on straight microstrip line as shown in Fig. 4.1 (A) with the magnetic bias ($\vec{\boldsymbol{h}}_{\boldsymbol{RF}} \parallel \vec{\boldsymbol{H}}_{\boldsymbol{0}}$) perpendicular to EM-wave propagation direction and with YIG thin film flipped in asymmetrical position. To observe the non-reciprocity in simulated results, the thickness of the YIG films was taken 90 nm

39

and external magnetic field was varied as an external excitation to YIG thin films to tune the device operating frequency.

To obtain a non-reciprocal EM-wave propagation, the final adjustable planar waveguide design employs a non-magnetic RT/duroid® laminates with a YIG thin film loaded device. The positioning of the YIG thin film can considerably affect the design's performance.

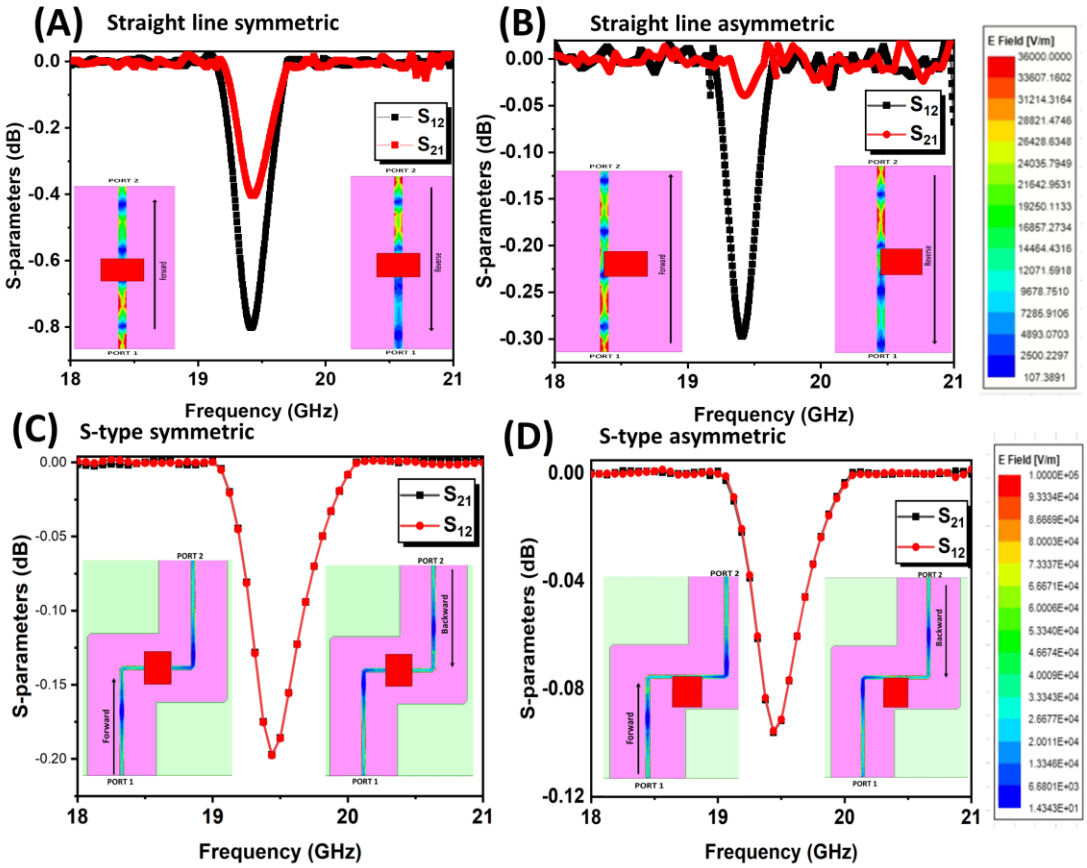

Fig. 4.3: HFSS simulated plots for (A) straight microstrip line with symmetrical positioning (B) straight microstrip line with asymmetrical positioning (C) S-type microstrip line with symmetrical positioning and (D) S-type microstrip line with asymmetrical positioning of the sample. (Insets: HFSS simulated E-field response for each microstrip line and sample positioning).

Fig. 4.3 (A-D) demonstrates the HFSS simulated response of transmission parameters as well as the electric (***E***) field strength (right most color matrix) for a two-port microstrip line. Fig. 4.3 (A) and (C) show when the sample is placed symmetrically on a straight microstrip line. Similarly, Fig. 4.3 (B) and (D) demonstrate asymmetric positioned YIG film on straight as well as "S" type waveguide, respectively. Fig. 4.3 (A) and (B) demonstrate the non-reciprocal EM-wave propagation both for symmetric and asymmetric case. Similarly, Fig. 4.3 (C) and (D) demonstrate absorption of EM-wave for reciprocal propagation on a "S" type waveguide. We observe that for a straight microstrip line, the symmetric position (Fig. 4.3 (A)) results less nonreciprocity whereas for asymmetric position (Fig. 4.3 (B)) proper unidirectional transmission results giving rise to large isolation. On the contrary, for a "S" type microstrip line, both for symmetric as well as for asymmetric position of YIG (Fig. 4.3 (C) and 3 (D)) EM-wave propagation is reciprocal. For all simulations an external magnetic field of 6 KOe was applied. It is clearly demonstrated from the Fig. 4.3(A-B) that the non-reciprocity enhances when the sample is placed in asymmetrical position as compared to symmetrical position.

High frequency microwave excitation was carried out to investigate the signal propagation in the non-reciprocal microwave devices. In this case, M held perpendicular to the direction of EM propagation but parallel to the $\boldsymbol{h_{RF}}$ component of EM waves. The propagation vectors + $\boldsymbol{k_{em}}$ and – $\boldsymbol{k_{em}}$ represents for forward and reverse propagation of EM waves [238]. For the simple transmission line, the propagation vector ($\boldsymbol{k_{em}}$) is obtained from the following relation,

$$\boldsymbol{k_{em}} = \sqrt{\varepsilon \mu_m \frac{\omega^2}{c}} \tag{4.1}$$

The difference between the forward EM wave amplitude (S_{21}) and the reverse amplitude (S_{12}) represent the non-reciprocity or isolation and can be written as,

$$\text{Isolation} = (S_{21} - S_{12}) \tag{4.2}$$

Tunable isolation was achieved by considering the magnitude of the transmission line for these geometries [236]. Magnetic materials which exhibit anisotropy when loaded

asymmetrically on the microstrip line enhances the non-reciprocity and also violates the Lorentz reciprocity resulting in asymmetric polder tensor of permeability [220, 236-244].

4.3.3 Microwave measurements:

High frequency microwave excitation was carried out to investigate the signal propagation in the reciprocal microwave devices. Tunable band-stop filter can be achieved by considering the magnitude of the transmission line for these geometries [245], whereas it can be used as a phase shifter due to the delay in transmission phase along the length of the line [37]. Fig. 4.4 (A) shows the frequency-swept FMR spectra of 0.15 mbar oxygen pressure YIG film when electromagnetic wave was propagating from port 1 to 2 (S_{21}) as a function of frequency and with external magnetic field applied along film's in-plane direction. It is to be mentioned here that we have observed EM-wave propagation through YIG film from port 1 to 2 (S_{21}) and port 2 to 1 (S_{12}) to be exactly identical which demonstrate the reciprocal nature of the band-stop filters. Similar results were achieved in HFSS simulation as shown in Fig. 4.4 (C-D). It is observed that the magnitude of EM-wave power absorption increases at higher frequencies at the resonance dip.

The resonance frequency and frequency linewidths for each field were determined from the Lorentzian fitting of the spectra. We have defined the frequency tunability as the ratio of change in filter frequency with bias magnetic field ($\boldsymbol{H_{DC}} > 0$) to the frequency at zero magnetic field ($\boldsymbol{H_{DC}} = 0$) [37, 245-246]. The band-stop frequency was tuned from 3 GHz to 20 GHz when external magnetic field increased from 0.3 to 6 KOe. Hence, a frequency tunability of band-stop filter with 90 nm YIG film as active element is observed to be ~ 85.3% in the present investigation. Frequency-swept FMR spectra and frequency tunability of three other YIG films (grown at lower oxygen gas pressure) were also achieved.

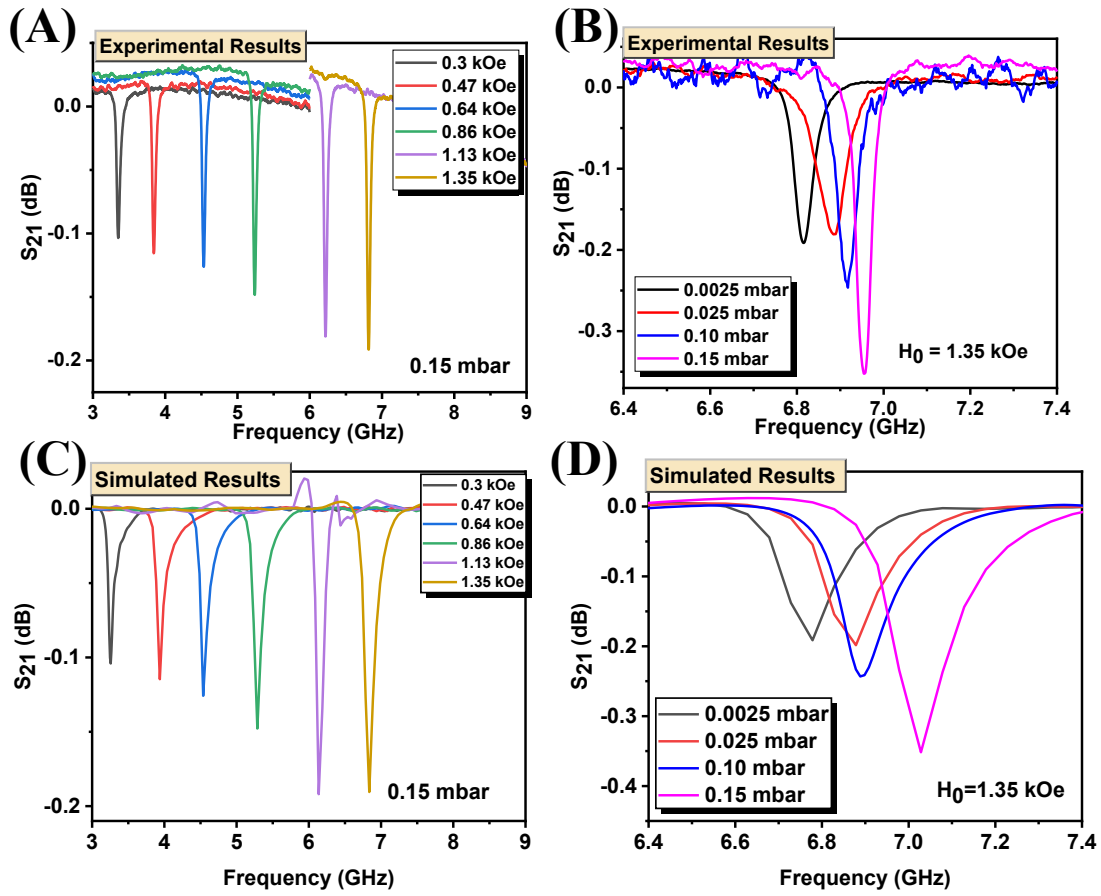

Fig. 4.4. (A) S_{21} parameter showing resonance frequencies measured at in-plane external magnetic field for YIG/GGG thin films at oxygen pressure of 0.15 mbar. (B) transmission response versus frequency at different oxygen growth pressure at fixed magnetic field. (C) HFSS calculated transmission spectra for YIG/GGG thin films at 0.15 mbar oxygen pressure, and (D) HFSS simulated S_{21} versus frequency at different oxygen pressure for all the samples at 1.35 kOe field.

To demonstrate reciprocal behavior of EM-wave propagation, frequency swept both transmission coefficients S_{21} and S_{12} data were measured with Keysight PNA-N5224a vector network analyzer using a S-type microstrip line.

Fig. 4.4 (B) depict the transmission spectra at a fixed magnetic field of 1.35 kOe of all four YIG films to demonstrate the effect of different oxygen growth pressure. The notch frequency for 0.0025 mbar film occurs at the lowest frequency of 6.8 GHz, whereas the

notch frequency increases in frequency unit for higher oxygen growth pressure films. For highest O_2 growth pressure of 0.15 mbar the notch frequency shifted to 6.96 GHz.

The increase of notch frequency indicates that there is an increase in saturation magnetization of the YIG films with the increase of oxygen growth pressure. This is an indication of better epitaxial growth of YIG film at higher pressures. Fig. 4.4 (C-D) shows the theoretical FMR spectra from finite element method solver (HFSS) for electromagnetic structures. The theoretical HFSS simulated spectra are in reasonable agreement with the experimentally observed data corresponding to Fig. 4.4 (A-B).

As we observed in S-type waveguide geometry, FMR mode propagation corresponds to the uniform precession mode (EM wave-vector $\boldsymbol{k}$ = 0), the relation between the notch-frequency f_r and in-plane external magnetic field for thin film geometry can be expressed by using Kittel's equation [92, 247]

$$f_r = \gamma' \sqrt{(H + H_k)(H - H_k + 4\pi M_s)} \qquad (4.3)$$

where γ' is the gyromagnetic ratio, $4\pi M_s$ is the saturation magnetization and H_k is the in-plane anisotropy field. The behavior of bandwidth or frequency-linewidth of the transmission dip as a function of field for different oxygen pressure grown YIG films are shown in Fig. 4.5 (A). Fig. 4.5 (A-B) clearly indicates that band-stop filter bandwidth decreases with the increase of oxygen pressure. This decrease is related to the improvement of film quality towards better epitaxial nature for higher oxygen growth pressure film. We observed that the field linewidth for a fixed frequency of 12 GHz has values of 66 Oe, 47 Oe, 25 Oe and 15 Oe for the oxygen pressure samples varying from 0.0025 mbar to 0.15 mbar respectively. The field linewidth also decreases with the increase of oxygen growth pressure which may be due to better YIG phase formation [229]. This makes the YIG thin film structure as a promising candidate for many microwave signal processing device applications, viz. magnetic memory, sensor, microwave passive and active filters etc.

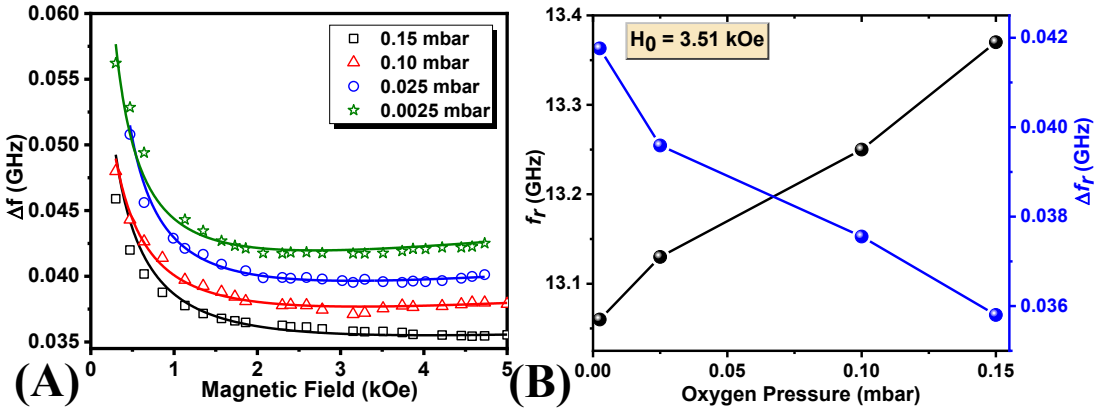

Fig. 4.5: (A) Frequency linewidth as a function of magnetic field, (B) Resonance frequency and frequency linewidths for different oxygen pressures.

Magnetization precession in magnetic media has a natural gyrotropy, i.e. a definite precession with respect to the direction of the internal magnetic field. The presence of such a naturally gyrotropic thin film in the immediate vicinity of a transmission line creates an effective gyrotropic boundary condition for the propagating wave and our goal is to develop the explicit form of this gyrotropic condition depending on the parameters of the thin magnetic film. As a result, the magnetic susceptibility of a magnetic medium is substantially different for left-handed and right-handed circularly polarized electromagnetic waves. This property is related to the axial nature of the magnetization vector and is not present in any non-magnetic materials. Thus, the properties of a magnetic medium can be different for electromagnetic waves propagating in opposite directions and, therefore, it is possible to realize nonreciprocal devices.

In isolators, generally a circularly polarized plane wave interacts strongly with a ferrite media when it rotates in the same direction as the precessing magnetic dipoles of the medium whereas the interaction with the ferrite material is less if a circularly polarized wave rotates in the opposite direction. The incident wave will be significantly reduced if the circularly polarized wave has the same direction of rotation as the processing magnetic dipoles although at the opposite port very small attenuation will be generated. Therefore, the position of the sample is crucially important to guarantee that the fields inside the

ferrite material are circularly polarized [248-250]. The non-reciprocity or the one-way propagation is generally observed due to the time-reversal and spatial symmetry breaking in magnetic materials such as gyrators. Further, some magnetic materials exhibit anisotropy which alters the response of h_{RF} when it is applied in opposite direction parallel to external magnetic field as shown in Fig. 4.3 (A-B). The following equation shows that the permeability is an antisymmetric tensor, with $\mu_{12} = -\mu_{21}$.

$$\mu = \mu_0 \begin{bmatrix} 1+\chi & -i\kappa & 0 \\ i\kappa & 1+\chi & 0 \\ 0 & 0 & 1 \end{bmatrix} \tag{4.4}$$

where $\chi = \frac{\omega_0 \omega_m}{{\omega_0}^2 - \omega^2}$, $\kappa = \frac{\omega \omega_m}{{\omega_0}^2 - \omega^2}$, $\omega_m = -\gamma 4\pi M_s$, and $\omega_0 = -\gamma H_0$. H_0 is the applied magnetic field and ω is the angular frequency. This is the primary cause of microwave propagation nonreciprocity in ferrite dielectric. Asymmetrically loaded magnetic materials on the microstrip line enhances the nonreciprocity with the violation of Lorentz reciprocity [240-244]. The condition is satisfied with an external static magnetic field applied such that electromagnetic waves with wave vector $\vec{k}$ propagate in a direction perpendicular to the bias field (magnetization vector) (Fig. 4.1 (A)). In this configuration, the polarization of the wave can be decomposed into transverse-magnetic (TM) and transverse-electric (TE) modes. Fig. 4.6 (A) shows the experimental data of forward and reverse transmission coefficients (S_{21} and S_{12}) of YIG/GGG thin films flipped on the microstrip line asymmetrically for different oxygen pressure grown films at a fixed magnetic field of 6 kOe. Similarly, Fig. 4.6 (B) demonstrates the HFSS simulated theoretical response of the non-reciprocity behavior of EM-waves inside the YIG films. It is clearly observed that there is non-reciprocity of the signal transmission for YIG thin films of thicknesses around 90 nm [236-244]. The origin of non- reciprocity for a straight microstrip line EM wave propagation can be explained due to the anisotropy present in the YIG thin films and asymmetric distribution of magnetic potential which can be either

on the surface of the film or in the bulk of the film. In both cases, the excitation and propagation are more efficient in one direction than in opposite direction resulting in unequal microwave absorption [251-254]. We have reported this effect in our earlier work in case of magnetic nanowires [239].

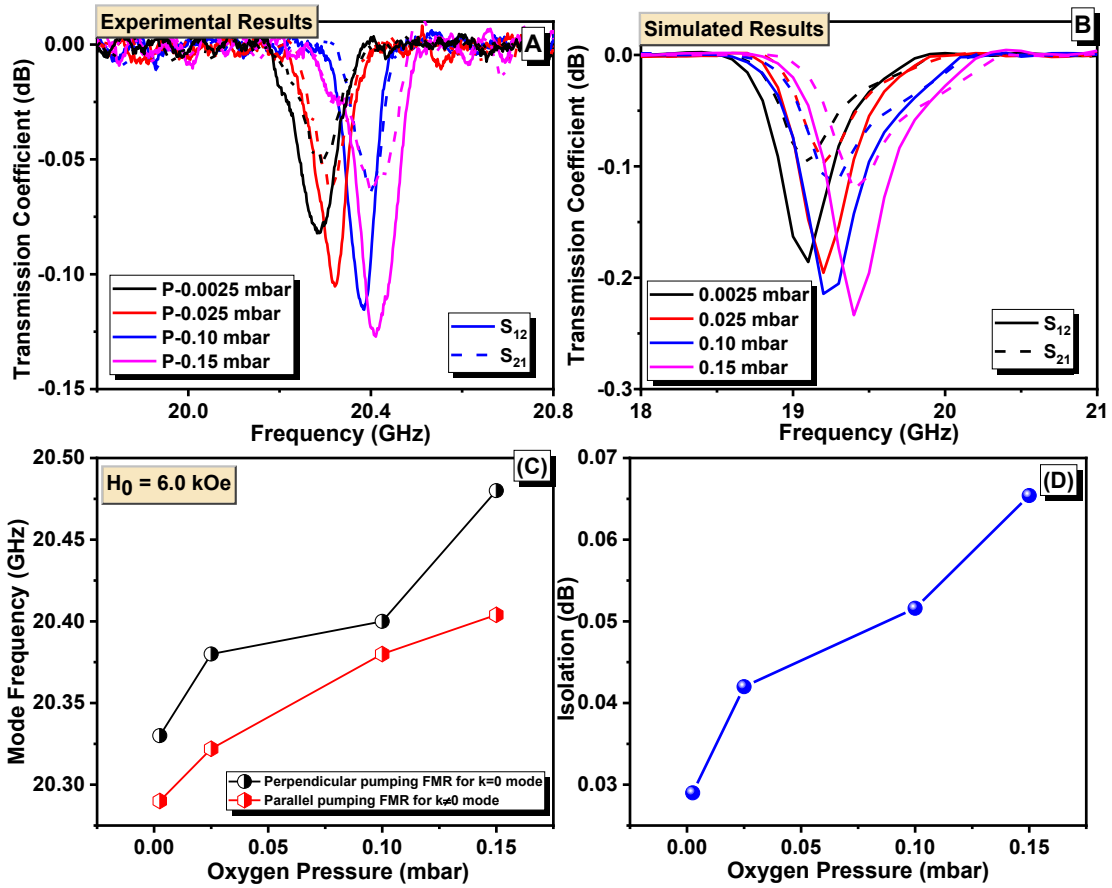

Fig. 4.6: (A) Experimental results of straight microstrip line transmission coefficients (S_{12} and S_{21}) for different oxygen gas pressure samples at a fixed external magnetic field of 6 kOe. (B) simulated results of transmission parameters exhibiting non-reciprocal behavior at a bias of 6 kOe. (C) A comparison of $\boldsymbol{h_{RF}} \perp \boldsymbol{H_{DC}}$ to $\boldsymbol{h_{RF}} \parallel \boldsymbol{H_{DC}}$ FMR frequencies as a function of different oxygen pressure. (D) non-reciprocal propagation (isolation) for various samples at different oxygen growth pressure

This is because the microwave electric field outside the center conductor and the ground electrodes are tangential to the air-dielectric boundary that produce a discontinuity in

displacement current density at the interface when the YIG was placed in asymmetrical position in a straight microstrip-line and the dc bias was applied normal to EM-wave propagation direction. This may also be attributed to magnetic anisotropy of the material where the precession of magnetization can align with the applied magnetic field leading to an efficient energy exchange [236, 237]. As illustrated in Fig. 4.3 (B), the configuration can be visualized as a half-mode planar microstrip waveguide (PMW) isolator. It is with a perfect magnetic conductor (PMC) boundary condition approximated along the open side (side without YIG film) of the microstrip waveguide.

The asymmetry demonstrates that effective permeability has negative value in a certain frequency region. As a result, if a wave propagates within this band of frequencies inside the waveguide, it will be absorbed by the material in one direction, resulting in severe insertion loss while enabling transmission in the opposite direction. This negative permeability band can be controlled to regulate the isolation band by varying the applied bias. When the magnetic field is perpendicular to the RF field i.e. in FMR condition, the anisotropic effects that cause non-reciprocity are absent as observed in Fig. 4.3 (C-D) for both the symmetrical as well as asymmetrical position. Therefore, appropriate choice of microstrip line is an important selection for the design of reciprocal and non-reciprocal microwave devices.

Fig. 4.6 (B) demonstrates the HFSS simulated transmission parameters for asymmetric placed YIG thin films for Fig. 4.1 (A) configuration. It is emphasized here that the simulated results match well with our experimental results. For all the studied samples, we observe that the magnitude of non-reciprocity (isolation) increases with the increase of magnetic field. Interestingly, isolation for highest oxygen pressure grown YIG film exhibit the maximum isolation.

Fig. 4.6 (C) shows a comparison of mode frequencies for parallel-pumping resonance [($\boldsymbol{k \neq 0}$) with $\boldsymbol{h_{RF} \parallel H_{DC}}$] using the Straight-type microstrip line along with the uniform precession FMR ($\boldsymbol{k = 0}$) with $\boldsymbol{h_{RF} \perp H_{DC}}$ geometry obtained by using a “S” type microstrip line for all samples at a fixed magnetic field of 6 kOe. The uniform precession

FMR mode frequencies occur at higher values than the $\boldsymbol{k \neq 0}$ modes (parallel pumping) generated frequencies using straight microstrip line. Hence, these two mode frequencies are different to each other. The highest isolation of 6.54 % was observed for 0.15 mbar sample at an applied magnetic field of 6 kOe as shown in Fig. 4.6 (D). We observed that the isolation increases with increase of oxygen pressure up to 21.6 % in experimental results and are comparable to simulated results of 26.6%.

The increase in isolation can be related to anisotropy present in the YIG thin films, as anisotropy is much more sensitive to iron ions recharging which is caused by changing of oxygen non-stoichiometry. More oxygen pressure means more Fe^{3+} ions generation for higher oxygen pressure which increases magnetic moments and hence there is an increase of saturation magnetization and hence isolation. Further, it is important to mention here that non-reciprocity can be achieved for a 90 nm thick YIG/GGG thin films when it is flipped asymmetric on the microstrip signal line. These results open upon up a direction for the design of microwave nonreciprocal devices like isolator and circulators for sensitive RF front end and microwave planar devices.

One can even increase the operating range by applying the external magnetic field further. As our intention is to identify the isolation characteristic in a broad frequency range, we have tuned the operating frequency of the YIG-based devices by changing DC magnetic field (H_0). We have observed a distinct isolation, though very small in amplitude, in our YIG thin films of 90 nm. The observed parameters from both reciprocal and non-reciprocal EM wave propagation like bandwidth/frequency linewidth, insertion loss for stop-band frequency and non-reciprocity for different oxygen gas pressure grown YIG films were tabulated in table 4.2.

Table 4.2: Device Parameters for various oxygen pressure growth samples.

Oxygen Pressure (mbar)	Frequencies @ field (3.51 kOe)		Isolation % @ field (6 kOe)
	Bandwidth (MHz)	Band-rejection (dB)	
0.0025	41.76	0.280	2.9
0.025	39.59	0.292	4.2
0.10	37.56	0.300	5.16
0.15	35.8	0.393	6.54

4.4 Conclusions

We have successfully demonstrated both experimentally and theoretically through finite element method HFSS simulations the reciprocal and non-reciprocal electromagnetic wave propagation in microwave frequency range using different transmission lines using 90 nm thick YIG film as active element. Reciprocal propagation was used to study the uniform precession FMR modes ($\boldsymbol{k} = \mathbf{0}$ modes) for the design of notch-filters. We have also demonstrated the non-reciprocal EM-wave propagation in YIG/GGG thin films with $\boldsymbol{k} \neq \mathbf{0}$ modes which produce isolation for the design of an isolator. Further, it is demonstrated that different oxygen growth pressure grown YIG films show different characteristics and the best device parameters are achieved at highest oxygen pressure grown YIG thin film. A comparison of mode frequencies with magnetic field for two configurations revealed that uniform precession mode occurs at higher frequency than the $\boldsymbol{k} \neq \mathbf{0}$ modes. We achieved a frequency tunability to 85.3% for stop-band resonance frequencies with an external magnetic field of 6 kOe. From the $\boldsymbol{k} \neq \mathbf{0}$ modes we have achieved non-reciprocity/isolation. The maximum isolation of about 6.54% with 0.15

mbar oxygen gas pressure YIG film was achieved at a dc bias field of 6 kOe. Moreover, the non-reciprocity behavior observed to increases significantly with the increase of externally applied magnetic field. Hence, it is well demonstrated in the present investigation that a sub-100 nm YIG film can be used for reciprocal and non-reciprocal microwave devices, a way towards miniaturization of microwave signal processing devices.

Chapter 5

Effect of controlled oxidation of Ni to NiO in YIG/Ta/Ni heterostructure

Asymmetric trilayers, particularly those including heavy metal tantalum (Ta) as a spacer, are less explored. The derived spin pumping induced damping (α_{sp}) of ferromagnet/heavy metal/anti-ferromagnet ($FM_1/HM/FM_2$) and ferromagnet/heavy metal/anti-ferromagnet (FM/HM/AFM) trilayers reveals a direct dependence on the spacer layer dynamics. In this investigation to understand the contribution of the spin injection more quantitatively we address the technological perspective of $FM_1/HM/FM_2$ and FM/HM/AFM trilayer films in spintronic applications. Using ferromagnetic resonance spectroscopy (FMR), we investigate how a 4 nm non-magnetic heavy-metal spacer layer, Ta, affects the ferromagnetic relaxation (damping) through spin pumping in epitaxial YIG thin films on GGG substrate coupled with Ta and Ni (YIG/Ta/Ni) structure. In our tri layered structure (YIG/Ta/Ni), the spin pumping from upper and lower FM layers are different. The spin-pumping mediated Gilbert damping (α_{sp}) was calculated as 1.0×10^{-4} for YIG and 1.0×10^{-2} for Ni layer in the YIG/Ta/Ni structure. As YIG is ferrimagnetic (FM_1) and Ni is a ferromagnetic (FM_2) the spin currents at the opposite interfaces of Ta layer act differently on the magnetization vectors of the neighbouring magnetic layers. We found that the results in YIG/Ta/Ni can be self-consistently interpreted by a standard spin pumping theory with $g^{\uparrow\downarrow}$ (YIG)= $1.39 \times 10^{17} \pm 0.10 \times 10^{17}$ m^{-2} and $g^{\uparrow\downarrow}$ (Ni)= $1.17 \times 10^{18} \pm 0.05 \times 10^{18}$ m^{-2}. Further, there is enhancement of spin pumping in epitaxial YIG thin films after the oxidation of top Ni layer to antiferromagnetic NiO (YIG/Ta/NiO). The spin-pumping effect is detected as further broadening of ferromagnetic resonance linewidth. It is found that the oxidation of (FM_2) Ni to (AFM) NiO layer leads to enhancement of effective Gilbert damping (α_{eff}) of YIG from 1.35×10^{-3} to 1.55×10^{-3} of the trilayer structures.

Hence spin-pumping mediated Gilbert damping (α_{sp}) was calculated as 1.0×10^{-4} and 2.2×10^{-4} for YIG/Ta/Ni and YIG/Ta/NiO trilayers (i.e., ~100% increment). The broadening of linewidth indicates the efficient spin transfer due to the presence of anti-ferromagnetic NiO through spin back-scattering mechanism. The derived parameters like Gilbert damping, zero-frequency linewidth (ΔH_0) and mixing conductance indicate considerable enhancement from YIG/Ta/Ni structure to YIG/Ta/NiO ($1.39 \times 10^{17} \pm 0.10 \times 10^{17}$ m^{-2} to $2.31 \times 10^{17} \pm 0.16 \times 10^{17}$ m^{-2}). The presence of NiO layer enables the enhanced spin-current transmission due to spin back-flow at the Ta/NiO interface and hence considerably enhanced effective spin-mixing conductance at the interface. Before investigating the spin dynamics, we have investigated the structural and surface morphological properties using X-ray diffraction, Raman spectroscopy and atomic force microscopy. The conversion of Ni to NiO were demonstrated with the change in structural and surface morphological properties. These studies provide an alternative path towards next generation magnetic switching devices.

5.1 Introduction

Spin current is a flow of spin angular momentum that shares several analogies with electric currents. Spin currents can be conveyed not only by migrating electrons but also by magnetic quasiparticles, including magnons or spin waves [255-259]. In the development of spintronic devices, a significant challenge comes in the long-range transfer of spin angular momentum. Such magnetic stimulations are particularly significant in the spintronics field since they facilitate the passage of spin currents in electrical insulators, where charge currents are not feasible [8, 260]. The occurrence of the spin current transfer from a precessing magnetization to the neighboring heavy metal (HM) layer in the ferro/ferrimagnet (FM) layer is called as Spin pumping. This phenomenon occurs when there is an occurrence of the nonequilibrium spin accumulation in the HM layer and arises due to the dynamic and coherent precession of the

magnetization vector around H_{eff} in a FM layer. Spin pumping in an FM/HM/FM trilayer refers to the generation of a spin current in the heavy metal (HM) layer due to the precession of magnetization in the ferromagnetic (FM) layers, particularly during ferromagnetic resonance (FMR). This process can lead to an enhanced damping in the FM layers and potentially drive long-range magnetic order or collective precession in the trilayer system. Similarly, insulator spintronics may offer a pathway to low-power electronic devices in which spin currents transmit signals and encode information [176, 261-262]. Spin pumping in an FM/HM/AFM trilayer refers to the transfer of spin angular momentum from a precessing ferromagnetic (FM) layer to both a normal metal (NM) or heavy metal (HM) layer and an antiferromagnetic (AFM) layer via spin currents. This phenomenon is crucial for understanding and utilizing spin-orbit torque switching and multi-mode energy harvesting in spintronics. In an FM/HM/AFM trilayer, the spin current generated in the FM layer can flow into both the HM layer and the AFM layer. The spin current injected into the HM layer can be detected using the inverse spin Hall effect (ISHE), which converts the spin current into a measurable voltage. The spin current injected into the AFM layer can induce oscillations in the AFM layer, which can then lead to further spin pumping and spin current generation. Spin pumping in a ferromagnet/heavy metal/antiferromagnet (FM/HM/AFM) trilayer involves the transfer of angular momentum from a precessing ferromagnetic layer to the adjacent heavy metal and, subsequently, to the antiferromagnetic layer. This process, known as spin pumping, is characterized by the generation of a spin current in the HM layer due to the magnetization dynamics in the ferromagnet. The spin current then propagates into the AFM layer, influencing its magnetic properties and potentially leading to observable effects like changes in the damping of the ferromagnet. AFM materials are gaining attention in spintronics due to their potential for high-density memory, fast switching speeds, and robustness against external perturbations. Spin pumping in FM/HM/AFM structures can be used to study and control antiferromagnetic order, potentially leading to new types of spintronic devices.

The interface between the HM and AFM layers plays a crucial role in spin pumping and spin transport. Factors like interface roughness, intermixing, and interfacial magnetic coupling can influence the efficiency of spin current transfer. Currently, spin transport and magneto-dynamics in antiferromagnetic (AF) insulators have garnered significant interest among researchers [60-62]. Specifically, employing AF insulators as an insertion barrier in magnetic devices utilizing spin-orbit torque (SOT) may effectively eradicate shunting currents within the free layer and reduce Joule heating [263]. Wang et al. demonstrates enhancement of spin currents with the insertion of NiO layer between YIG and normal metal (NM=Pt) [76]. Qiu et al. observed two orders of magnitude difference in the transmitted spin current with YIG/Cr_2O_3/Pt trilayer [264]. They ascribe this significant alteration of spin current to the interplay between the anisotropic spin current transmission of the antiferromagnet and the device shape, which is associated with the Néel vector and anisotropy of Cr_2O_3. Further, thermally injected spin current was shown to increase in NM/AF/YIG with NiO and CoO as insulating layer. The spin-mixing conductance at the HM/YIG interface for NM of 3d, 4d and 5d metals demonstrates linear increment with AF in between [265]. Nonlocal spin current in an antiferromagnetic NiO can be attributed to magnon-polaron interaction. A characteristic length scale for magnon-polaron formation in antiferromagnets can produce nonlocal spin transport. This can be further elucidated by noting that the ferromagnet and anti-ferromagnet magnons possess distinct properties. In an earlier work it is demonstrated that an effective FM-AFM interaction mediated via the conduction electrons in the nonmagnetic Cu spacer is detected which results to an enhancement of the ferromagnetic resonance linewidth via a broadening of the FMR spectra. They further find experimentally that the spin-pumping-induced contribution to the linewidth from a metallic ferromagnetic layer (FM) pumps spin current into the non-magnetic antiferromagnetic film (AFM) layer placed behind a spacer layer of Cu. [266-267].

At present there are no studies of asymmetric trilayer structure ferromagnet/heavy metal/ferromagnet with Ta inter-layer. In the present work, we report the effect of

controlled oxidation of Ni to NiO in YIG/Ta/Ni to understand the spin transport in the heterostructure. The 2θ XRD scan and Raman spectra confirm the formation of heterostructures and transition of Ni to NiO. The root-mean-square (rms) roughness was determined from atomic force microscopy (AFM). Using ferromagnetic resonance (FMR) measurements, we focused on the change in linewidth under the spin current injection which reflects the change in effective damping parameter due to anti-damping spin torque due to spin current. Also, the spin-mixing conductance was determined and observed a significant enhancement with the presence of a NiO AF layer. Furthermore, there are very few reports on the spin pumping in tantalum (Ta) in asymmetric trilayer systems, making the YIG/Ta/Ni heterostructure a novel and compelling system for investigation.

5.2 Experimental procedure

5.2.1 Synthesis of heterostructures

Pulsed laser deposition (PLD) technique was used to grow single crystalline YIG thin films on GGG (111) substrates (MTI Corporation, USA). A KrF excimer laser of wavelength 248 nm was used to ablate the materials for the thin film growth in the PLD system. To grow high quality YIG thin films, 300 mJ energy was used with a pulse repetition frequency of 10 Hz to ablate the YIG target. We have used a turbo molecular pump to generate a base pressure of 1×10^{-6} mbar. Top layer impurity of the substrates was removed by pre-heating at 800 °C. The deposition was carried at an oxygen pressure of 0.10 mbar. The rate of growth of the YIG films were maintained at ~ 0.5 Å/sec. For this thickness film deposition, 15,000 shoots were applied. We have performed an in-situ annealing for 2 hours at 800 °C on the films. Thereafter the films were cooled down to room temperature. Throughout the in-situ annealing process Oxygen atmosphere was maintained [229]. On the YIG film, ultra-thin layer of Ta followed by a thin layer of Ni was deposited using rf sputtering. After each deposition, AFM technique was used to measure the film thicknesses which was found to be ~ 90 nm for YIG. A 4 nm Ta metallic

layers was used as a capping layer. On top of Ta layer, we have deposited a 20 nm Ni layer by using a sputtering system. Further, Ni layer was oxidized at a temperature of 500 °C under O_2 atmosphere to convert Ni to NiO layer. Ta layer which is an effective self-limiting oxide spacer layer was used to fabricate the trilayer structure.

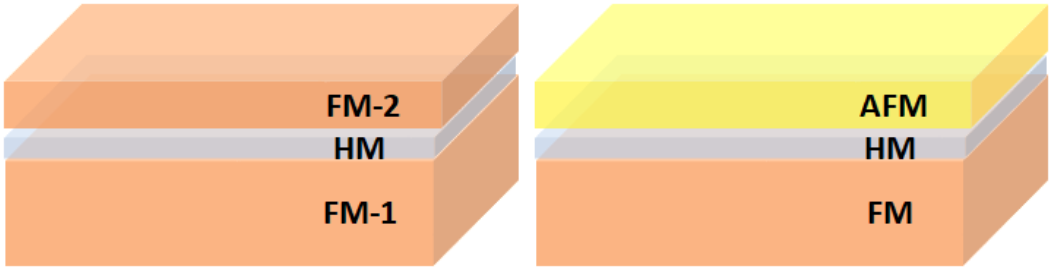

Fig. 5.1: Schematic of investigated heterostructure

In addition to above structures, we have deposited the single layer films of YIG and Ni layers. YIG was deposited on single crystalline GGG (111) substrate by using a PLD system. Whereas Ni was deposited on top surface oxidized Si substrate as $Si/SiO_2/Ni$ by using a sputtering system. It is to mention here that, though FMR is a powerful technique to evaluate effective fields, magnetic anisotropy, Gilbert damping etc. The use of broadband FMR alone to ascertain spin transport in trilayer spin-valve systems is quite uncommon.

5.3 Characterization

The X-ray diffraction method (XRD - Miniflex Rigaku diffractometer), which utilizes Cu Kα radiation with a wavelength of 1.5406 Å, was used to examine the thin films' structural characteristics. Atomic force microscopy (AFM) with a WITech Alpha 300 RA system was used to test the films' quality and roughness. The system was operated in AC (tapping mode) with a non-contact cantilever that had a low force constant (45 N/m) and a high resonance frequency (250 KHz). The phase development of YIG, Ni, and NiO was

further confirmed by Raman spectroscopy (WITech Alpha 300 RA) at a resolution of 1 cm^{-1}.

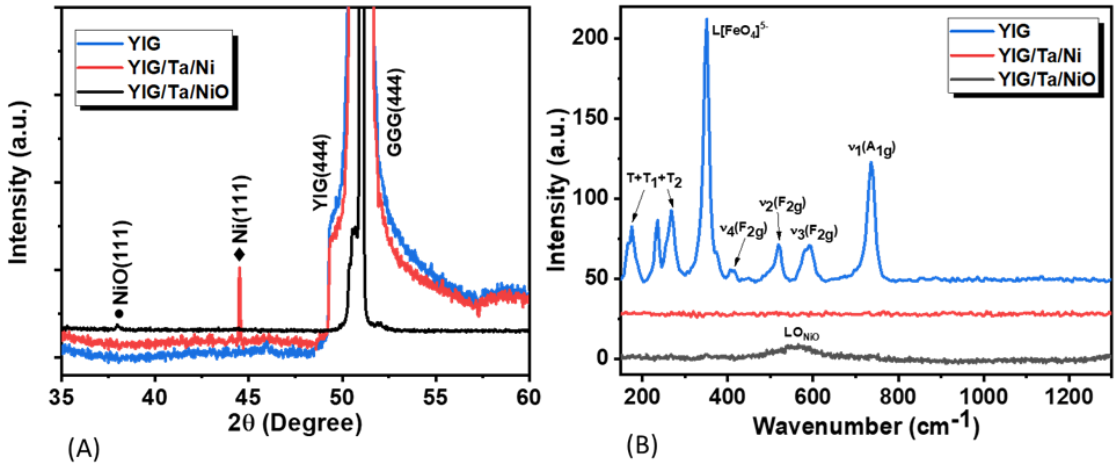

Fig. 5.2: (A) XRD pattern (B) Raman Spectra, of YIG, YIG/Ta/Ni and YIG/Ta/NiO thin films.

Using a magnetic field applied along the film's in-plane geometry, the physical properties measurement system (PPMS - Cryogenics Limited (Model - J103), UK) was used to conduct the dc magnetic measurements. Detailed ferromagnetic resonance (FMR) measurements were carried out by using a Keysight Vector Network Analyzer (VNA) along with a "S" shaped coplanar waveguide (CPW). The measurements were performed in a flip-chip configuration with the film surface flipped downward on the CPW transmission line. To maintain FMR condition the high-frequency magnetic field (h_{RF}) was made to propagate perpendicular to the DC magnetic field. The measurements were done in field sweep mode at different the frequencies varied from 8 GHz to 14 GHz. The obtained FMR spectra was fitted using Lorentzian function to determine resonance field and field linewidth.

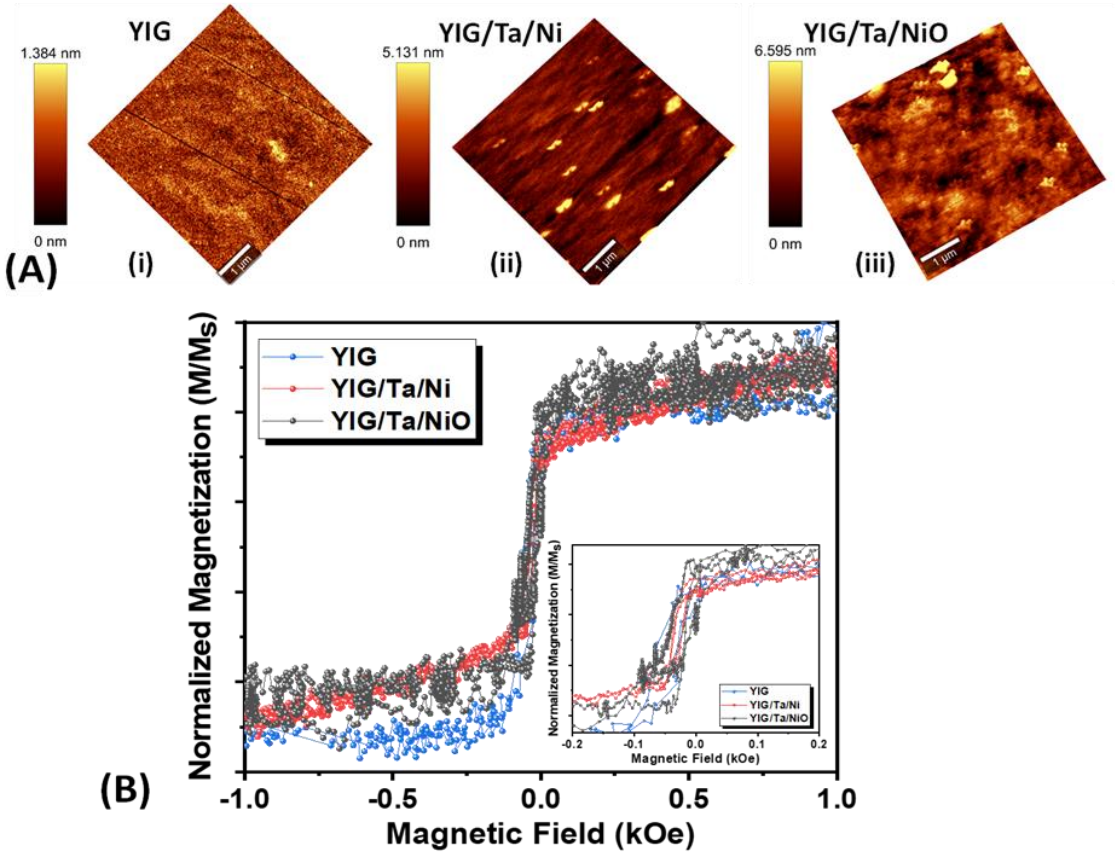

Fig. 5.3: A (i-iii) AFM images of the bare YIG film, YIG/Ta/Ni film, and YIG/Ta/NiO film. (B) Magnetization curve as a function of applied magnetic field for the investigated heterostructures, (inset: zoom in at zero magnetic field).

5.4 Result and discussion

5.4.1 Structural and magnetic properties of heterostructure

The structural properties were characterized using X-ray diffraction technique (XRD). Fig. 5.2(A), depicts the XRD data of pristine YIG, YIG/Ta/Ni and YIG/Ta/NiO films which confirmed the formation of heterostructures and transition of Ni to NiO. The pristine YIG showed the signature of single crystallinity over GGG (111) substrate. A sharp peak of Ni (111) was observed at 44° for YIG/Ta/Ni and with further oxidation Ni

switched to NiO with preferred orientation along (111) plane [165]. Similar confirmatory results were obtained from the Raman spectroscopy. Fig. 5.2(B) shows Raman spectra of pristine YIG, YIG/Ta/Ni and YIG/Ta/NiO heterostructure indicating the transition of Ni metal to NiO after oxidation. YIG peaks can be seen from the Raman spectra at around 168, 180, 235, 269, 381, 415, 485, 580, and 600 cm^{-1}, respectively [196]. The most intense peak at 269 cm^{-1} which reflects $L[FeO_4]^{5-}$translational modes, is associated with ferromagnetic nature. GaO_4 and GaO_6 internal vibrations in GGG substrates are linked to the A_{1g} modes at peaks 355 and 741 cm^{-1}, respectively [197]. Due to metallic nature of 20 nm thick Ni, no peak was observed in Raman spectra for YIG/Ta/Ni film. The LO vibrational mode of NiO is prominently visible in the Raman spectra of YIG/Ta/NiO heterostructure.

Fig.5.3 [A(i-iii)] shows the atomic force microscopy (AFM) measurements of a bare YIG film, YIG/Ta/Ni and YIG/Ta/NiO heterostructure revealing that the root-mean-square (rms) roughness increases from 0.33 nm to 1.89 nm, respectively. Fig. 5.3(B) shows the magnetic hysteresis loop of all the investigated samples. The pristine YIG film exhibits a square hysteresis loop with a very small coercive field of 12 Oe and a sharp magnetic switching, implying exceptionally high magnetic uniformity [199]. The incorporation of Ni causes negligible reduction in coercivity indicating improved ferromagnetic nature. We observed clearly from the inset of Fig. 5.3(B) oxidation of Ni to NiO, the coercivity gets almost double suggesting it's antiferromagnetic nature.

5.4.2 Spin dynamics of single layered YIG and Ni films

Before investigating the spin dynamics of trilayers structure $FM_1/NM/FM_2$ we have deposited the single layer films of YIG and Ni separately as mentioned earlier. Fig.5. (4) depict the FMR measured spectra and the derived resonance fields (Hr) and FMR linewidth of a 90 nm thick epitaxial thin film.

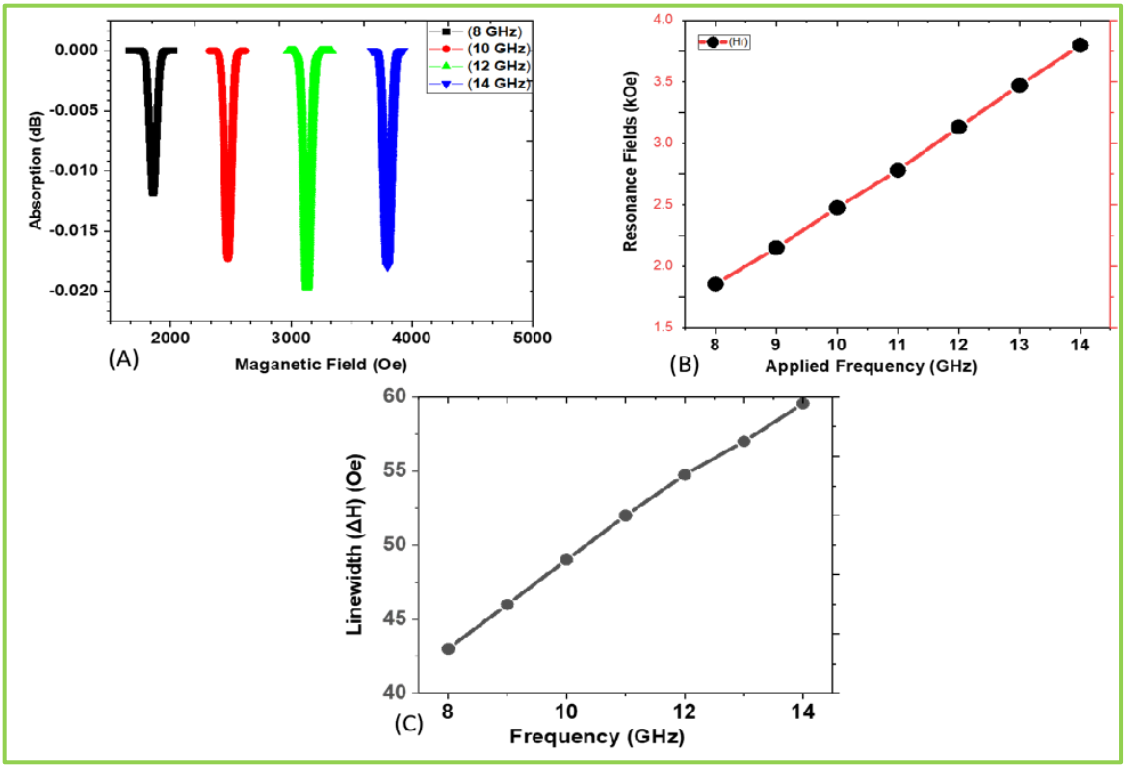

Fig.5. 4: (A) FMR response of bare YIG film deposited on GGG (111) substrate. (B) show the extracted resonance fields (Hr) and (C) are the extracted FMR linewidth by Lorentzian fits.

Fig. 5.4 (A) shows the ferromagnetic resonance (FMR) spectra of 90 nm thick epitaxial ferrimagnetic YIG thin film deposited on GGG (111) substrate at an elevated temperature by PLD. Using the sum of the symmetric and antisymmetric Lorentzian functions, the resonance fields (H_r) and field linewidths (ΔH) were derived from the FMR spectra. Fig. 5.4 (B) depicts the resonance field as a function of frequency, whereas Fig. 5.4(C) depicts the resonance linewidths as a function of frequency. The high oxygen pressure of 0.10 mbar used during sample deposition have induced FMR spectra with narrow linewidths.

This is because the YIG films grown at high O_2 pressure induced much lesser root-mean-square (rms) roughness of 0.33 nm from AFM images shown in Fig.5.3(A i-iii). Hence,

they have much better substrate to film interface matching. This reduces the extrinsic contribution to linewidths. This is a marked feature of perfect epitaxial growth for YIG film with a much narrower spectra and the larger resonance absorption dips. As observed in our earlier work the epitaxially grown YIG film has the direction of the magnetic moments are along the film plane [229].

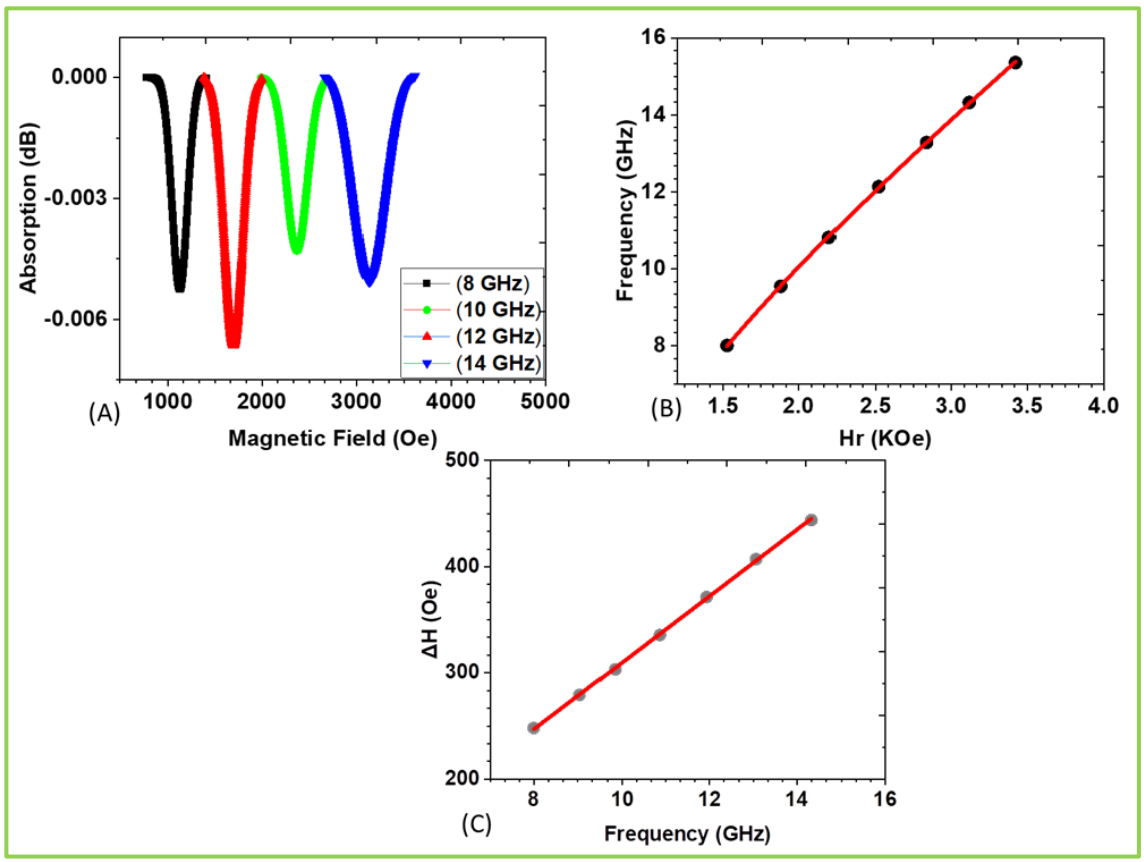

Fig. 5.5: (A) FMR spectra of a single layered Ni film of 20 nm thick deposited by using a sputtering system. (B) show the resonance fields (Hr) and (C) FMR linewidth derived by Lorentzian fits.

One Ni film of thickness 20 nm was deposited by using the sputtering system. The measured FMR signal, i.e. absorption (S_{21}) versus magnetic field swept applied in the plane of the film from zero to 4 kOe at different fixed frequency was used to obtain the

FMR spectra as depicted in Fig. 5.5 (A). Each FMR spectrum was fitted to a Lorentzian function to derive the resonance fields (shown in Fig. 5.5 (B) and resonance linewidths (shown in Fig. 5.5 (C)). For an in-plane FMR measurement, the resonance fields of Ni (shown in Fig. 5.5 (B)), which is a ferromagnetic metal occurred at a lower field in comparison to YIG, which is a ferrimagnetic insulator. This is obvious as metallic Ni has a higher saturation magnetization in comparison to YIG having a lower saturation magnetization. Additionally, FMR linewidths of metallic Ni (shown in Fig. 5.5 (C)) are more than 10 times larger than the ferrimagnetic insulator, YIG.

To analyse the FMR resonance fields and linewidths of single layer YIG and Ni, we have used the Kittel's equation (eq.1) for in-plane configuration of FMR. By fitting the resonance fields versus frequency data of both YIG (Fig. 4(B)) and Ni (Fig. 5.5(B)) measured at different applied frequencies, we have determined the effective magnetizations ($4\pi M_{\text{eff}}$) and in-plane anisotropy field (H_k) in addition to gyromagnetic ratio both for YIG and Ni films.

$$f = \frac{\gamma}{2\pi}[(H_{\text{res}} + H_k)(H_{\text{res}} + H_k + 4\pi M_{\text{eff}})]^{1/2} \tag{5.1}$$

The solid lines in Fig. 5.3(B) and Fig. 5.4(B) represent fits to the data points using eq. (5.1). The measured $4\pi M_{\text{eff}}$ values are 2.2 kOe and 6.48 kOe for YIG and Ni respectively. Similarly, the in-plane anisotropy fields for YIG and Ni are derived as 70 Oe and 40 Oe, respectively. The gyromagnetic ratio γ' ($=\gamma/2\pi$) are 2.91 and 2.27 obtained for YIG and Ni films respectively. As the measured $4\pi M_{\text{eff}}$ values of YIG as well as Ni are equal or close to the bulk values of the corresponding system. The linear variation in ΔH both for YIG (Fig. 5.4(C)) and Ni (Fig. 5.5(C)) as a function of applied frequency indicate that the origin of damping is intrinsic in nature. By using the phenomenological equation;

$$\Delta H = \Delta H_0 + \frac{4\pi\alpha_{int}}{\gamma} f \tag{5.2}$$

and fitting the data of Fig. 5.4(C) and Fig. 5.5 (C) for the variation of ΔH versus f_r, we derived the intrinsic damping parameter (α_{int}) both for YIG as well as Ni. The solid lines

in Fig. 5.4(C) and Fig. 5.5 (C) represent linear fits to the data using eq. (5.2). From the slope of Eq. (5.2) we determine the intrinsic Gilbert damping parameters as 1.35×10^{-3} for YIG and 4.28×10^{-2} for Ni films respectively.

5.4.3 Spin Pumping in asymmetric YIG/TA/Ni

Spin pumping in an FM/HM/FM trilayer refers to the phenomenon where a precessing magnetization in one ferromagnetic (FM) layer generates a spin current vide transfer of spin angular momentum that flows into the adjacent non-magnetic (heavy metal - HM) layer and then into the other FM layer. This process is essentially a spin current transfer from one FM layer to another via an intermediate HM layer. It can be understood as a consequence of ferromagnetic resonance (FMR) in the FM layers, where the precessing magnetization acts as a source of angular momentum that is transferred to the adjacent layers. In coupled $FM_1/HM/FM_2$ systems, there will be dynamic coupling between two ferromagnetic layers which is a result of spin pumping phenomenon. This nonlocal damping happens for a trilayers structure as a result of the simultaneously ejection of spin currents from both the ferromagnetic layers. In an asymmetric trilayer, the spin pumping induced damping is dependent on the precessing magnetizations' phase and amplitude. When the two FM layers are different as YIG/Ta/Ni, the two different FM/HM interfaces result in two different values of spin dynamics namely, pumping induced Gilbert damping and hence mixing conductance $g^{\uparrow\downarrow}$. For an asymmetric trilayers system, $g^{\uparrow\downarrow}$ results in a directional dependent spin current transfer from FM_1 and FM_2 into the HM spacer layer. Therefore, it is important to quantify the value of mixing conductance to correctly describe the spin transport in a trilayers system with asymmetric interfaces adjacent to the HM layer.

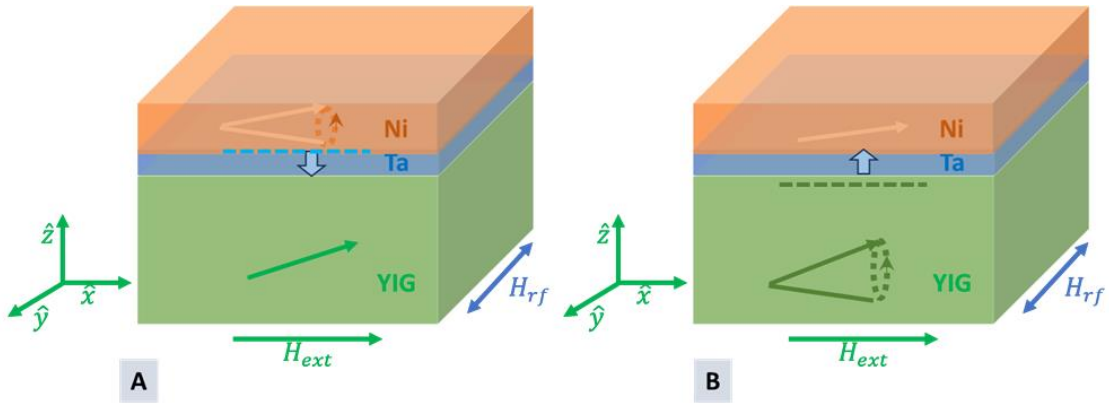

Fig. 5.6: depicts asymmetric $FM_1/HM/FM_2$ (FM_1=YIG and FM_2=Ni) trilayers at magnetization precession at 10GHz (A) with Ni magnetization precession at 1.6 kOe and (B) YIG magnetization precession at 2.45 kOe. [273]

In YIG/Ta/Ni spin-valve trilayer structure depicted in Fig. 5.6(A) and 5.6(B), where heavy metal spacer layer Ta with a thickness of 4 nm, makes the two FM layers as decoupled and is exemplified with two distinct resonance peaks. Each FM layer representing independent precession of magnetization. The ferromagnetic metal Ni film goes to resonance (H_{r1}) at a lower magnetic field with a broader FMR linewidth (ΔH_1). In contrast the ferrimagnetic YIG film goes to resonance (H_{r2}) at a higher magnetic field but with a much narrower linewidth (ΔH_2). Fig.5.7 (A) reveals the ferromagnetic resonance (FMR) spectra of trilayer $FM_1/HM/FM_2$ heterostructures of YIG/Ta/Ni. At different applied frequency, YIG/Ta/Ni heterostructure structure exhibit two distinct resonances for two different magnetic layers, viz. YIG and Ni, which are separated by a heavy metal of 4nm Ta as spacer layer. The epitaxial YIG film which was grown by a PLD system shows a very sharp resonance at 1.9 kOe, whereas Ni resonance dip occurred at 1.1 kOe. With the increase of the frequency of applied microwave, both resonance fields and linewidths increase to higher values both for YIG and Ni films. These findings corroborate the insights related to the two asymmetric FM layers.

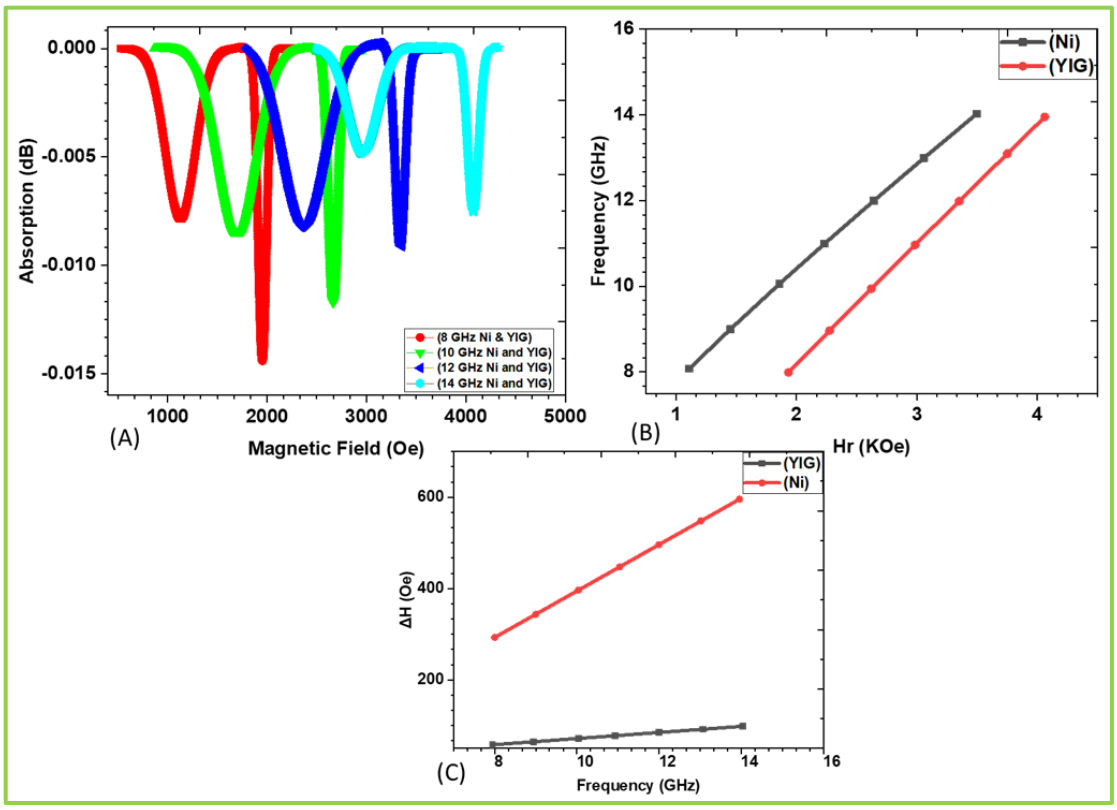

Fig. 5.7: (A) Field sweep FMR profile of heterostructure thin film at different frequency (B) Resonance fields as a function of frequency for the heterostructures. (C) Field linewidth as a function of frequency for the heterostructures.

We observed symmetric base-lines, both for YIG resonance as well as Ni resonances. The effective magnetizations ($4\pi M_{\text{eff}}$) were calculated by fitting the frequency vs H_{r} data of YIG and Ni measured at different applied frequencies using the FMR equation as given in eq. (1) for in-plane configuration. The solid lines to Fig. 5.7 (B) are the fitted lines to the experimental data points. The measured $4\pi M_{\text{eff}}$ values are 2.09 kOe and 7.2 kOe for YIG and Ni respectively. As the measured $4\pi M_{\text{eff}}$ values of YIG as well as Ni are equal or close to their bulk values, it is confirmed that the FM films are in the "decoupled" state in the YIG (90 nm)/Ta (4 nm)/Ni (20 nm) trilayers system.

Fig. 5.7 (C) depicts the dependence of the FMR linewidths (ΔH) of the YIG and Ni resonance spectra as a function of FMR excitation frequencies across 4 nm Ta layer.

A through comparison of FMR spectra of Fig. 5.4 and Fig. 5.5 corresponding to single layer films of YIG (90nm) and Ni (20nm), respectively to the spectra of trilayer YIG (90nm)/Ta (4nm)/Ni (20nm) we have the following observations:

(i) The values for the resonance fields both for YIG and Ni layers are almost same for the single layer as well as for the corresponding YIG and Ni layers of the trilayer structure over all the microwave frequency points.

(ii) But the resonance linewidth of single layer and the corresponding layer of the trilayer are the very different. Both the YIG and Ni spectra of the trilayer system are broader than in the single layer films.

(iii) There is a large increase of linewidths for both YIG and Ni films in the trilayer system in comparison to single layer films. For example, at 10 GHz

(iv) The linear variation in ΔH both for Ni and YIG as a function of applied frequency indicate that the origin of damping is intrinsic in nature. By using the phenomenological equation as described in eq. (5.2).

Eq. (5.2) which depict a linear correlation between the ΔH and f_r, we deduce the effective damping parameter (α_{eff}) both for YIG as well as Ni. The fits to the data of resonance field versus applied frequency is shown by the solid lines in Fig. 5.4 (B). The effective Gilbert damping parameters were determined from the slope of Eq. (5.3), which results in the extraction of spin pumping induced damping parameters. Gilbert damping parameter obtained for YIG and Ni in the trilayers structure are 1.45×10^{-3} and 5.28×10^{-2}, respectively. The inhomogeneous linewidth broadening (ΔH_0), i.e. the zero-frequency offset, due to variations in crystal structure, strain, composition, or defects across the film. The values of ΔH_0 as observed from fitting are 27 Oe and 35 Oe for bare YIG film and for YIG in the YIG/Ta/Ni trilayer structure.

A further enhancement of 7 Oe in ΔH_0 value for YIG in the trilayer structure is due to little enhancement of strain, defects, etc. across the YIG top surface of film when Ta and Ni films deposited on top of it. The enhancement in the value of effective Gilbert damping

signifies the amplitude of magnetization precession in the FM layer and is a direct consequence of spin-pumping induced broadening. The linewidth (ΔH) enhancement is a consequence of spin pumping. The coupling that transfers angular momentum from YIG to HM (Ta) metal and then to antiferromagnet adds to the damping of the precessing YIG magnetization, thus increasing (ΔH) as shown in Fig. 5.4 (B). In order to accurately determine the enhancement of Gilbert damping, we measure the frequency dependencies of (ΔH) for all the samples. In all cases, the linewidth increases linearly with frequency. The Gilbert damping constant (α) and zero-frequency linewidth (ΔH_0) can be obtained using eq. (5.2). The Gilbert damping constant and zero-frequency linewidth were retrieved from Fig. 5.4 using the fitting to eq. (5.2).

5.4.4 Spin pumping effect in heterostructures

The α_{eff} is the sum total of the experimentally measured damping parameter, that contain the intrinsic damping (α_{int}) of the FM layer and the contribution arising from spin pumping. α_{eff} can be expressed as;

$$\alpha_{eff} = \alpha_{int} + \alpha_{sp} \tag{5.3}$$

We have derived α_{sp} (Ta) each for YIG and Ni from Fig. 4 (B) and (C) respectively. To do this we have used the single layer YIG and Ni films as the intrinsic Gilbert damping and then extracting the spin pumping contribution from the effective Gilbert damping arising from the YIG/Ta interface and the Ta/Ni interface. The value of Gilbert damping for a single layer YIG is found to be 1.35×10^{-3}, whereas the effective Gilbert damping for YIG in the trilayer YIG/Ta/Ni structure is 1.45×10^{-3}. Hence the α_{sp} (Ta) for YIG is found to be 0.10×10^{-3}. Similarly, we have calculated the Gilbert damping for a single layer Ni film of 20 nm thick as 4.28×10^{-2}. The effective Gilbert damping for Ni from the YIG/Ta/Ni structure is observed as 5.28×10^{-2}. Hence the α_{sp} (Ta) for Ni is found to be 1.0×10^{-2}. Hence, the enhancement of Gilbert damping due to spin pumping effect is 7.4

% for YIG and 23.36 % for metallic Ni film. This large increase of Gilbert damping due to spin pumping in metallic Ni film indicates a larger transfer of spin angular momentum out of the precessing Ni film through its interface with the adjacent Ta layer. Hence it is confirmed that a faster relaxation of precession in Ni as compared to YIG in the 4 nm thick Ta layer, which can be denoted as in decoupled regime. The slight variation in the values of the spin-mixing conductance in comparison with earlier work [76] may be due to several sources like the deposition conditions, the interface quality, and even the measurement technique employed.

The enhancement of effective Gilbert damping is the result of the spin current those leaks out of the ferromagnetic layers and dissipates into the HM layer via the process of spin-flip mechanism. The process of spin current transfer can travel a distance greater than the spin-diffusion length (λ_{sd}) of the HM layer. But when the thickness of the HM was made to be less than the spin diffusion length, there will be spin accumulation at the FM/HM interface, that leads to a spin backflow of current into the FM layer. Therefore, the total spin current accumulation at the FM/HM interface will be the sum total current due to spin pumping FM→HM, represented by I_{pumps} and current due to spin backflow HM→FM, which is represented by I_{backs}. But in a trilayer systems, $FM_1/HM/FM_2$, there will be spin backflow current from two interfaces, viz. FM_1→HM and also FM_2→HM. The intrinsic spin-mixing conductance ($g_{int}^{\uparrow\downarrow} = \pi r^2$) of a FM/HM interface the transfer of spin angular momentum from the FM to the NM layer experimentally measurable effective Gilbert damping parameter is given as follows:

$$\alpha_{sp} = g_{int}^{\uparrow\downarrow} \frac{g\mu_B(1 - e^{(-t_{NM})/\lambda_{sd}})}{4\pi M_s t_{FM}} \tag{5.4}$$

where all symbols hold their usual meaning. In addition, in a trilayer system like YIG/Ta/Ni, it is assumed that each FM layers act as a perfect spin sink. The intrinsic spin-mixing conductance which is the real part of the complex spin-mixing conductance ($g_{eff}^{\uparrow\downarrow}$)

provides the dominant contribution to in a nonmagnetic metallic spacer. We have derived the LHS of Eq. (5.3), α_{sp} from the effective Gilbert damping α_{eff}. The spin mixing conductance g observed to be higher in metallic ferromagnets Ta/Ni in comparison to insulating YIG/Ta due to several mechanisms, such as:

(i) conduction electrons in metallic ferromagnets can directly engage in spin exchange at the interface with a heavy metal (ii) spin current injection and involvement in metallic ferromagnets form Ohmic contacts with adjacent heavy metals (iii) Additional scattering and impedance begin to play an important role in YIG, which is an insulating ferrimagnet, that depends on magnon-mediated spin transport (iv) A strong interfacial spin-orbit coupling appears in metallic ferromagnets, that enhance spin pumping (v) There are spin memory loss in insulating interfaces like YIG/Ta.

The spin mixing conductance ($g_{\uparrow\downarrow}$) was determined from the damping constant of all the samples under investigation and can be written as [54, 271-272]

$$g_{\uparrow\downarrow} = \frac{4\pi M_s t_F}{g\mu_B}(\alpha_{YIG/NM} - \alpha_{YIG}) \tag{5.5}$$

Where M_s is the saturation magnetization, t_F is the thickness of normal metal (NM), g and μ_B are the Lande' factor and Bohr magneton, respectively. The calculated spin mixing conductance for YIG was found to be 1.39×10^{17} m^{-2} for YIG/Ta/Ni, which is close to earlier reported work [76]. Similarly, the spin mixing conductance $g^{\uparrow\downarrow}$ for Ni was found to be $1.17 \times 10^{18} \pm 0.05 \times 10^{18}$ m^{-2}. Hence, it is confirmed that spin mixing conductance $g^{\uparrow\downarrow}$ is higher for metallic ferromagnet like Ni by an order of magnitude than the insulating ferrimagnet like YIG. This is due to several physical mechanisms. (i) Through direct electron exchange there is participation of conduction electrons of Ni in spin exchange at the Ta/Ni interface, hence efficient spin current flow to Ta layer. (ii) Further through interfacial transparency there are better spin current injection and absorption in metallic Ni as it makes an Ohmic contact to Ti layer. On the contrary, YIG being an insulator rely

only on magnon-mediated spin transport. (iii) Further, for Ni with stronger interfacial spin-orbit coupling there is enhancement of spin pumping.

For an insulating ferrimagnet like YIG, thermal magnon-mediated unity spin-current transmission refers to the efficient transfer of spin information, without a corresponding charge current, through the excitation and propagation of magnons (quanta of spin waves) driven by thermal gradients. This phenomenon is particularly relevant in spin caloritronic and spintronics, where it can be harnessed for energy conversion and information processing. Unity spin-current transmission implies that a large portion, ideally all, of the spin current generated by one material can be effectively transferred to another material. In magnon-mediated transmission, the magnons excited in the source material propagate and then transfer their spin information to the adjacent material, potentially through various mechanisms like magnon-electron interactions or direct exchange coupling.

YIG/Ta interface: This indicates the transfer of spins both from YIG and Ni to the heavy metal Ta due to spin-pumping effect. Spin pumping in YIG/Ta in the YIG/Ta/Ni heterostructure refers to the generation of a spin current in the heavy metal layer when the magnetization of the YIG layer precesses at FMR field of 2.45 kOe at an applied microwave frequency of 10GHz. As YIG is a ferrimagnetic insulator with low Gilbert damping and a relatively narrow ferromagnetic resonance linewidth, it allows for efficient magnetization precession with relatively low microwave power. Being an insulator, YIG doesn't allow for direct injection of spin-polarized electrons, making spin pumping the dominant mechanism for spin current generation at the YIG/Ta interface due to strong spin-orbit coupling in Ta. This strong spin-orbit coupling allows for the conversion of the spin current (spin angular momentum) into a charge current via the Inverse Spin Hall Effect (ISHE). The efficiency of spin pumping is quantified by the spin mixing conductance ($g^{\uparrow\downarrow}$), which represents the probability of transferring spin angular momentum across the interface.

Ta/Ni interface: Similarly, in the Ni/Ta interface of the YIG/Ta/Ni heterostructure due to magnetization precession in the ferromagnetic Nickel layer generates a pure spin current that flows into the adjacent heavy metal Ta. This spin current is a result of the magnetic dipole interaction at the interface between the two materials. The HM layer then converts this spin current into a voltage via the inverse spin Hall effect (ISHE). The oscillating spin polarization at the HM/Ni interface injects a spin current into the HM layer. This process is analogous to charge pumping in nanostructures, but it occurs at room temperature and is a more robust phenomenon. The spin current is proportional to the precession frequency and the strength of the magnetic interaction at the interface. The quality of the Ni/HM interface plays a crucial role. Roughness or impurities can affect the spin current and its conversion. The spin Hall angle and spin diffusion length of the HM layer are important factors in determining the efficiency of spin current conversion to charge current.

FM_1/HM/FM_2 interfaces: The spacer layer Ta has two different interfaces. Therefore, for a trilayer system of YIG/Ta/Ni with a thin Ta layer, at 10 GHz applied frequency, the spin current generated by magnetization precession of Ni layer will pass through the Ta spacer at a smaller magnetic field of 1.86 kOe and enter the YIG layer. On the other hand, at the same 10 GHz applied frequency spin current generated by magnetization precession of YIG layer will pass through the Ta spacer at a higher magnetic field of 2.63 kOe and enter the Ni layer. This process makes the two FM layers of Ni and YIG can sense each other through the Ta layer by exchanging the nonequilibrium spin currents. This is important to mention here that as the spin current generation are taking place at much different field values, there will be no cancellation of spin current. There will be only accumulation of spins in the Ta spacer layer. And hence there will be spin-momentum brake because of the dynamic coupling between YIG and Ni layers. Hence, there will be an enhancement of effective Gilbert damping of the tri-layer system by spin pumping.

FM/HM/AFM; Further, after oxidizing the top Ni layer to NiO resulted in a FM/HM/AFM (YIG/Ta/NiO) trilayers. As Ni after 100% oxidation transformed to an antiferromagnet NiO, therefore, Ni peak vanished due to the formation of antiferromagnetic NiO. It is noted that the ferromagnetic resonance field (H_r) values do not change for all three samples. This is a clear indication that the magnetization of the YIG layer is unaffected for all three structures. For trilayer structure YIG/Ta/Ni due to the presence of Ta inter-layer there is a slight broadening of YIG peak.

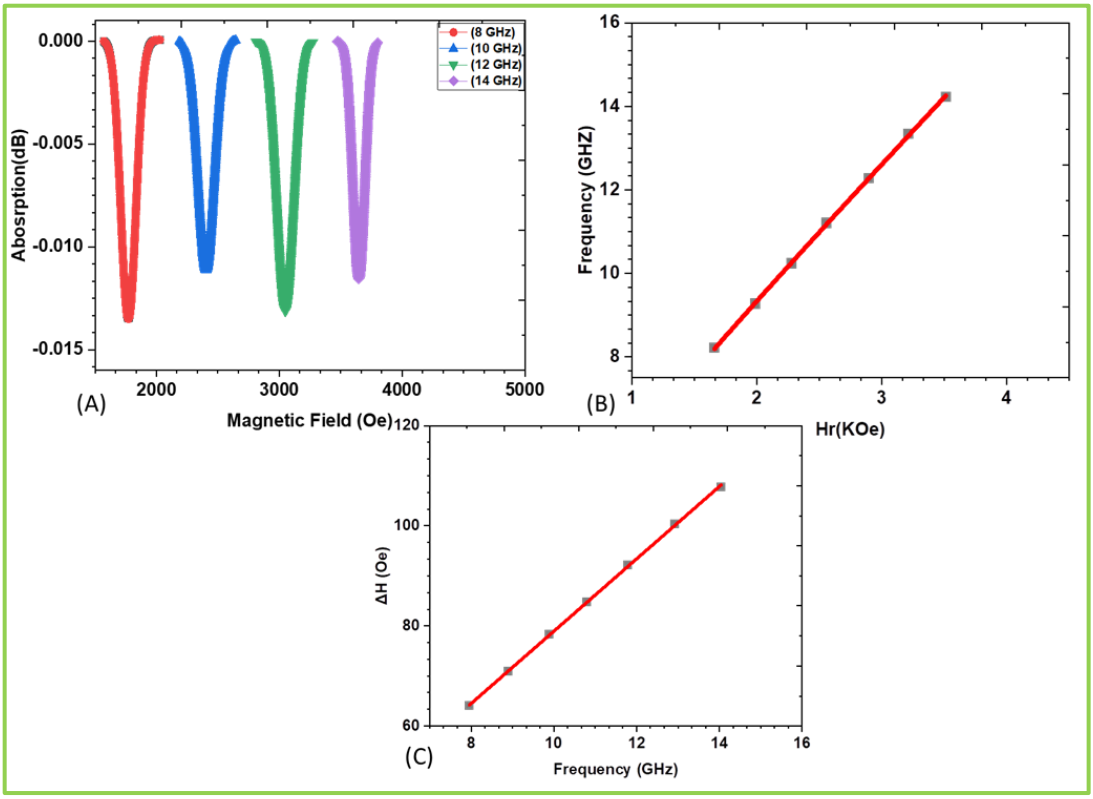

Fig. 5.8: (A) FMR spectra of YIG in YIG/Ta/NiO structure. (B) show the resonance fields (Hr) and (C) FMR linewidth derived by Lorentzian fits

Fig. 5.8 (A) reveals the ferromagnetic resonance (FMR) spectra of trilayer FM/HM/AF heterostructures of YIG/Ta/NiO. Interestingly, for YIG/Ta/NiO structures we have observed a two-fold broadening of YIG peak. In this investigation, the value of intrinsic Gilbert damping for a single layer YIG is found to be 1.35×10^{-3}. In the YIG/Ta/Ni

trilayers structure the effective Gilbert damping for YIG increased to 1.45×10^{-3}. The solid lines to Fig. 5.8 (B) are the fitted lines to the experimental data points.

This increase has been assigned to the spin pumping effect as YIG is interfaced to a heavy metal Ta and hence there is an enhancement of Gilbert damping for YIG α_{sp} (Ta)=0.10×10^{-3}. After conversion of Ni to antiferromagnetic NiO the effective Gilbert damping for YIG is found to be 1.57×10^{-3}, which is about 16% increase from its intrinsic value.

Fig. 5.8 (C) depicts the dependence of the FMR linewidths (ΔH) of the YIG after the conversion of Ni to NiO. This two-fold broadening of YIG resonance linewidth may be due to the presence of an antiferromagnetic (AF) NiO top layer. This is detected as an increase in the linewidth of the ferromagnetic resonance (FMR) spectra. This indicates the transfer of angular momentum from YIG to the heavy metal Ta-accompanied with spin back-flow from the antiferromagnetic NiO top layer. We would like to explain in the following way:

In a YIG/Ta/NiO trilayers system, when the spin polarized current reaches the Ta/NiO interface, a certain portion of the spin current reflected back into Ta layer due to the spin backflow process driven by spin accumulation. The ferromagnetic YIG layer acts as a source and the probe for the for-spin current which is the source pumped into the Ta thin layer. Since there is negligible spin dissipation in the Ta spacer, the backflow spin-current contribution to spin pumping induced Gilbert damping can be measured via FMR linewidth of YIG layer. Considering spin relaxation in Ta layer to be negligibly small, the spin-pumping current is reflected at the Ta-NiO interface and returns back to Ta layer.

In YIG the spin polarization is so strong that spin accumulation can be neglected. In insulating NiO layer spin accumulation and spin polarization by the localized moments can be possible. Ta layer can inject spin into the NiO layer via dynamic exchange

coupling. Due to limited magnon diffusion length inside an insulator the enhancement of damping is relatively high.

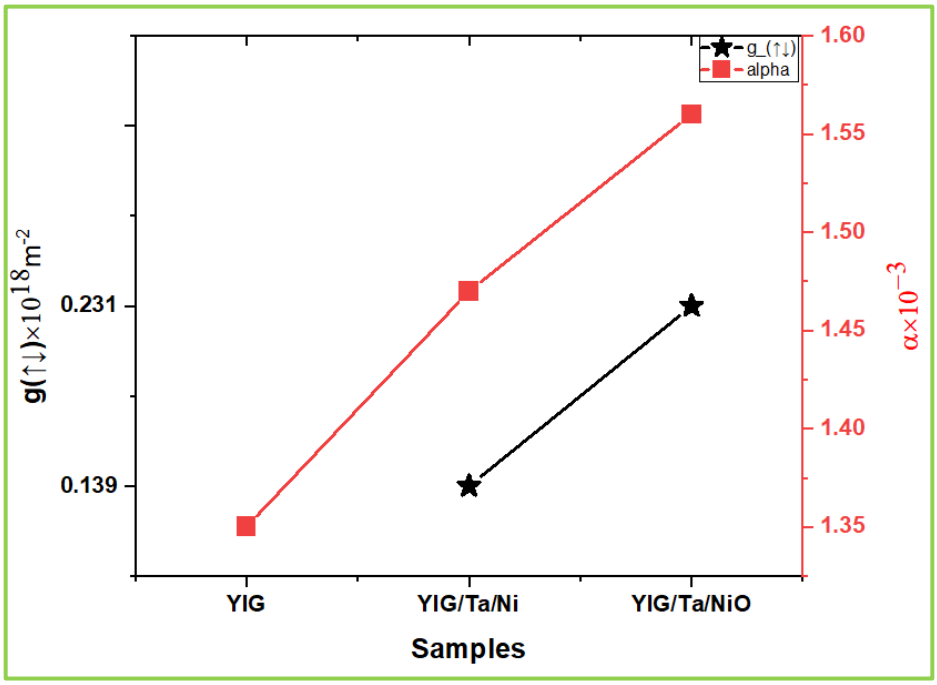

Fig. 5.9: (Left panel) Gilbert damping of YIG in (i) single layer (ii) in trilayers of YIG/Ta/Ni and (iii) in YIG/Ti/NiO. (Right Panel) Spin mixing conductance ($g_{\uparrow\downarrow}$) in (i) in trilayers of YIG/Ta/Ni and (ii) in YIG/Ti/NiO.

To explain the enhancement of Gilbert damping as well as spin mixing conductance for the YIG/Ta/NiO trilayers to YIG/Ta/Ni trilayers, as shown in Fig. 5.9. The spin-pumping mediated Gilbert damping (α_{sp}) was calculated as 1.0 $\times 10^{-4}$ and 2.2 $\times 10^{-4}$ for YIG/Ta/Ni and YIG/Ta/NiO trilayers (i.e., ~100% increment), respectively. Hence there is a considerable enhancement of spin mixing conductance of YIG from $1.39 \times 10^{17} \pm 0.10 \times 10^{17}$ m^{-2} for YIG/Ta/Ni trilayer to $2.31 \times 10^{17} \pm 0.16 \times 10^{17}$ m^{-2} for the YIG/Ta/NiO trilayer.

At FMR, the oscillating magnetization of YIG transfers spin angular momentum to spin polarized electrons of the adjacent Ta layer. Linewidth broadening of the YIG layer occurs due to the loss of spin angular momentum. For YIG/Ta interface, this method exhibits an increase of spin mixing conductance depending on the YIG/Ta interface as spins may entirely absorbed or scattered backs into the YIG layer. In this investigation, we investigate the spin dependent transport in Ta and AFM NiO using the spin pumping technique.

Around the total effective field due to the spin pumping effect, YIG generate pure spin polarized current when oscillating at FMR. The spin current diffuses through YIG/Ta/NiO trilayers. Due to spin dependent scattering, it is absorbed or reflected at the YIG/Ta and Ta/NiO interfaces and hence affects the YIG effective Gilbert damping: $\alpha = \alpha^0 + \alpha^{pump}$. Here α^0 is the intrinsic YIG layer's damping and α^{pump} is the additional non-local damping. For the paramagnetic Ta, $\alpha_{sat}{}^{pump}$ is mostly related to spin flipping that is bulk-like. In contrast, for the YIG, $\alpha_{sat}{}^{pump}$ mostly relates to the effective spin mixing conductance ($g_{eff}^{\uparrow\downarrow}$) that mostly depends on the Ta/NiO interface ($g_{Ta/NiO}^{\uparrow\downarrow}$). Hence, there is an increase of spin mixing conductance for YIG/Ta/NiO system, in comparison to YIG/Ta/Ni system.

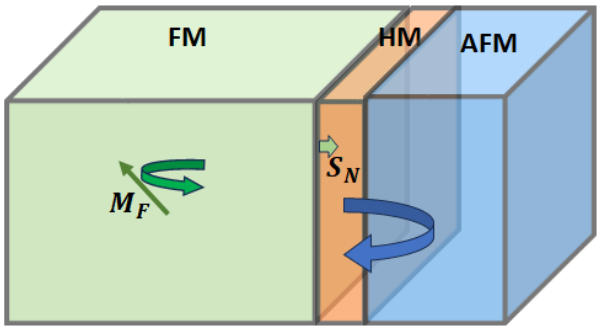

Fig. 5.10: Representation of spin flow in FM/NM/AFM layer.

In YIG/Ta/NiO spin transport via FM-NM-AFM is shown as depicted in in Fig. 5.10.

Here, we considered a heterostructure consisting of FM and AFM layers with thickness d_1 and d_2 ($d_1 > d_2$), separated by a NM spacer layer. The thickness of NM layer (4 nm) is higher than the spin diffusion length of Ta. Therefore, Ta cannot conserve the polarization of the spin sink within λ_{sd}, and thus does affect the Gilbert damping. [267]. These results suggest the following multistage spin transport in YIG/Ta/NiO thin films: (1) at the YIG/Ta interface, the precessing YIG magnetization transfers angular momentum to the conduction electrons in the metal, (2) the spin current in Ta propagates to the Ta/NiO interface where it is converted to antiferromagnetic excitations leading to enhance spin transport [76]. These results suggest a new path toward high-efficiency spin transport by engineering heterostructures.

5.5 Conclusions

In conclusion, we report the effect of oxidation of Ni to NiO in YIG/Ta/NiO heterostructure to measure the spin transport. The proposed heterostructures explored confirmed that spin mixing conductance $g^{\uparrow\downarrow}$ is higher for metallic ferromagnet like Ni by an order of magnitude than the insulating ferrimagnet like YIG. The significant enhancement of linewidth indicates excellent spin conversion efficiency at the YIG/Ta and Ta/NiO interfaces. Transition from Ni to antiferromagnetic NiO layer by oxidation results in robust spin transport in NiO mediated by antiferromagnetic magnons and spin fluctuations. These results suggest a new path to examine the prevalence of a favorable interface for the effective spin backflow and spin memory loss.

Chapter 6

Spin Transport and Interfacial Dynamics in YIG-Based Multilayer Thin Films

Ferromagnetic Resonance (FMR) based spin pumping serves as a powerful technique to quantify the spin mixing conductance of ferromagnet-noble metal based heterostructure. In this study we present the non-magnetic metal mediated spin pumping study in the epitaxial grown YIG- based multilayer thin films. Spin transport efficiency in heterostructures determined by the spin conductance of each constituent and their transparency at interfaces, which combinedly control the flow and conversion of spin currents. We report the comparative investigation of YIG/Pt, YIG/Cu/Pt, YIG/Cu/W, YIG/Cu/W/Pt and YIG/Cu/Pt/W multilayer, emphasizing the influence of non-magnetic and noble metal on spin current transmission at room temperature due to considerably enhanced spin mixing conductance at the interfaces. The surface morphological and structural properties were investigated using Atomic Force Microscopy, X-ray diffraction and Raman spectroscopy. The magnetic properties demonstrate increase in the coercivity and decrease in saturation magnetization after the deposition of non- magnetic metallic layer on YIG. Whereas, the ferromagnetic resonance measurements reveal broadening of the line width of ferromagnetic resonance indicates the significant spin transfer to the non-magnetic metal layer. The parameters like gilbert damping, zero frequency linewidth and mixing conductance retrieved from the fitting indicates considerable change with the different metallic film. These studies provide an alternative path towards next generation magnetic switching devices.

6.1Introduction

Traditional electronic devices work on the movement of electrical charges. By contrast, the spin and charge current decoupling realized through ferromagnetic resonance (FMR)-

driven spin pumping offers a route toward low energy, high-efficiency spintronics technologies, with profound implication for future computing [274, 275] and worldwide energy sustainability [271]. Spin pumping is given as the transfer of electron spins from a ferromagnet (FM) layer to a neighbouring non-magnetic metal in an FM/NM structure under the magnetic precession [8, 40, 276]. In this type of system, a time oscillating magnetization produces a pure spin current in the nonmagnetic layer. This phenomenon has been demonstrated experimentally with the different excitation sources spanning from GHz to THz frequencies range [277-279]. Spin pumping efficiency is characterised by the extent of spin angular momentum transfer [279], which is measured by the interfacial spin mixing conductance [280-281]. Notably, such efficiency is strongly sensitive to the interfacial properties of the NM in contact with the FM [282] or a ferromagnetic insulator [271]. As a result, enormous theoretical and experimental efforts have been made to understand how to excite, detect, and manipulate magnetization dynamics and spin current transport in such heterostructures [283]. Efficiency of spin pumping is primarily governed by the interfacial spin mixing conductance ($g\uparrow\downarrow$) of the FM/NM junctions [284]. Yttrium Iron Garnet (YIG, $Y_3Fe_5O_{12}$) is one of the most important magnetic insulator materials for the spin transport studies. It is emerged as a model system for transport studies. This is primarily attributed to its ultra-low gilbert damping and exceptionally long spin wave propagation length [285-290]. It also has high Curie temperature (560 K), which makes it suitable for the applications in the field of spintronics, magnonics and microwave passive and active devices [166-171]. Usually, non-magnetic metal layer (NM) is selected to serve as the spin sink e.g Pt, W or Ta, because of their strong spin hall effect (ISHE), whereas lighter non-magnetic metal such as Cu are rarely utilized because of their poor spin orbit coupling. A wide range of FM/NM or FM/NM1/NM2 heterostructures have been extensively investigated by both spin Seeback measurements [63, 291] and FMR spin pumping [292-298]. Quantitative understanding of the spin transmissivity of multilayer heterostructures is important for using intervening layers to maximize spin transport characteristics. Experimental and

theoretical work on spin pumping predict that its efficiency depends on the various factor like spin orbit coupling in the nonmagnetic (NM) layer, interface quality and the presence of magnetic anisotropy in the FM Layer. For example, Cu interlayers have recently been used to quash the proximity-induced ferromagnetism in YIG/Pt systems [63–66]. Yet, a systematic quantitative understanding of spin current generation and conduction in YIG/Cu/NM and YIG/Cu/NM_1/NM_2 heterostructures of spin current generation and conduction in YIG/Cu and YIG/Cu/NM heterostructure, interestingly the role of spin mixing conductance at each interface, is still need to study which is lacking. In the current work, we discuss the effect of interface on the spin transport in the heterostructure by depositing the FM/NM_1, FM/Cu/NM_1, FM/Cu/NM_2, FM/Cu/NM_1/NM_2 and FM/Cu/NM_2/NM_1. The XRD scan together with Raman measurement confirm the successful formation of heterostructures on YIG. Using the atomic Force Microscope (AFM) surface morphology was examined and also the root mean square (RMS) roughness value was measured. Broadband Ferromagnetic resonance spectrometer (FMR) measurements were performed to examine the damping parameters of heterostructures. In addition, the spin mixing conductance was determined, and significant change was observed.

6.2 Experimental procedure

YIG thin films were deposited on single-crystalline GGG (111) substrates (MTI Corporation, Richmond, USA) by the pulsed laser deposition (PLD) technique. Substrates and vacuum chamber were cleaned properly before the deposition in order to have high quality thin film. Chamber were cleaned using the isopropanol to maintain the high vacuum pressure and avoid the contamination. Whereas substrates were cleaned thoroughly by sonication using the isopropanol and acetone to remove the impurities and contamination. A 248 nm KrF excimer laser with a 10 Hz pulse rate was used to ablate the material from the target at 300 mJ energy for the deposition of high quality YIG thin films. Turbo molecular pump was used to maintain the base pressure of chamber at mbar. Distance between the substrate and target was fixed at 4 cm. Substrates were preheated to 800 °C

prior to deposition in order to remove any contaminants or surface impurities. The deposition was carried out at 800 °C in the presence of 0.15 mbar of oxygen pressure. The films were deposited at the rate of ~ 0.6 Å/sec. The as grown thin films were annealed in-situ for two hours at the deposition temperature of 800 °C in the presence of 0.15 mbar oxygen pressure and then cooled down to room temperature in the same oxygen pressure throughout the process. Ultra-thin film of nonmagnetic metals like Pt, Cu, W were deposited on YIG film using the RF and DC sputtering system. DC/RF magnetron sputtering technique was used for the deposition of Copper (Cu), platinum (Pt) and tungsten (W) on the YIG film of 3 mm X 5 mm dimension. The deposition was carried out using a high purity (99.99%) Cu, Pt and W targets of 2 inch in diameter and 1mm in thickness. The sputtering process was carried out in chamber which was fitted with TMP to achieve the ultra-vacuum of the order of 10^{-8} KPa for the deposition. Deposition of all normal metals (Cu, Pt and W) was carried out at the 300°C and distance between the substrate and the target was maintained at 13 cm during the course of deposition, Pt was deposited using 0.02 A current, deposition rate of 1.1 Å/s as measured with the in-situ thickness monitor, Cu was deposited by using the 30 W power at deposition rate of 1.8 Å/s whereas, W was deposited using the same power at deposition rate of 2.4 Å/s, working pressure of 3.26×10^{-4} kPa was maintained during the deposition of all metallic samples by providing high purity inert gas (argon) in to the deposition chamber by means of MFC (mass flow controller). Series of five samples YIG/Pt, YIG/Cu/Pt, YIG/Cu/W, YIG/Cu/Pt/W and YIG/Cu/W/Pt were deposited using the sputtering technique. Films thickness was optimised by different deposition parameters and measured by using the lithography and atomic force microscope (AFM) technique. The thickness of YIG film was 90 nm. Thickness of the Copper (Cu) in all the samples were fixed 2.5 nm. Thickness of the Platinum (Pt) in first sample YIG/Pt and second sample YIG/Cu/Pt was 5 nm, where as in the fourth (YIG/Cu/Pt/W) and fifth (YIG/Cu/W/Pt) samples were fixed at 2.5 nm. The thickness of tungsten (W) in third sample was 5 nm whereas in fourth and fifth samples were fixed at 2.5 nm. We have deposited the bilayer, tri layer and tetra layer of structures. Used the Cu as spacer between

the noble/heavy nonmagnetic metals platinum (Pt) and tungsten (W) because Cu have long spin diffusion length and very good spin conductor and it facilitates the transport of pure spin currents without significant loss can cause increase in Gilbert damping due to strong spin-orbit coupling [82, 298].

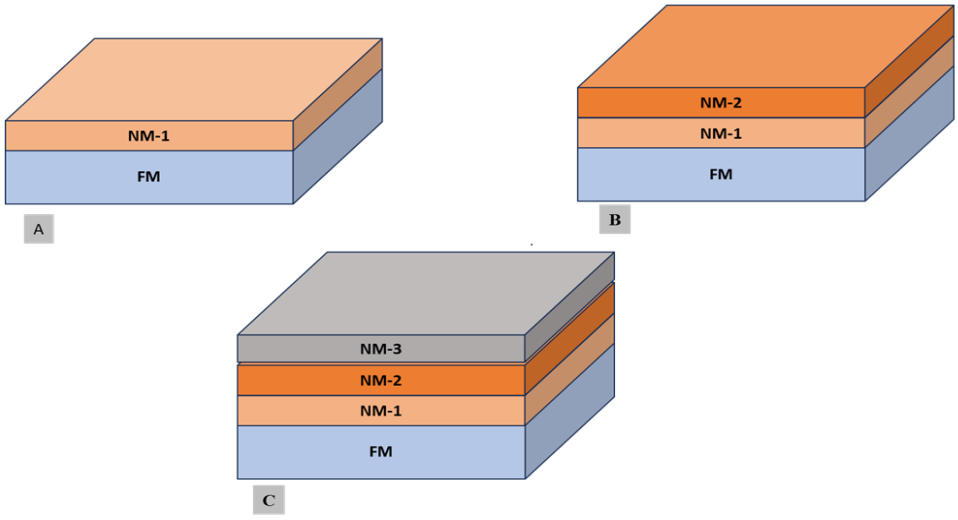

Fig. 6.1: (A), (B) and (C) Schematic of Investigated Heterostructures

The X-ray diffraction pattern of thin magnetic films was performed using the X'Pert PRO PANalytical diffractometer. This diffractometer is equipped with a Cu–Kα of wavelength 1.54 Å and lower grazing angle of incidence. Phase development of films was also measured by Raman spectroscopy (WITec alpha 300 RA) at a resolution of 1 cm^{-1}. 532 nm of laser wavelength, spectrophotometer grating of 600g/mm, integration time of 2 s, 20 accumulations and very low laser power was used for Raman measurement of the samples. The magnetic measurement of the samples was carried out using the J3120 model of Cryogenic Limited, UK made physical properties measurement system equipped with the vibrating sample magnetometry (VSM) technique. The dc magnetic measurements were performed at room temperature (300K) with the VSM probe by using a magnetic field applied in the in- plane direction of films geometry. The samples were inserted inside the pickup coil of the magnet with the help of nonmagnetic capsule and Kapton tape. At the time of measurement vibrator was vibrating at constant frequency of 20 Hz, cantering

of the samples were carried out with the applied field of 100 Oe. The paramagnetic contribution of the substrates was properly subtracted. WITec, GMBH make WITec alpha 300 RA atomic force microscope equipment was used to check the quality and the roughness of thin films. AFM measurements were carried out in ac mode (tapping mode) by using the non-contact cantilever with high resonant frequency (250 KHz), low force constant (45 N/m), coated with Au at reflective side, tip height 14-16 µm, cantilever length 125 µm, thickness 3.5-4.5 µm, and tip curvature radius was few nanometres. The detailed magnetization dynamics of films were performed using the vector network analyser based broadband ferromagnetic resonance (FMR) spectroscopy. "S" shaped coplanar waveguide (CPW) was used with the film in flip chip configuration on the CPW, both ends of the waveguide connected to the ports of VNA. The coplanar waveguide (CPW) for measurement of this experiment was fabricated on a copper-clad RT/duroid® 5870 laminates, a high-frequency dielectric substrate. The signal line was formed with a width of 1mm, isolated from the ground planes by a defined gap. This required configuration ensured the characteristics impedances of 50 Ω for transmission line applications. The applied dc magnetic field on film plane was perpendicular to the high-frequency magnetic field (h_{RF}). The measurements were carried out in the field sweep mode at various frequencies varied from lowest measured frequency 8 GHz to the highest frequency 20 GHz. The acquired FMR spectra were fitted with Gaussian function to extract the resonance field line width and resonance field.

6.3 Result and Discussion

6.3.1 Structural characterisation of multilayer thin films using XRD and Raman spectroscopy

The X-Ray diffraction and Raman techniques were used to measure the structure properties of all the deposited films. Fig. 6.2(A) represents the x-ray diffraction output of YIG/Pt, YIG/Cu/Pt, YIG/Cu/W, YIG/Cu/Pt/W and YIG/Cu/W/Pt films which confirmed

the deposition of multilayer film and creation of heterostructures. Single crystalline nature of the YIG observed on GGG (111) substrates, besides the YIG other non-magnetic metal (NM) also showed the sharp peak at 2θ angle of 43.22°, 39.82° and 40.1° for the Cu (111) plane, Pt (111) plane and W (110) plane respectively [299-301]. X-ray diffraction data of all samples confirmed the formation of desired heterostructures. Fig. 6.2(B) shows the Raman spectroscopy data of heterostructures. The presence of Pristine YIG was further confirmed from the Raman spectroscopy characterisation while no additional peaks were observed for NM deposited samples confirmed the deposition of metallic layer over YIG.

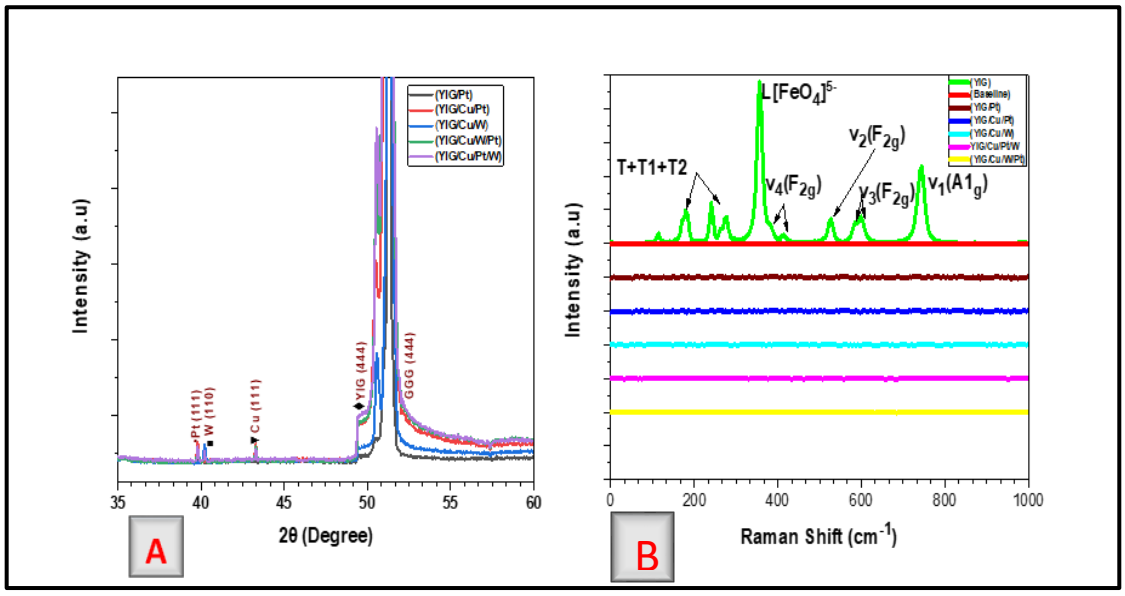

Fig. 6.2: (A) XRD data of complete set of samples deposited over YIG (B) Raman Data of all the Samples grown for multilayer

The Raman peaks of YIG can be seen from the spectroscopic data around 168, 180, 235, 269, 381, 415, 485, 580, and 600 cm^{-1}, respectively [196]. The major peak at 269 cm^{-1} which demonstrate $L[FeO_4]^{5-}$ translational modes, which is related with ferromagnetic nature. GaO_4 and GaO_6 which represents internal vibrations in substrates (GGG) are linked to the A_{1g} modes at Raman spectroscopy peaks of 355 and 741 cm^{-1}, respectively

[197]. None of the peak was observed for Cu, Pt and W for deposited samples in the heterostructures due to its metallic nature [302].

37

6.3.2 Interface study of thin films using atomic force microscopy

Furthermore, atomic force microscopy (AFM) was used to measure the roughness value of the films. Roughness of the films plays a crucial role in magnetization dynamics because higher roughness of the structures promotes the generation of the two magnon scattering. Fig. 6.3 (A) –(F) represents the 3D images generated through atomic force microscope (AFM) data for pristine (YIG), heterostructures samples YIG/Pt YIG/Cu/Pt, YIG/Cu/W, YIG/Cu/Pt/W and YIG/Cu/W/Pt respectively.

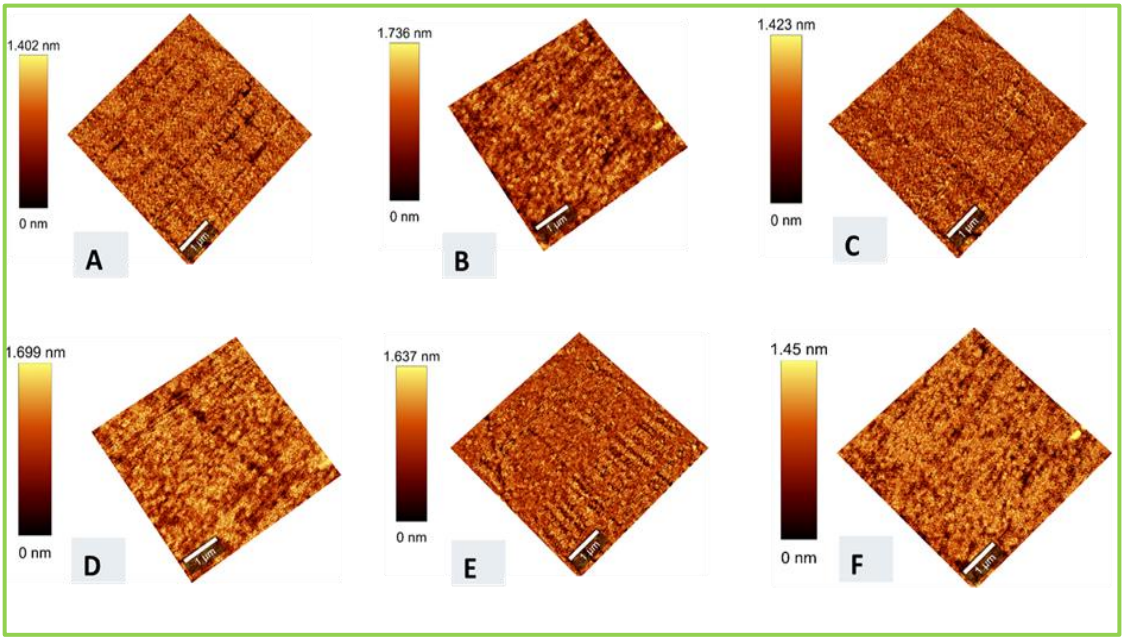

Fig. 6.3: (A) to (F) AFM images of all set of samples analysed in heterostructures.

From the AFM data it was observed that the root mean square (RMS) value of roughness varied from .26 nm to .46 nm, which is consistent with earlier reported result of heterostructures [82, 299]. RMS value of roughness for all the samples is mentioned in Table 6.1. Fig. 6.4 represents the vibrating sample magnetometry MH data of all the

samples. The schematic diagram of direction of magnetic field which is applied parallel to the plane of sample surface is shown in inset of fig 6.4.

6.3.3 Magnetization study using VSM and FMR

Magnetic measurement done at room temperature with the help of superconductor-based magnet. Magnet temperature was at 4.8 K, first stage at 39 K and second stage was at 4 K. Helium pots temperature was at 4.2 K. The paramagnetic contribution of GGG substrates was subtracted from the raw magnetization (MH) data using a linear background correction. There was not much difference in the saturation magnetization for all the samples of series. The hysteresis loop of all the samples was found to be in square loop structures. It exhibits very less change in the coercivity for all the samples which was measured around 15 ± 3Oe. Due to low value of coercivity YIG Shows the magnificent mellow magnetic nature. The low value of coercivity corelates to the low magnetic nonuniformities in thin films [199].

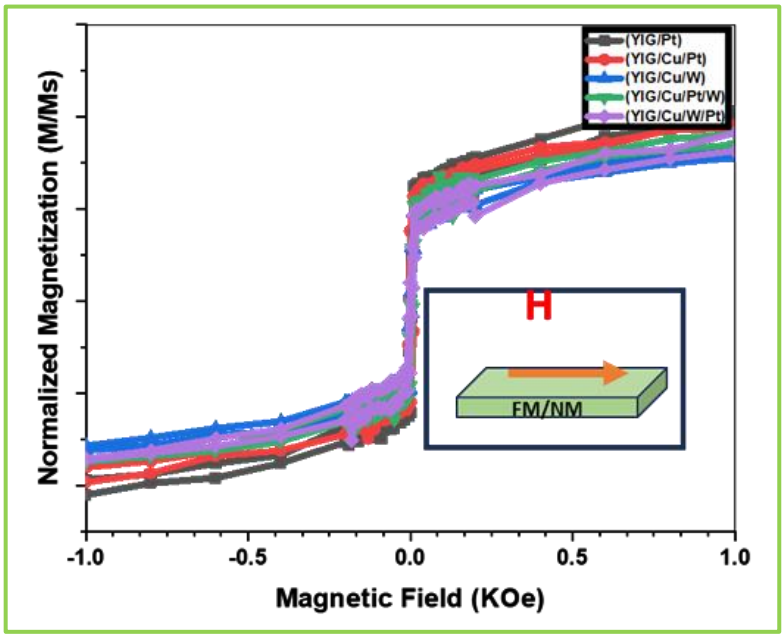

Fig. 6.4: Plot between magnetic moment and applied magnetic field of YIG/Pt/YIG/Cu/Pt, YIG/Cu/W, YIG/Cu/Pt/W and YIG/Cu/W/Pt

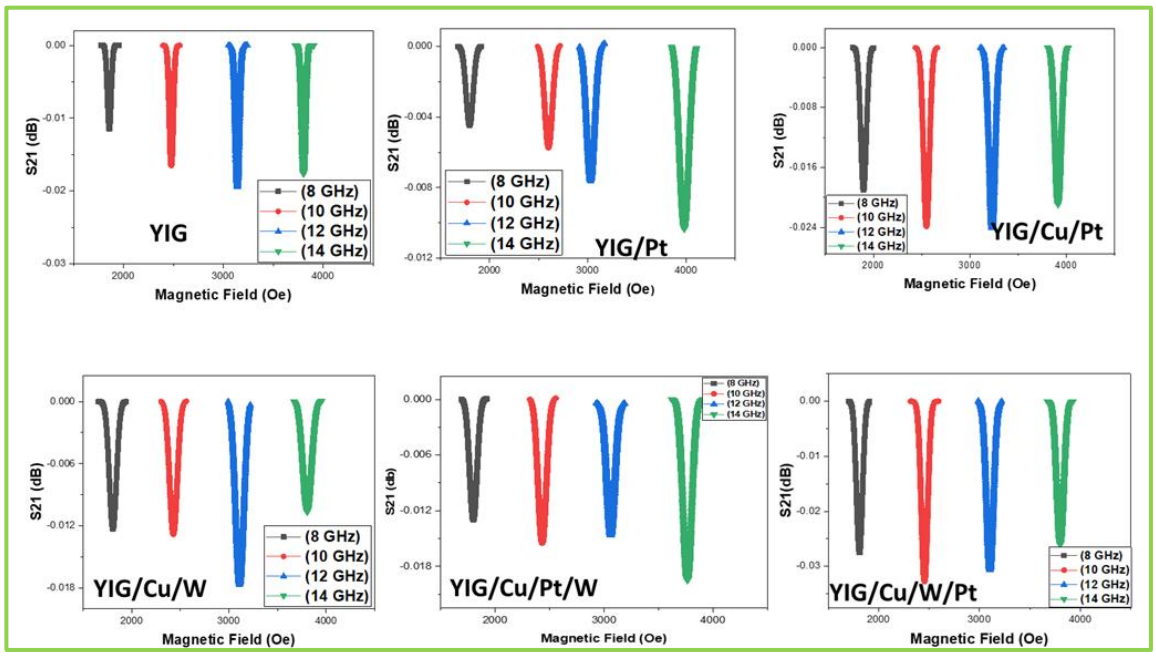

Fig. 6.5: FMR absorption spectra for YIG, YIG/Pt/YIG/Cu/Pt, YIG/Cu/W, YIG/Cu/Pt/W and YIG/Cu/W/Pt

The magnetization of YIG pass on the angular momentum in to the conduction electron in Cu, since the Cu thickness (*t*_{Cu}) is much smaller than the spin diffusion length (λ_{SD}), spin accumulation in the Cu spacer drives a spin current (*J*_s) into the adjacent Pt or W layer, as a outcome of the inverse spin hall effect (ISHE), injected spin current in to the metallic layer Pt or W is converted in to the transverse charge current giving rise to a measurable voltage (*V*_{ISHE}) [82]. The resistance of first sample YIG/Pt measured around .51 KΩ whereas after the insertion of Cu of 2.5 nm as a spacer resistance of second sample YIG/Cu/Pt decreased to around .42 KΩ, resistance of third sample YIG/Cu/W shown in higher side around 7 KΩ, fourth sample YIG/Cu/Pt/W resistance measured about 3.2 KΩ and resistance of fifth sample YIG/Cu/W/Pt reduced to around .45 KΩ.

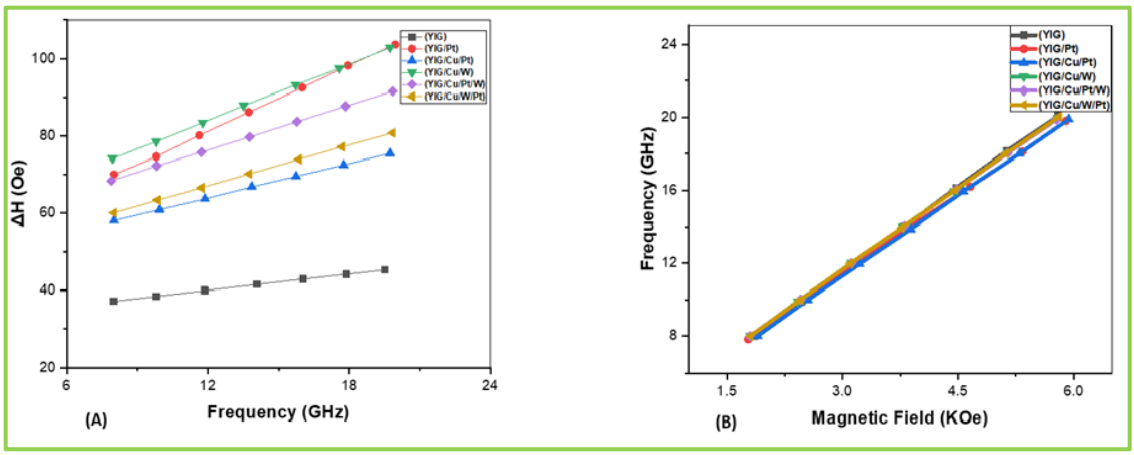

Fig. 6.6: (A) Change in line width with change in frequency for heterostructure (B) Variation of H_r with respect to frequency of multilayer heterostructure

6.3.4 Spin pumping effect in multilayer heterostructure

To encounter the mechanism behind the spin pumping performance of all the bi, tri and tetra layer structures, we require to find out the spin mixing conductance from the enhancement of the Gilbert damping (α) arising from spin pumping. For measurement of damping parameters and magnetisation studies we performed the FMR measurements at room temperature. Fig. 6.5 shows the absorption spectra of all the samples of heterostructures obtained from the FMR measurements. From the FMR data it was observed that the non-magnetic metallic layer relatively affects the effective saturation magnetisation ($4\pi m_{eff}$) in YIG (111), which is tabulated in Table 6.1. Gilbert damping and effective saturation of all the magnetic film was measured by the frequency dependent FMR line width, which is shown in fig. 6.6 (A) and (B).

FMR line width (ΔH) and resonant magnetic field (H_{rf}) was calculated by gaussian fit of the absorption data obtained using FMR in field sweep mode for the different frequency range varies from 8 GHz to 20 GHz. In all samples we found that line width increases linearly with increase in frequency.

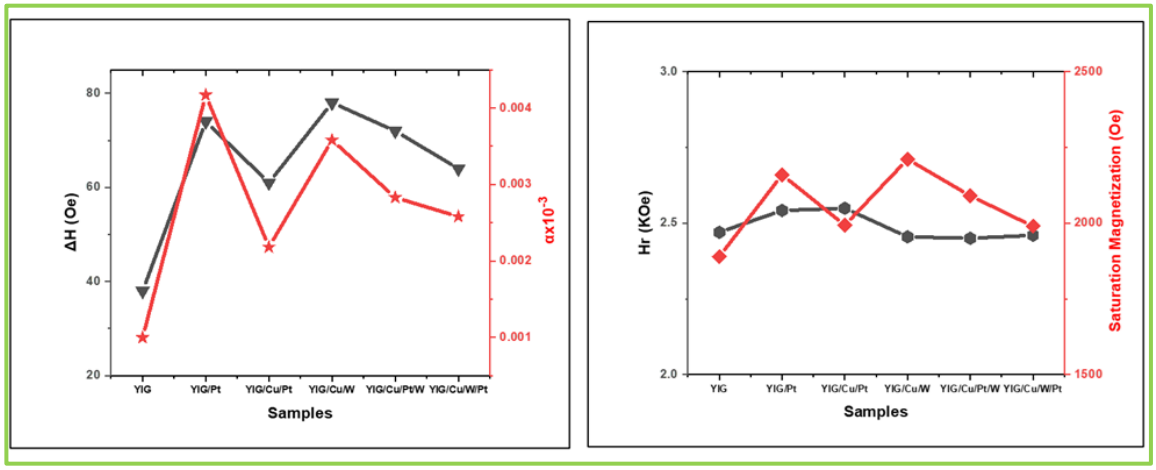

Fig. 6.7: (A) Delta H at 8 GHz with respect to Damping Constant (B) Variation of H_r with saturation magnetization.

The field swept line width is determined by the energy dissipation due to interactions between the magnons and other degree of freedom, i.e., phonon and magnon in the film, and accordingly characterise the intrinsic FMR linewidth [170, 304]. In plane equation of Kittel's written by equation (6.1) [305], effective magnetization field ($\mu 0 M$eff) were calculated using

$$f = \frac{\gamma}{2\pi}\mu_0\sqrt{(H_r)(H_r + M_{eff})} \qquad (6.1)$$

In the above equation $_{\mu 0}M_{\text{eff}}$ is the effective field which is written as $_{\mu 0}$ $(Ms - H_{\text{ani}})$ with anisotropy field $Hani = \frac{2K1}{Ms}$.

Field linewidth and Gilbert damping parameters was measured using the phenomenological equation [205].

$$\Delta H = \Delta H_0 + \frac{4\pi\alpha}{\gamma} f \qquad (6.2)$$

We observed that the linewidth measured at 8 GHz of the YIG/Pt multilayer film was 74 Oe, which reduced to 61 Oe upon the insertion of a Cu spacer layer before the Pt. In contrast, the linewidth for the YIG/Cu/W structure was 78 Oe. For the tetra-layer structure of YIG/Cu/Pt/W, the linewidth was 72 Oe, which is larger than the YIG/Cu/W/Pt structure, which had a linewidth of 64 Oe. Which is in resemblance with previous study on heterostructures of heavy metals YIG/Cu/Pt and YIG/Cu/W [82]. Change in the Gilbert damping constant was also observed which was higher for the YIG/Pt 4.17×10^{-3} and lowest for pristine samples 9.97×10^{-4}, all the value of damping parameters tabulated in Table 6.1. Relation between damping constant and ΔH as well as between the H_r and saturation magnetization is shown in fig. 6.7 (A) and (B) respectively. An increase in the damping constant due is in accordance with the previous study on the multilayer thin film on Py/Cu/Pt, YIG/Cu/Pt, Bi-YIG/Pt and YIG/Pt [48, 65, 299, 305]. Variation in the damping parameters across the samples due to the spin pumping effect. Change in linewidth and damping parameters implies the consequential difference at the interface of multilayer film. The damping enhancement in multilayer due to spin pumping can be expressed as $\alpha_{sp} = \alpha_{YIG/NM} - \alpha_{YIG}$, from this expression higher value of α_{sp} observed for bilayer YIG/Pt, whereas for other samples lower value of α_{sp} observed. Tserkovnyak et al. established a theory for the quantitative analysis of interfacial spin mixing conductance $g_{eff}^{\uparrow\downarrow}$ [284] in metallic FM/NM bilayers, tri layers or tetralayers, where real part of $g^{\uparrow\downarrow} \approx g_{eff}^{\uparrow\downarrow}$ is dominant, whereas recently it has been also reported that the imaginary part of $g^{\uparrow\downarrow} \approx g_{eff}^{\uparrow\downarrow}$ is also insignificantly small [306, 307].

Table-6.1: Parameters obtained from the Atomic Force Microscope (AFM) and Ferromagnetic Resonance Spectroscopy (FMR) measurements

Samples	Roughness (nm)	Effective saturation magnetisation ($4\pi m_{eff}$) in Oe	Damping constant (α)	Spin mixing conductance ($g^{\uparrow\downarrow}$)
YIG	0.26	1890	9.97×10^{-4}	-
YIG/Pt	0.46	2160	4.17×10^{-3}	2.25×10^{18}
YIG/Cu/Pt	0.30	1993	2.28×10^{-3}	1.01×10^{18}
YIG/Cu/W	0.42	2211	3.58×10^{-3}	1.81×10^{18}
YIG/Cu/Pt/W	0.39	2090	2.83×10^{-3}	1.31×10^{18}
YIG/Cu/W/Pt	0.32	1990	2.58×10^{-3}	1.15×10^{18}

So as to understand these behaviours, we require to determine the spin mixing conductance ($g_{eff}^{\uparrow\downarrow}$) of all the samples. Spin pumping influenced gilbert damping enhancement may be expressed as equation (6.3) [284],

$$\alpha_{sp} = \frac{4\pi M_s t_F}{g\mu_B} g_{eff}^{\uparrow\downarrow} \quad (6.3)$$

Where t_F is the thickness of non-magnetic normal metal (NM), M_s is the saturation magnetization, $g_{eff}^{\uparrow\downarrow}$ is the spin mixing conductance at the interface of YIG/NM, which incorporates the spin current backflow propelled by spin accumulation, μ_B and g are the Bohr magneton and Lande' factor, respectively. We calculated the spin mixing conductance provided in Table I for all the samples and it was found that the value of $g^{\uparrow\downarrow}$ is higher 2.25×10^{18} in case of bilayer (YIG/Pt) sample and lowest 1.01×10^{18} for the tri layer (YIG/Cu/Pt) sample, calculated value of spin mixing conductance is close to earlier reported value for FM/NM based bilayer or tri layer [82, 304]. Magnetization dynamics in thin films is also affected by the spin pumping and spin back flow, which is the source

of viscous damping. In addition, spin phonon interaction can lead to spin damping or relaxation, in some cases they could also enable spin current to propagate even in the absence of spin-polarized current. Efficiency of this mechanism depends on the spin orbit coupling, crystal structure and phonon modes [15, 54, 292]. Hence, spin mixing conductance of bilayer is higher where as it is lower for tri layer and tetra layer. Minor change in the interface structure can affect the spin pumping efficiency leads to change in the value of spin mixing conductance, we featured to the decrease in the value of spin mixing conductance ($g^{\uparrow\downarrow}$) by slight variation in the interface of the multilayer thin films.

6.4 Conclusions

In summary, we have deposited the heterostructures of ferromagnetic material and normal metal. Series of five samples deposited using PLD and sputtering technique. Deposited, 90 nm of YIG thin film on GGG substrates, Pt of 5 nm over YIG, in between the YIG and Pt, Cu of 2.5 nm as spacer, tetra layer of YIG/Cu/Pt/W and YIG/Cu/W/Pt, in tetra layer deposited all the normal non-magnetic metals of 2.5 nm. We systemically studied the influence of interface on the spin pumping of heterostructures. XRD and AFM characteristics disclosed that the deposited thin films have smooth surfaces and phase pure. Significantly higher value of spin mixing conductance observed for YIG/Pt samples in comparison to others tri layer (YIG/Cu/Pt, YIG/Cu/W) and tetra layer (YIG/Cu/Pt/W, YIG/Cu/W/Pt) from the FMR based spin pumping measurements. These values confirms that squashing of spin current in YIG/Cu/Pt and improvement of spin currents in YIG/Cu/W tri layer, it also confirms that suppression of spin current in YIG/Cu/W/Pt significantly higher spin currents in YIG/Cu/Pt/W tetra layer. These results potentially pave the way for significant enhancement in spin pumping efficiency by engineering multilayer films with optimized spin conductance matching at the interfaces, a convincing potential for insulator based spintronic devices.

Chapter 7

Summary, future scope of work and social impact

The research work conducted for this thesis is summarized in this chapter, with particular attention paid to the goals pursued, the techniques employed, and the main conclusions drawn. The main findings of the research are summarized to emphasize the work's scientific contributions and adaptability. Additionally, this chapter summarizes unresolved problems and areas of future advancement in the understanding and application of spintronics and related phenomena, and it suggests potential directions for future research.

7.1 Summary of research work

The main emphasis of the present work was on the growth and characterization of single crystalline ferromagnetic thin films deposited by the pulsed laser deposition (PLD) technique. This technique allowed accurate control of film thickness, crystallinity, and stoichiometry, which are key parameters for the tuning of structural, magnetic, and interfacial properties of the films. Understanding the magnetization dynamics and spin-dependent transport phenomena crucial for spintronic device applications was made possible by these regulated growth and systematic characterization. Theoretical illustration has been explored for both reciprocal and non-reciprocal electromagnetic wave propagation in the microwave frequency range utilizing various transmission lines and high-frequency structure simulator (HFSS) simulations with nanometer thick ferromagnetic film as the active element. For different spintronics application, the investigation of ferromagnetic/normal metal/ferromagnetic layer and ferromagnetic/normal metal/antiferromagnetic heterostructures has been examined. The potentiality of spin as a carrier across the interface has been established by integrating

noble metal/normal metal with ferromagnetic material to build a multilayer thin film utilizing sputtering and pulse laser deposition techniques. X-ray diffraction (XRD), Raman spectroscopy, scanning electron microscopy (SEM) with EDX, electron beam lithography and atomic force microscopy were used to perform the initial characterizations of the film. Vibrating sample magnetometer (VSM) mode of physical properties measurement (PPMS) system have been used for the static magnetic properties measurement. A popular spectroscopic technique ferromagnetic resonance (FMR) has been used for examining the dynamic magnetic properties of nanometre thick films. FMR has become an essential tool for both fundamental magnetism research and applications in spintronic device research because of its great sensitivity and adaptability. It is explored to determine crucial parameters such as spin mixing conductance, magnetic anisotropy, effective magnetization, and Gilbert damping constant. The fundamental mechanisms of spin transport and magnetization dynamics have been studied by using ferromagnetic resonance (FMR) to study interfacial phenomena, spin pumping, and spin–orbit interactions in thin films and multilayer heterostructures.

7.2 Salient outcome of this thesis

Chapter 1 provides a summary of the work included in this dissertation. This chapter covered the function and significance of ferromagnetic thin films in spintronics devices. The ferromagnetic system and heterostructures based on ferromagnetic and normal metals were discussed in this chapter. The basic physics underlying damping mechanisms and ferromagnetic resonance are also covered. The thesis's motivation has been explained by examining the gap in thin film deposition and its uses in high frequency and spintronics devices.

Chapter 2 comprises an extensive description of the experiments and characterization techniques used in this dissertation. Several thin-film deposition techniques have been discussed. Complementary characterization techniques have been explained, which have

been used to examine the structure, morphology, and magnetic properties of magnetic nanostructures. Additionally, this chapter contains a ferromagnetic resonance (FMR) experiment that was conducted using the proper device geometry and improved measurement techniques in order to ensure an accurate assessment of the magnetic dynamics.

Chapter 3 discuss in specific, the making of YIG bulk targets that was prepared from the synthesized nano/micro particles using the solid-state reaction process. It was determined that the lattice constant of bulk YIG was 12.377 Å. YIG thin film have been deposited using the pulsed laser deposition (PLD) system by optimizing the deposition parameters. By varying the oxygen gas pressure, we investigated the structural, magnetic, and microwave characteristics of epitaxial YIG thin films deposited by pulsed laser on GGG (111) substrates. It has been found that as the oxygen pressure rises from 0.0025 mbar to 0.15 mbar, the lattice constant rises from 12.379 Å to 12.458 Å. Using atomic force microscopy (AFM), the root mean square (rms) roughness of each sample was determined to be less than 0.6 nm. YIG thin-film Raman spectra show peaks at approximately 168, 180, 235, 269, 381, 415, 485, 580, and 600 cm-1, respectively. For both in-plane and out-of-plane geometries, the angular dependent FMR spectra of epitaxial YIG (111) thin films show that 0.15 mbar O2 pressure meets the requirements for the ideal single crystal growth of YIG. For the highest oxygen pressure 0.15 mbar grown film, the lowest Gilbert damping constant was 4.37×10^{-5}, while for the 0.0025 mbar oxygen pressure grown sample, it was 3.55×10^{-4}. For samples with high oxygen pressure, the in-plane cubic magneto-crystalline anisotropy is found to be greater than the uniaxial anisotropy. Additionally, it has been noted that high oxygen gas pressure grown YIG films can achieve low damping constants, which makes them appropriate for spintronics applications, such as narrow band filters.

Chapter 4 described through the use of finite element method HFSS simulations and various transmission lines with 90 nm thick YIG film as the active element, successfully

proved both theoretically and experimentally the reciprocal and non-reciprocal electromagnetic wave propagation in the microwave frequency range. The stop-band filter and isolator response of electromagnetic wave propagations were measured using two distinct microstrip lines. Simulations of high frequency electromagnetic fields were carried out using ANSYS HFSS software. A particular accurate finite element method (FEM) that applies a frequency domain electromagnetic full-wave analysis of the structure being studied is the main technique. Using the identical substrate characteristics as the experiment, theoretically calculated both reciprocal and non-reciprocal electromagnetic waves. There are 1865 grid cells for YIG film, 4400 grid cells for microstrip line, and 47676 grid cells for dielectric substrate. The absorption of EM wave propagation was observed by flipping the YIG thin films on the signal line. In order to study and optimize the effect of conducting or non-conducting resonant magnetic layers, the software uses anisotropic and frequency-dispersive permittivity and permeability tensors. Additionally, it is shown that YIG films grown at varying oxygen growth pressures exhibit distinct properties, and that the optimal device parameters are attained at the maximum oxygen growth pressure. At a dc bias field of 6 KOe, the highest isolation of roughly 6.54% was obtained with a YIG film at 0.15 mbar oxygen gas pressure. Furthermore, it has been shown that the non-reciprocity behavior rises dramatically as the externally applied magnetic field increases. Therefore, the current study clearly shows that a YIG film with a thickness of less than 100 nm may be employed for both reciprocal and non-reciprocal microwave devices, which is a step toward minimizing the size of microwave signal processing devices.

Chapter 5 discussed the technological perspective of ferromagnet/heavy metal/ferromagnet ($FM_1/HM/FM_2$) and ferromagnet/heavy metal/anti-ferromagnet (FM/HM/AFM) trilayer films in spintronic applications in order to gain a more quantitative understanding of the spin injection's contribution. Explained about the deposition of FM/NM/FM (YIG/Ta/Ni) and controlled oxidation of top Ni layer to NiO,

formation of different heterostructures as FM/NM/AFM (YIG/Ta/NiO). Studied the Effect of spin pumping on the controlled oxidation of YIG/Ta/Ni layer. The ferromagnetic resonance linewidth is further broadened as a result of the spin-pumping effect. It was found that the effective Gilbert damping (α_{eff}) of YIG increased from 1.4×10^{-3} to 1.55×10^{-3} of the trilayer structures when (FM2) Ni is oxidized to the (AFM) NiO layer. For YIG/Ta/Ni and YIG/Ta/NiO trilayers, spin-pumping mediated Gilbert damping (α_{sp}) was therefore determined to be 0.5×10^{-4} and 2.0×10^{-4}, respectively (i.e., ~300% increment). The calculated spin mixing conductances were found to be 2.31×10^{17} and 1.39×10^{17} m^{-2} for YIG/Ta/Ni and YIG/Ta/NiO, respectively. By investigating both thermal and phonon-mediated coupling mechanisms, the suggested heterostructure produced coherent long-range magnetization control between ferromagnetic and anti-ferromagnetic layers that are separated by a regular metal spacer. At the YIG/Ta/Ni and YIG/Ta/NiO interfaces, the notable increase in linewidth suggests outstanding spin conversion efficiency. Spin fluctuations and the spin back-scattering mechanism help to enhance the strong spin transport in NiO that results from the oxidation-induced transition from the Ni to the antiferromagnetic NiO layer.

Chapter 6 discusses the growth and characterization of multilayer of YIG, Pt, Cu and W on GGG (111) substrate. Essentially, we have grown Bi-layer, tri-layer and tetra layer of FM/NM, FM/NM/NM, FM/NM/NM/NM heterostructures, where FM is YIG deposited on GGG (111) substrate whereas, NM is Pt, Cu and W. Discussed about the multilayer structure of YIG/Pt, YIG/Cu/Pt, YIG/Cu/W, YIG/Cu/W/Pt and YIG/Cu/Pt/W. The successful growth of heterostructures on YIG is confirmed by the XRD scan and Raman measurement. The root mean square (RMS) value of roughness ranged from.26 nm to.46 nm, according to the AFM data. Due to the spin-pumping effect, the ferromagnetic resonance linewidth is further expanded. There was also a change in the Gilbert damping constant, which was lower for pristine samples (9.97×10^{-4}) and greater for YIG/Pt (4.17×10^{-3}). A change in linewidth and damping characteristics suggests a

corresponding variation at the multilayer film interface. Spin mixing conductance value is higher 2.25×10^{18} in case of bilayer (YIG/Pt) sample and lowest 1.01×10^{18} for the tri layer (YIG/Cu/Pt) sample. Spin pumping and spin back flow, the cause of viscous damping, also have an impact on magnetization dynamics in thin films. According to the FMR-based spin pumping measurements, the YIG/Pt samples had a noticeably larger value of spin mixing conductance than the other tri layer (YIG/Cu/Pt, YIG/Cu/W) and tetra layer (YIG/Cu/Pt/W, YIG/Cu/W/Pt) samples. According to these values, the YIG/Cu/Pt spin current was squashed, the YIG/Cu/W trilayer spin currents were improved, and the YIG/Cu/W/Pt tetralayer spin currents were much larger when the YIG/Cu/W/Pt spin current was suppressed.

In conclusion, we have grown high quality single crystalline yttrium iron garnet (YIG) thin film using pulse laser deposition system by optimizing the different deposition parameters. Oxygen growth pressure was shown to affect a number of variables, including structural, magnetic and FMR dynamics. According to its magnetization dynamics and other characteristics, the highest oxygen grown pressure of 0.15 mbar was determined to be more suitable for the development of YIG thin film and its application in spintronics devices. We have deposited the multilayer thin film by using the pulse laser deposition (PLD) and sputtering techniques. We have used the DC and RF sputtering system for the deposition of metallic thin film over the YIG to grow the multilayer heterostructures. We have performed the spin pumping study on the controlled oxidation Ni to NiO in YIG/Ta/Ni heterostructures and found that spin fluctuations and the spin backscattering process contribute to the robust spin transport in NiO. In order to investigate the dynamics of magnetization and the effectiveness of spin pumping in ferromagnetic/noble metal heterostructures, we have used the DC and RF sputtering approach to deposit the bilayer tri-layer and tetra layer of noble/normal metal over the YIG. We have performed the investigation of spin pumping efficiency on metal deposited YIG/ (Pt, Cu/Pt, Cu/W, Cu/W/Pt and Cu/Pt/W) thin films. By going the magnetization dynamics and spin

pumping measurements on this multilayer heterostructures, these results lead us to the conclusion that YIG/Pt has higher spin pumping efficiency, which is beneficial for its application in upcoming spintronic technologies.

7.3 Future prospective and social impact

It is now possible to optimize PLD and sputtering deposited, YIG and YIG-based multilayer heterostructures respectively and conduct advanced research.

The list of potential future initiatives in this specific area of study is as follows:

Interface Engineering: Quantitative relationships between spin transparency and interfacial defects may be established by further research comparing smooth and rough atomic interfaces.

Temperature-Dependent Investigations: Inferences regarding phonon-assisted spin scattering processes will be possible through low-temperature studies of spin pumping and high-temperature studies of spin damping behavior.

AFM Interlayers: Research on antiferromagnetic interlayers, like NiO, may provide some understanding of long-range spin transport across AFM insulators and magnon-mediated spin transmission.

YIG/Pt, YIG/Cu/Pt, YIG/Cu/W, YIG/Cu/W/Pt and YIG/Cu/Pt/W and multilayers should be studied in detail for the ISHE, Magneto optical Kerr effect (MOKE) and spin Seebeck effect.

Device Realization: These multilayers will help close the gap between basic research and practical applications by being included into prototype spintronic devices such spin-torque oscillators, STT-MRAM, and spin caloritronic sensors.

HFSS and Micromagnetic Simulations: Predictive design of multilayer heterostructures with customized spintronic responses will be possible by combining full-wave and micromagnetic models with experimental investigations.

The research and development of spintronics devices has significant positive social effects, mainly through the development of faster, more powerful, and energy-efficient computing and data storage systems. This development supports breakthroughs in a wide range of industries, including personal electronics, industrial automation, and medical treatment. Because of its exceptional sensitivity, spintronic sensors are being investigated for use in biomedical applications like cancer detection, molecular research, the development of diagnostic chips, and the control of biomedical prosthesis. Faster read/write speeds, greater density, and data retention without constant power are provided by technologies such as Magneto-resistive Random Access Memory (MRAM).